Millimetre Wave Imaging for Concealed Target Detection

by

Lianhong Zhang

A thesis submitted to the University of London for the degree of Doctor of Philosophy

School of Electronic Engineering and Computer Science
Queen Mary
United Kingdom

February 2011

TO MY FAMILY

Abstract

Concealed weapon detection (CWD) has been a hot topic as the concern about public safety increases. A variety of approaches for the detection of concealed objects on the human body based on earth magnetic field distortion, inductive magnetic field, acoustic and ultrasonic, electromagnetic resonance, MMW (millimetre wave), THz, Infrared, x-ray technologies have been suggested and developed. Among all of them, MMW holographic imaging is considered as a promising approach due to the relatively high penetration and high resolution that it can offer. Typical concealed target detection methods are classified into 2 categories, the first one is a resonance based target identification technique, and the second one is an imaging based system. For the former, the complex natural resonance (CNR) frequencies associated with a certain target are extracted and used for identification, but this technique has an issue of high false alarm rate. The microwave/millimetre wave imaging systems can be categorized into two types: passive systems and active systems. For the active microwave/millimetre wave imaging systems, the microwave holographic imaging approach was adopted in this thesis. Such a system can operate at either a single frequency or multiple frequencies (wide band). An active, coherent, single frequency operation millimetre wave imaging system based on the theory of microwave holography was developed. Based on literature surveys and first hand experimental results, this thesis aims to provide system level parameter determination to aid the development of a target detection imager. The goal is approached step by step in 7 chapters, with topics and issues addressed ranging from reviewing the past work, finding out the best candidate technology, i.e. the MMW holographic imaging combined with the resonance based target recognition technique, the construction of the 94 GHz MMW holographic prototype imager, experimental trade-off investigation of system parameters, imager performance evaluation, low profile components and image enhancement techniques, feasibility investigation of resonance based technique, to system implementation based on the parameters and results achieved. The task set forth in the beginning is completed by coming up with an entire system design in the end.

Acknowledgments

I would like to thank Professor Clive G. Parini and Professor Yang Hao for funding me to do the research so that I can perform the investigations in the Antenna Measurement Lab of School of Electronic Engineering and Computer Science, Queen Mary University of London. They guided me through all the stages, giving valuable instructions and sending me to various conferences and seminars so that I had plenty of opportunities to interact with peer researchers of other institutions.

I would like to thank John Dupuy, the Antenna Measurement Lab of School of Electronic Engineering and Computer Science, Queen Mary University of London for the fruitful discussions and his continuous support through the progress of the project, especially for the setting up of the 94 GHz holographic imaging system, without which many of the investigations in this thesis could not have been performed.

I would like to thank Dr. Yoonjae Lee of the same group for allowing me using his woodpile EBG and waveguide structure in the measurements, it was a wonderful collaboration.

I would like to thank my fellow researcher Atiqur Rahman for many discussions over the years and Masood UR Rehman for the help in setting up the Latex system and many tips of using it.

Table of Contents

4 The Performance Evaluation of the 94GHz MMW Holographic Prototype Imager 90

List of Figures

List of Tables

List of Abbreviations

BWO	Backward Wave Oscillator
CT	computed tomography
CONTEST	Counter Terrorism Strategy
CW	Continuous Wave
CWD	Concealed Weapon Detection
EBG	Electromagnetic Band Gap
EM	Electromagnetic
EU	European Union
FDTD	Finite Difference Time Domain
FMCW	Frequency Modulated Continuous Wave
GA	Genetic Algorithm
HEB	Hot Electron Bolometre
HPBW	Half Power Beam Width
IFFT	Inverse Fast Fourier Transform
INL	Idoho National Laboratory
ISAR	Inverse Synthetic Aperture Radar

LMS	Least Mean Square
LO	Local Oscillator
MDF	Medium Density Fibre
MMIA	Millimetre Wave Integrated Array
MMIC	Monolithic Microwave Integrated Circuits
MMW	Millimetre Wave
MoM	Methods of Moments
NEΔR	Noise Equivalent Reflectivity difference
PNNL	Pacific Northwest National Laboratory
PoF	Pencil of Functions
PSF	Point Spread Function
QCL	Quantum Cascade Laser
RF	Radio Frequency
SAR	Synthetic Aperture Radar
SBD	Schottky Barrier Diode
SEM	Singularity Expansion Method
SIS	Superconductor Insulator Superconductor
SNR_I	Signal Noise Ratio of image
S/C	Signal to Clutter ratio
S/N	Signal to Noise ratio
TDS	Time Domain Spectrum
THz	Terahertz
VNA	Vector Network Analyzer
WAMD	Wide Area Metal Detection

Chapter 1

Introduction

1.1 Background

Concealed weapon detection (CWD) has been a hot topic as the concern about public safety increases. There have been a series of attacks dating back to December 1988, the terrorist bomb that brought down Pan Am Flight 103 over Lockerbie, Scotland, followed by the September 11, 2001 attack, then the stories of the London bombings of 7 July 2005, causing enormous loss of property and human lives. The public transportation system and gathering places attracted most of the interests from the terrorists because of its economic significance and the influence that the terrorists can exert through it.

In response to the growing threat from domestic and international terrorism, the UK government adopted a counter-terrorism strategy(CONTEST) [1], focusing on the most significant security threat to the people of the UK today and the threat from international terrorism. In the US, the Transportation Security Administration (TSA) provided its National Research Council (NRC) with following statement of task: 1. identify potential applications for technology in transportation security with a focus on likely threats; (2) evaluate technology approaches to threat detection, effect mitigation, and consequence management; and (3) assess the need for research, development and deployment to enable implementation of new security technologies [2].

The introduction of computed tomography based on x-ray to the airport check-in procedure for the passenger luggage has improved the security, however, for the passengers, security check still relies on the hand held and portal-style metal detectors assisted by human stop and search. As described later on in section 2, there are drawbacks for this type of detectors, and the weaknesses can be exploited by the sophisticated terrorists. The public and authority call for complex and comprehensive security systems.

A variety of approaches to concealed objects detection on the human body based on magnetic, acoustic/ultrasound, microwave/MMW, THz, infrared, and x-ray technologies have been suggested and developed. Various concealed target detection approaches have been developed. Two overviews were performed by Costianes in [3] in 2005 and Agurto in [4] in 2007. As a subject of aggressive academic and industrial research, considerable progresses was reported over the last 2-3 years. A comprehensive review will be given to reflect these in the following sections. The review will focus on the technologies of CWD systems used and the surrounding issues that need to be addressed. Based on the review, a research proposal was raised and this is discussed in Section 1.4. The last section of this chapter is the outline of the thesis in which the issues and goals set forth in section 1.4 are listed and to be addressed and approached in proceeding chapters.

1.2 Review of current CWD research

Here we will briefly consider the range of methods found in the open literature.

1.2.1 Metal detection and earth magnetic field distortion

1.2.1.1 The description of the technology

The operating principle is based on the detection of the distortion of the earth's magnetic field caused by the metal objects carried by an individual passing through a portal-style CWD system. The detectors that are used in this type of CWD systems are called Gradiometer Metal Detectors which was described in [5]. A gradiometer consists of two magnetometers which are connected electronically in a differential mode, in such a way the false alarms caused by the background fluctuations can be reduced. A gradiometer responds to the change of the earth magnetic field caused by a moving ferromagnetic object. It is a new application of the existing magnetometers.

Such an idea has been implemented by the Idaho National Laboratory (INL), see Fig 1.1. An array of 16 gradiometers are on both sides of the portal-style CWD system. Data are collected from each gradiometer and the change of earth magnetic field is determined. After data processing the location and size of the metal object is located. A freeze-frame video capture technology provides a graphical interface in which the location of suspected threatening object can be indicated.

Figure 1.1: Concealed weapon detection using a magnetometer-based portal (*http : //www.inl.gov/library/*)

Certain classes of weapons and items such as keys, coins, mobile phones have their unique spectral signatures and they can be used for target automated identification and classification. INL has developed an algorithm to perform pattern recognition by analysing the collected spectrum signatures and comparing to a known database of weapons vs non-weapon responses.

1.2.1.2 Considerations for use

As a passive non-contact CWD system, it has no medical device interference. The spatial resolution of the system is dependent on the number of gradiometers used on either side of the portal. Increasing the number of gradiometers means increasing the cost. The system requires the objects to be ferromagnetic to be detected, which is a drawback. Metals such as copper, brass, lead, aluminum and some stainless steels are non-ferromagnetic hence undetectable.

1.2.2 Inductive Magnetic Field Methods

1.2.2.1 The description of the technology

The theory of operation can be explained using Fig 1.2 [6]. There are two coils in the CWD system, one is transmitter coil, the other is receiver coil. A pulsed or alternating current flows in the transmitter coil producing time varying magnetic field around the coil itself, which is detected by the receiver coil. If a metallic object is put between these two coils, according to Faraday's law, time varying magnetic field will induce an electromotive force in the metal object, and this force will causes eddy currents to flow in the metal which generates the secondary magnetic field. Eddy currents decrease with a characteristic decay time depending on the shape and size of the metallic object. Because of its uniqueness, it can be considered as the signature of the object. The secondary magnetic field is detected by the receiver coil and interferes with the one produced by the source coil, finally a current containing the target signature information is produced in the receiver coil. If the database containing all the threatening weapons' signatures is developed, when a concealed metal object is detected, a potential threat can be identified by comparing to the database.

Wide-Area-Metal Detection (WAMD) is a recent application of inductive magnetic field approach [7], such a detection system employs spatially distributed metal detectors combined with a video surveillance system and it can be used to screen large crowds of people more efficiently, reducing the need for each person to be examined separately.

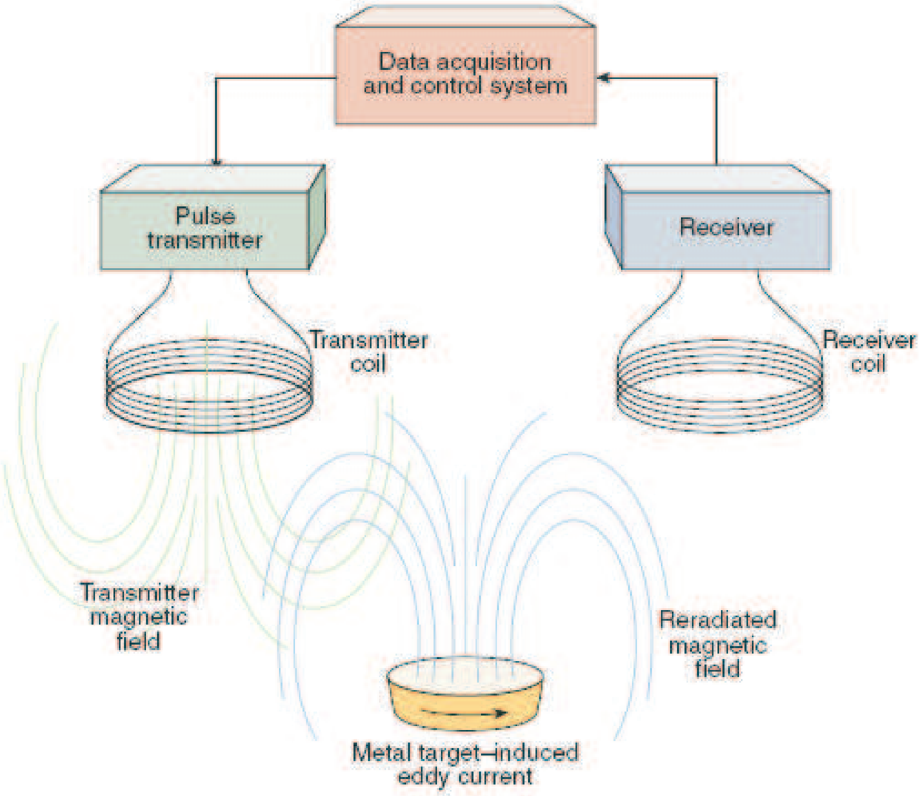

Figure 1.2: Basic pulse induction metal detection scheme [6]

1.2.2.2 Considerations for use

Inductive magnetic field methods suffer from the problem of sensitivity. For objects with low conductivities (generally for non-metallic materials) or small size metallic objects, they can hardly be detected because the human body signal maybe larger than the detection signals from the objects. Also, this technology primarily detect only metal objects. Unless multiple detectors are used, the device will not provide location information of the object.

1.2.3 Acoustic and Ultrasonic Detection

1.2.3.1 The description of the technology

The operation principle is dependent on the acoustic reflectivity of the object. It is worth noting that acoustic waves are mechanical vibrations, the reflectivity is related to the shape, orientation and hardness of the object [5]. Basically, hard objects produce high acoustic reflectivity, plastic objects could provide the same strength of reflectivity as metals, which differs from EM wave based technologies. However, there is a problem of the penetration ability of clothes for ultrasonic detection when it is used for CWD operation, for example, leather could cause large acoustic reflections which makes the concealed weapons undetectable. Also, there is no differentiation in the reflections from weapons and hard non-weapon objects.

A nonlinear acoustic CWD detection by combining ultrasonic and acoustic methods has been suggested [8], Fig 1.3 illustrates the concept. Two sets of transducers produce two ultrasonic beams with frequencies of f1 and f2. Focusing devices are used in the transducers so the ultrasonic beams can propagate over the long distance and still focus at the target. The two beams are mixed at the focused zone which produces 4 frequencies, i.e. f1, f2, f1+f2, f1-f2, here only the difference frequency f1-f2 is chosen and it is tuned to the audio range so that it can penetrate to the clothing and interact with the subject. The return from the target is used for analysis such as pattern matching and classification.

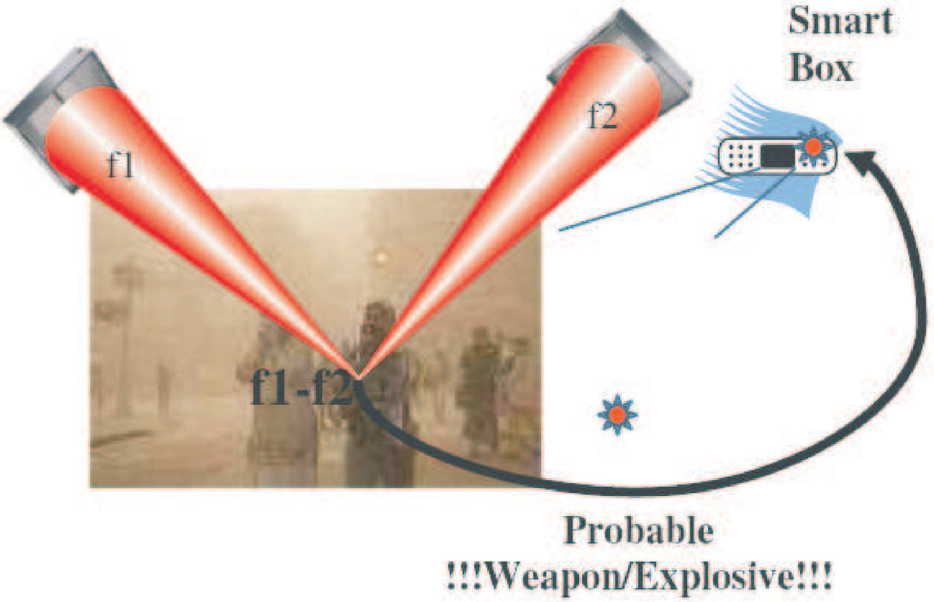

Figure 1.3: Concept showing crossed beam ultrasonic nonlinear acoustic generator for CWD [8]

1.2.3.2 Considerations for use

This technology is sensitive to hard objects, and cannot differentiate between weapons and non-weapons. Since leather causes high acoustic returns, targets concealed by it may not be detected. The use of the harmless acoustic and ultrasonic waves for the detection is an advantage compared to technologies based on other parts of the spectrum. However, fast scanning of ultrasonic beams whilst still focusing on the target is a concern for practical use.

1.2.4 Electromagnetic Resonances Based Target Recognition

1.2.4.1 The description of the technology

The method, which is called singularity expansion method (SEM), was first reported by C. E. Baum in 1971 [9], it is based on the analytic properties of the electromagnetic response as a function of two-sided Laplace transform variables which can be called the complex frequency. The singularity expansion method (SEM) is stimulated by observing the transient electromagnetic response which appears to be dominated by a few damped sinusoids. If the Laplace transform is performed, a damped sinusoid corresponds to one pole in the complex frequency domain [10]. These poles or complex frequencies are associated with the target shape, size and material and independent of the interrogation signal, hence they are called natural resonance frequencies which can be used to characterize the target. In addition, resonance based scattering exhibits some features which are attractive for CWD. They are: 1. The scattered return is larger in the resonance region. 2. The natural resonance seen in a scattered return are independent of the orientation of the object. 3. An object's resonance patterns uniquely identify it within a class of objects. 4. A few natural resonances characterize an object over a large frequency band [11].

A pulse of microwave/radio frequecy or a swept frequency source is used to illuminate the target space, the return of the illumination signal from the target is used to extract the signature of the target. A few resonance frequency extraction methods such as Prony's method [12], the pencil-of-function method (PoF) [13], E-pulse method [14] and Genetic Algorithms [15] have been developed.

The extracted target signature (characterized by the extracted complex natural resonance frequencies) is compared to the database that stored signatures of the all the known weapons to determine whether there is a match. If yes, an alarm is automatically activated.

1.2.4.2 Considerations for use

Resonance based target recognition has the advantage of simple system implementation but high false alarm rates caused by the presence of the human body. A Recent report by the group in Manchester Metropolitan University [16] shows that the transient responses from a human body with and without a concealed handgun are evidently different, and the later time response from the tested handgun is obvious. The extracted complex resonance frequencies of the handgun on and off the body are close to each other only with change of the damping factor of one of the complex resonance frequency. CWD systems based on different technologies can be combined and complement each other, in this thesis, the electromagnetic resonances based detection system will be combined with the MMW imaging based system which will be discussed later on.

1.2.5 Millimetrewave based technology

1.2.5.1 The description and development of the technology

Microwave/MMW imagers can be categorized into 4 types: 1. Microwave/MMW Radar Imager. The operation principle is based on the detection of the Doppler-frequency shift in the reflected signal from the moving target. To obtain the distance or range information, the continuous-wave must be modulated, a common waveform is Frequency-modulated Continuous-wave (FMCW). This is the conventional Radar technique, only the coordinates of the object is determined. 2. Broadband/Noise Pulse MMW imager. A very short duration pulse or a noise pulse is used to illuminate the target, the reflected energy is recorded and the image is formed by the spectrum intensity at each spatial location. 3. Microwave Holography imager. Holographic imaging is based on the interference of two beams of electromagnetic waves. The return waves from the target interferes with the reference beam and amplitudes and phases across the recording aperture are recorded. A holographic processing algorithm is used to reconstruct the target image. 4. Passive MMW imager. The operation of this type of imager is similar to Braodband/Noise Pulse MMW imager but rely on natural illumination.

Imaging systems operating at 27-33 GHz (microwave holographic imager) [21], 94 GHz (passive imager) [22], have been reported. Recently a sensor working at 220 GHz based on state-of-the-art solid-state components has been demonstrated for passive MMW imaging [23] and showed acceptable image quality for standoff detection of metallic and non-metallic objects. It is believed that for operating frequency above 500 GHz, only active systems are effective for stand-off concealed target detection due to the atmospheric and material attenuation [18]. System with operating frequency below 35 GHz are mature because of the availability of components.

Atmosphere phenomenology investigation is vital for stand-off detection and must be understood for the effective implementation of microwave, millimeter wave and terahertz imaging systems. Atmospheric effects, including rain, fog, air pressure and temperature effects, across the entire electromagnetic spectrum has long been studied since the 1950s [17] and were reviewed in [18]. Atmospheric phenomenology investigation from microwave up to infrared, has been performed, with more and more accurate results have been accumulating in the literature or updated. But for the THz band, due to the non-availability of THz components, there is a lack of atmospheric phenomenology data available. Through this investigation, atmospheric absorption windows around 35 GHz, 94 GHz, 140 GHz, 220 GHz, and 650 GHz were found.

Equally important is the material phenomenology investigation. The mechanism of active imaging is based on the reflectivity contrast from different materials in the target space. Passive imaging mechanism is more complex, for frequency less than 100 GHz, it is produced by the contrast in emissivity and reflectivity from the different target materials, for frequencies at 500 GHz and above, it is dominated by the emissivity of the items and their physical temperature [18]. Reflectivity is related to target material property which is frequency dependent, [19] is an extensive investigation of human tissue property below 100 GHz, however measurement at high frequency (above 100 GHz) has not been largely reported. One more factor that increases the complexity is the interaction between items to be imaged. When the frequency goes high, the wavelength becomes comparable to target dimension such as clothing weave period, which may cause resonance, so the material is no longer treatable as homogeneous.

The key issue for Microwave/MMW based imaging is the mapping of field distributions. The system implementation is somewhere between optical and Radar technologies. Its data processing schemes mainly inspired by those established in other technologies such as incoherent projection imaging, coherent holography and near-field scanning microscopy in optics, Sonar, echotomography in ultrasound, computed tomography in x-rays [20].

1.2.5.2 Considerations for use

Resolutions of MMW imagers are generally high enough for weapons detection. Both metallic and non-metallic targets can be detected. Penetration to clothing is good. Standoff detection can be achieved. The MMW imager can be a portal-style systems. Handheld MMW imager is also possible [24]. MMW imagers pose no ionizing hazard to the individuals. Using high operating frequencies they can achieve high spatial resolution but material and atmospheric attenuation also increases, so there is a trade-off here. For a given application, an optimal frequency exists. Constructing imaging systems operating at high frequency is expensive. Researchers rely on modelling to investigate the scattering and diffraction characteristics, but the most realistic investigation is by experiment. At low frequencies, atmosphere and material phenomenology is well understood, however, system operation at frequencies above 100 GHz is still mainly in the component level, with reports above 100 GHz being mainly on the improvement of device performance.

1.2.6 THz based technology

1.2.6.1 The description and development of the technology

The principle of operation for a THz CWD system is based on the fact that explosives and other prohibited dangerous chemicals have unique absorption spectra in THz frequency range which can be used to for material classification. See Fig 1.4, it is obvious that glutarnic acid has a distinctive absorption spectra compared

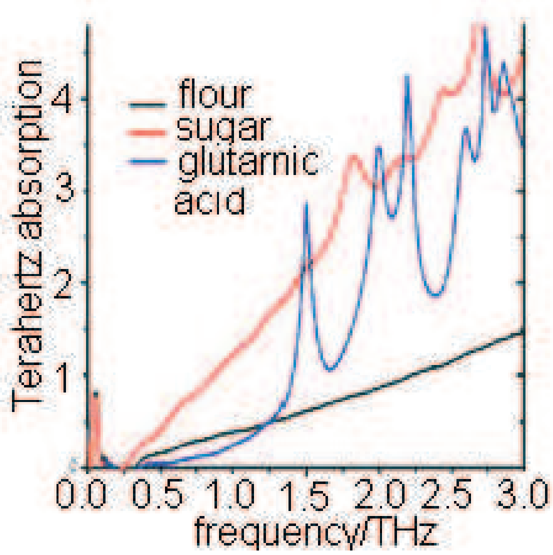

Figure 1.4: Three terahertz spectra showing glutarnic acid, a basic building block of proteins in living matter, compared with two other common powdered substances *http* : //*www.teraview.com*/*terahertz*/*id*/12

to flour and sugar. Depending on the scenarios, either transmission or reflection mode can be used. An interrogation THz pulse is launched and the transmission or reflection from the target is received. By applying Fourier transform to the received time domain signal, the absorption spectra of the target can be revealed. This type of detection is called Time Domain Spectroscopy (TDS).

Another application of THz is the imaging based detection. Its operating principle is similar to a pulsed MMW imager. Since metals, ceramic guns and knives, clothes and human skin gives different level of reflection in the THz band, THz pulsed imager can be used for security screening.

Teraview [25] is the first commercialized terahertz imaging system using a short pulse as the waveform, but its application is limited to very short range 3D imaging, for example, the imaging of tablet coating and cores, not for stand-off detection.

Within the electromagnetic spectrum, there is a THz gap from submillimeter wave band to far infrared that has remained largely untouched for some time due to the non availability of components such as RF sources, LO, mixer, etc. Two methods can be used to generate THz based on electronics and photonics. For the photonic method, the femto-second laser TDS systems are very popular [26], moreover, THz can be generated by mixing of two laser frequencies in a photo conducting antenna. Systems of this kind are compact and less expensive than femto-second laser systems [27]. The electronic approach is to use electronic component such as Schottky-barrier diode(SBD), superconductor-insulator-superconductor(SIS) and hot electron bolometre (HEB) mixers as the heterodyne detectors [28].

For the creation of the THz LO source, there are optics and electronics approaches as well. For the optical approach, a single frequency far-infrared laser can be used, and for the electronic approaches, there are three techniques, namely, harmonic multiplier, backward-wave oscillator (BWO) [28], and Quantum Cascade Laser (QCL) [29]. For frequency below 340GHz, electronic approach MMIC technology can be used.

1.2.6.2 Considerations for use

THz based CWD has the advantages of high resolution, wide THz spectra, and uses non-ionizing radiation to illuminate human body. However one disadvantage of using the electronic approach to generate THz signals is the limited output power which is not suitable for stand-off detection. In addition, THz atmospheric absorption is high compared to lower frequency bands. Therefore it will be necessary to study high output power components and sensors with more sensitive receivers.

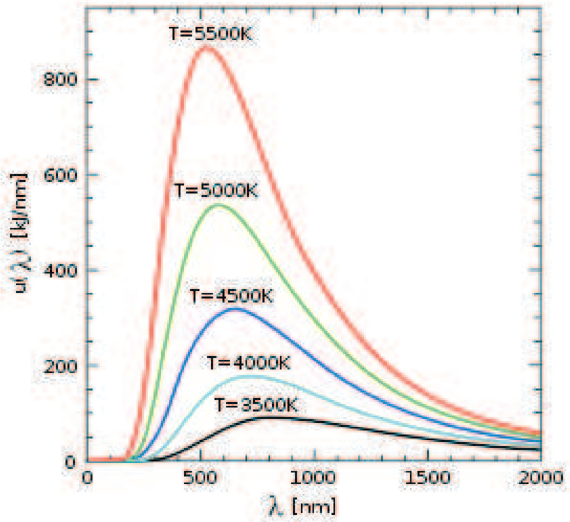

Figure 1.5: Black body spectrum (spectral energy density inside a blackbody cavity). $http://en.wikipedia.org$

1.2.7 Infrared Imager

1.2.7.1 The description of the technology

The operating principle of an infrared imager is based on the detection of thermal radiation difference from the target space. In physics, the spectral radiance of electromagnetic radiation from a black body can be described by the Planck's law and it is a function of frequency ν and absolute temperature T which is illustrated in Fig 1.5. From the curves in the figure, it can be seen that the spectral radiance peaks vary with the change of absolute temperatures, which implies that the infrared detection of concealed weapons or dangerous contraband materials is essentially a function of the temperature difference between the object and the human body.

1.2.7.2 Considerations for use

Infrared imaging has a few drawbacks when used for CWD operations. Firstly, the wavelengths in infrared band are too short to penetrate clothes. Assuming the clothing is tight, the radiation from the human body heats the clothes and the radiation is re-emitted which would make the target image blurred. For loosely wearing clothes, it would be even more difficult for CWD operation as the human body radiation would be spread over large area. Secondly, when the temperature of the concealed target approaches that of the human body, which is likely to occur when the target is concealed in the body for a long time, detection would be difficult.

1.2.8 X-ray Imager

1.2.8.1 The description of the technology

The first commercially viable CT scanner was invented by Sir Godfrey Hounsfield in Hayes, United Kingdom at EMI Central Research Laboratories using x-rays. Hounsfield conceived his idea in 1967 [30]. Medical screening is one of the major applications for x-ray imaging, but it cannot be used for security check for passengers due to dose. The application of x-ray imaging in security differs from the medical screening in the way that the former relies on the backscattering whereas the latter the absorption for the incident x-rays. The theory of operation for x-rays imager can be explained by the Compton effect [5]. The Compton effect is a quantum mechanical phenomenon. In x-ray backscattering, an x-ray photon interacts with the electron bound to an atom and transfers the kinetic energy to it. When the photon is scattered backwardly, its energy is reduced by the amount transferred to the electron and this phenomenon can be exploited for imaging.

1.2.8.2 Considerations for use

X-ray imaging can provide high spatial resolution and its penetration ability of clothes is high. Both metallic and non-metallic targets can be detected. Scanning speed of Commercially available x-ray imagers is high enough, a few seconds per scan. However, there are a few drawbacks for x-ray imaging: 1. It requires each side of the subject to be scanned, in the cases of a human body, 4 scans are needed. The x-ray imagers used for security screening are low energy operation, penetration to flesh is a few centimeters deep, so targets contained in cavities of the body may not be able to be detected. 2. Since the x-ray imaging for a human body contains anatomical information, it raises the privacy issue. 3. There may be a safety concern because x-ray radiation is ionizing, even though the dosage is much below the level that the authority believes is safe. Public acceptance is thus an issue.

1.2.9 Discussions

Eight common used CWD technologies have been reviewed, i.e. earth magnetic field distortion, inductive magnetic field, acoustic and ultrasonic, EM resonances, MMW, THz, Infrared, x-ray. Fig 1.6 shows the corresponding EM spectrum region in which each of them operates. TABLE 1-A summarizes the technical features in term of energy type, illumination mode, operation proximity and portability. TABLE 1-B is the assessment of these technologies from the detection performance point of view, degree of penetration, detectable weapons and main issues for each of the eight CWD technologies are tabulated.

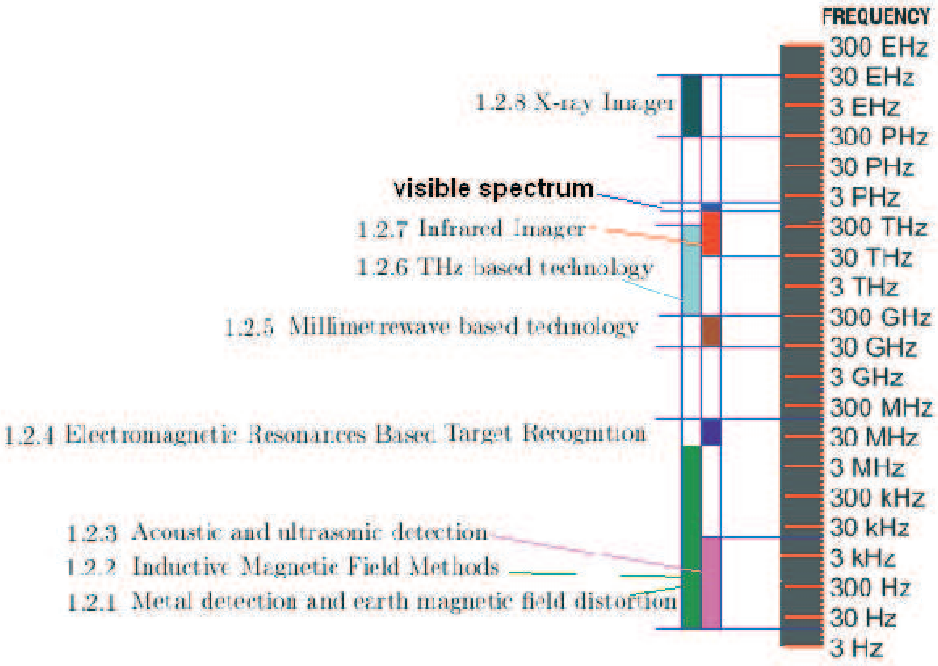

Figure 1.6: Electromagnetic spectrum and corresponding technologies

These eight CWD technologies will be assessed in terms of their performances in the detection, identification and classification processes. Here we use the following definitions with regard to threat interdiction [2]:

1. Detection: the process for discriminating objects of possible interest from their surroundings.
2. Identification: determination of threat, and
3. Classification: determination of the threat's characteristics.

The earth magnetic field distortion method is an identification technique which exploits the distortion of earth magnetic field when the ferromagnetic objects passing through the portal-style CWD system. It is a harmless passive system and poses no interference to the medical devices wore by the individuals. Penetration ability is high. The system is large but transportable. The major drawback lies in the fact that it cannot identify non-ferromagnetic targets. The other magnetic energy based technology is the inductive magnetic field methods. It is an active system with high penetration ability and only metals can be detected and identified (if there is a target magnetic signature database to compare with). There are two main issues for this technology: low sensitivity due to the human body background noise and lack of target location information. The acoustic energy based systems include the acoustic and ultrasonic method. They are active and portable and can be used for stand-off operation. Only hard targets can be detected, identified and classified (metals are generally hard objects, other hard but non-metallic objects include credit cards, ceramic knives etc.). The main issue for the acoustic based technology is its lack of differentiation of weapons from non-weapons and insufficient penetration ability. The EM resonances based technology uses EM energy. It is an active system and can be used for stand-off operation. Such a system is transportable. It has a high penetration ability and both metallic and non-metallic objects can be identified and classified. It has the drawbacks of high false alarm rates and a signature database of weapons is required. MMW based technology has the widest range of technical choices. It can be either active or passive and portability can be either transportable by a vehicle or hand held. It has a high penetration ability for clothes and both metals and non-metals can be detected. Stand-off operation can be achieved. MMW illumination is non-ionizing. MMW technology is imaging based, discriminating objects by their images. Compared to signature based identification and classification, imaging based technology requires a large amount of target information, which makes the system complex and costly. For THz based technology, there exists two classes of systems, one uses the time domain spectroscopy for target material classifications and the other is imaging based target recognition. The system is transportable, both metals and non-metals can be detected. While THz provides high resolution, it has the drawbacks of high

Table 1-A: A tabulation of the different technologies reviewed in this section

CWD Technologies	Energy	Illumination	Proximity	Portability
Earth Magnetic Field Distortion	magnetic	passive	near	transportable
Inductive Magnetic Field Methods	magnetic	active	near	transportable
Acoustic and Ultrasonic	acoustic	active	far	portable
EM Resonances	EM wave	active	far	transportable
MMW	EM wave	active or passive	far	transportable and handheld
THz	EM wave	active	near	transportable
Infrared	EM wave	passive	far	transportable
X-ray	EM wave	active	near	transportable

atmospheric absorption and is limited to operation close to the target. Infrared technology based imagers are passive and transportable and portable. Stand-off operation is possible. Both metals and non-metals can be detected. But it has the drawbacks of low penetration ability to clothing and no differentiation (assuming emissivity is the same) for targets with the same temperature. X-ray imager is an active system. The system is generally large but transportable and it is close-range detection. Both metals and non-metals can be detected. While it has the advantages of high resolution, high penetration ability, the two drawbacks, i.e. privacy violation and safety concerns, hinder its acceptance by the general public.

1.2.10 Conclusions from the review

From this brief review it is evident that MMW based techniques offer an attractive solution because it has good penetration ability and high resolution, both metallic and non-metallic objects can be detected, both stand-off and near proxim-

Table 1-B: A tabulation of main issues of the different CWD technologies

CWD Technologies	Penetration	Detectable Weapons	Main issues
Earth Magnetic Field Distortion	high	ferromagnetic metals	non-ferromagnetic targets undetectable
Inductive Magnetic Field Methods	high	only metals	1. sensitivity not enough 2. lack of location info
Acoustic and Ultrasonic	medium	hard objects	1. lack of differentiation 2. penetration insufficient
EM Resonances	high	metal and non-metal	1. high false alarm rate 2. Signatures Database needed
MMW	high	metals and non metals	high cost
THz	medium	metal and non-metal	1.stand-off detection unsuitable 2. high absorption loss
Infrared	low	metal and non-metal	1. low penetration 2. no differentiation when temperature contrast is low
X-ray	high	metal and non-metal	1. privacy violation 2. safety concerns

ity operation are possible, with no ionising radiation hazard. Even active systems pose little threat to the person being scanned. The radiation power of the active imaging system used for imaging could be 1000 times lower than the EU standard for the maximum allowed radiation power density on an individual, which is $50W/m^2$ [31]. In addition, it has other advantages such as size reduction, wide available bandwidth and mitigation of industrial interference frequencies compared to microwave band. All of these make it an ideal frequency for concealed weapon detection.

The possibility of combining MMW imaging with EM resonance based detection offers the potential for improved system performance. EM resonances based CWD technology is active and can be used for stand-off detection. It has a high penetration ability and both metallic and non-metallic objects can be detected. Its drawbacks of high false alarm rates can be circumvented by the combination with the MMW imaging based technology. Since the MMW imaging system providing the target image, this would greatly narrow down the lists of weapon signatures that automation target recognition algorithm needs to compare to, and this will improve detection rate.

Some of the core issues surrounding such systems are considered in the following section.

1.3 Imaging system concepts, parameters and technical choices

When designing MMW imaging systems, there are a few technical parameters that need to be determined, the system requirements include the selection of system operating frequency or frequencies, imaging system resolution, temperature resolution (for passive systems),video frame rate, the choice of single frequency operation or wide band frequency operation, passive or active imaging. For system architecture, there are choices of coherent or incoherent receiving, pulse or holographic. System operating environment requirements include indoor detection or outdoor detection, close range or stand-off detection, controlled or uncontrolled target scanning scenarios. Signal processing plays an important role in the retrieval of the images, different system designs employ different processing techniques.

1.3.1 Spectrum

Atmosphere phenomenology investigation is vital for stand-off detection and must be understood for the effective implementation of microwave, millimeter wave and terahertz imaging systems. Atmospheric effects, including rain, fog, air pressure and temperature effects, across the entire electromagnetic spectrum has long been studied since the 1950s [17] and were reviewed in [18]. More and more accurate results from microwave up to infrared have been accumulating in the literature or updated. But for the THz band, due to the non-availability of THz components, there is a lack of atmospheric phenomenology data. It is found that not every sub-band of MMW is suitable for imaging, in fact, there are only four atmospheric absorption windows i.e. 35 GHz, 94 GHz, 140 GHz, 220 GHz existing within the range of MMW band (30 GHz-300 GHz) that are available for use. Air absorption is an important factor and has to be taken into account especially for passive imaging system designs for outdoor long range systems.

Equally important is the material phenomenology investigation. The mechanism of active imaging is based on the reflectivity contrast from different target materials. Passive imaging mechanism is more complex, for frequency less than 100 GHz, it is produced by the contrast in emissivity and reflectivity from the different target materials, for frequencies at 500 GHz and above, it is dominated by the emissivity of the items and their physical temperature [18]. Reflectivity is related to the target material property which is frequency dependent, [19] is an extensive investigation of human tissue property below 100 GHz, however measurement at high frequency (above 100 GHz) has not been widely reported. One more factor that increases the complexity is the interaction between items to be imaged. When the frequency goes high, the wavelength becomes comparable to target dimension such as clothing weave period, which may cause resonance, so the material is no longer treatable as homogeneous.

Using high operating frequencies can achieve high spatial resolution but material and atmospheric attenuation also increases, so there is a trade-off here. For a given application, an optimal frequency exists. Constructing imaging systems operating at high frequency is expensive, researchers rely on modelling to investigate the scattering and diffraction characteristics, but the most realistic investigation is by experiment. Imaging systems operating at 27-33 GHz (active) [21], 94 GHz (passive) [22], 250 GHz (passive) [32] have been reported. It is believed for operating frequency above 500 GHz, only active systems are effective for stand-off concealed target detection due to the atmospheric and material attenuation [18]. System with operating frequency below 35 GHz are mature because of the availability of components. At low frequencies, atmosphere and material phenomenology has been well understood, however, system operation at frequencies above 100 GHz is still mainly in the component level, with reports above 100 GHz being mainly on the improvement of device performance. *Teraview* [25] is the first commercialized terahertz imaging system using short pulse as the waveform, but its application is limited to very short range 3D imaging, for example, the imaging of tablet coating and cores, not for stand-off detection.

1.3.2 Single frequency versus multiple frequencies

Generally speaking, multiple frequency operation provides more target information than single frequency. In 3-D imaging, multiple frequency operation can offer a deeper view than single frequency operation for close range large aperture operation [33].

For multiple frequency operation systems (frequency scanning), leaky wave antennas are often used. One important device which is worth mentioning here is the Rotman lens. While a leaky wave antenna can realize beam scan by frequency scan, the Rotman lens allows the beam to maintain the same direction as frequency scans. The feature is useful when there is a need to illuminate the same target at different frequencies. Such an application of the Rotman lens as the antenna of the concealed weapon detection system was discussed in [34].

For broadband/multi-frequency operation radiometry systems, if intermediate frequency (IF) beam forming(fixed time delay) is used, there is a dispersion issue as time delay in each receiving channel is not unique(varies as incidence frequency sweeps). One solution for this issue is to convert up the frequency and form the beam with optical components [35].

1.3.3 Pulsed imaging system

A single pulse offers little target information, very rarely is it used for detection. Multiple pulses offer more information, when received, they are integrated together. For multiple pulses, there are choices of coherent and incoherent receiving. In coherent waveforms each pulse transmitted takes the same phase. Coherent integration is more efficient, less receiving pulses are required to build up sufficient S/N, but the system requires a reference oscillator to synchronize. For the incoherent pulse integration system, it is less efficient, but it is easier to implement [36]. All the system that require phase information such as microwave holography, SAR, need coherent waveform so that the phase relationship from pulse to pulse can be maintained.

1.3.4 Thermal sensitivity

The mechanism of passive imaging is based on Plank's black body radiation theory. Temperature sensitivity is the minimum thermal temperature difference that the system can differentiate and it can be calculated by the following equation [36],

$$\Delta T_{min} = (T_a + T_{sys})[1/\beta\tau + (\Delta G/G)^2]^{1/2} \tag{1.1}$$

where T_a is antenna temperature, T_{sys} is system noise temperature, β is system bandwidth, G is the average power gain of the radiometer's pre-detection stage, ΔG is the variation, τ is integration time of an ideal integrator.

1.3.5 Polarisation technique

There is an advantage of using circular polarization, because the return signal will not be affected by the orientation of the target. An example using Circular Polarisation technique can be found in [34]. However, polarisation discrimination can offer additional target information. In the prototype imager developed in this thesis, a linear polarisation technique was used.

1.3.6 Beam forming techniques and scanning principles

There are two types of beam forming techniques, i.e, optical beam forming and electronic beam forming. For optical beam forming, dielectric lens antenna, reflector antenna, Rotman lens are the typical devices used.

QinetiQ has developed two experimental imagers using optical beam scan techniques. The first one is the single frame imager MITRE [37] using object space scanning technique, which means the main reflector is driven by a motor for beam scan, and the second one is the fast frame rate imager JULIET [37] using conical beam scan, in which the sub-reflector is tilted at an angle and scans by rotating around the axis. The advantage of conical scan in the focal plane space over the object space is that the frame rate can be increased. Another technique to increase the imaging frame rate is to use multiple receiving channels such as the focal plane staring array [35].

As for electronic beam scanning techniques, they can be classified into two types, the first one is a phased array, by adjusting the phase of each element as programmed, the beam steers accordingly, and the second beam steering technique uses frequency dependent beam scan devices, for example, leaky wave antennas.

1.3.7 The concepts of target recognition, 2D imaging and 3D imaging

Target recognition does not provide the real image of a certain target but gives a ”Yes” or ”No ” answer to whether a certain type of threat exists. For systems requiring such a single type of detection information, the design could be simple. In [38] a resonance based target detection approach was demonstrated. An interrogation signal was launched and the reflected signal from the target was received and processed. A spectral signature which can be used to characterize the object was extracted. The processing algorithm is not trying to reconstruct the object image from the return responses, instead, it extracts EM signature that represents the target, then by comparing to the database, the system determines whether there is a threat or not.

A typical 2-D passive imaging system employs a focusing lens and a receiving array near the focal region. The operating principle of such a system is analogous to an optical camera system. The image of the target is projected on the focal plane and a receiving array is placed at that point from where the spectrum energy of the reflection from different parts of the target can be recorded. As reflectivity and natural emission from the target and its background are different (e.g a human body and clothing), the contrast would form a 2-D image. There are a few types of designs based on this principle. An example can be found in [37], in which the Cassegrain antenna system was employed for W band operation. A narrow beam (half power beam width of 0.18 degree) was created by the paraboloid aperture. It took a few minutes to take a still frame of a body. [39] is another example, in which a tilted rotating scanner was used in the optical design. It produces a conical scan over the object field.

Using pulses as the interrogating signal and recording the return across the imaging aperture, in terms of the intensity and the delay time of the reflected signal at different cross sections of target, a 3-D image can be formed. This type of 3-D image is also called range image [40]. 3-D image (height map) can also be formed by interferometric synthetic aperture radar (SAR) technology [41], in which two receiving antennas are used to detect from the scenes/targets illuminated by the same antenna. By applying SAR processing, elevation and height information can be derived from the collected data.

1.3.8 Component issues

Component breakthroughs have always played an important role in the development of microwave, millimeter wave and THz imaging technology. Imaging approaches such as holography, tomography, time reversal etc. were initially used in acoustic, optics and X-ray imaging, they were introduced to microwave band later on as the result of the availability of microwave components. So far, components such as the RF source, LO (Local Oscillator), multiplier, front end transmit/receiving sensor availability below 100 GHz are not a hindrance to the research, but constructing the imaging system is still expensive even though technically it can be done. Research below 100 GHz is focused on the cheaper device development and proof-of-principle experiment.

1.3.9 Architectural issues

As stated previously, for passive imaging systems, the imaging mechanism is based on the contrast of the natural emissivity and the reflection of natural illumination from a certain target against its background. In order to boost the receiving signal to noise ratio, collimating devices such as spherical, parabolic or lens are commonly used. For active imaging systems, the signal to noise ratio requirement is easy to meet, the imaging system can use a pupil plane scan so as to simplify the imaging system architecture. Imaging array has been a hot research topic recently and is the device used to replace mechanical scanning and thus realize real time imaging. There are a few challenges such as device packaging, the spacing and mutual coupling issues between adjacent elements, sensor sensitivity etc, that need to be met. Above the 90 GHz and into the THz band, quasi-optical devices such as reflectors, collimators, wave splitters are used to bend, focus and split the waves.

1.3.10 Data processing for image formation

In fact the processing techniques used in millimeter wave and THz imaging are borrowed from radio astronomy, seismology, and optics. For microwave active imaging, synthetic aperture radar processing techniques are often used. The Canadian RADARSAT-1 is an application example of SAR processing techniques [42]. SAR processing technique requires a pulsed system. Holography is originally an optical technology [43], which was mature by the 1960s and 1970s. Later on this technique was extended to microwave band and used for microwave holographic metrology [44]. Microwave holographic imaging was developed for concealed weapon detection by Pacific Northwest National Laboratory (PNNL) [21].

A non-imaging based active technique used for concealed target detection is called TDS (Time Domain Spectroscopy), in which a THz wide band pulse is used as the interrogation signal and the received pulse is analyzed and from the THz absorption spectra a certain type of explosive can be identified. TDS technology has been commercialized by *Teraview* [25].

For passive imaging, the image is formed pixel by pixel, the brightness at each pixel is determined by the spectrum density. Data processing is simple, but calibration for all receiving channels is very important. There are two possible receiving types, one is direct receiving, the other one is heterodyne receiving. Temporal and temperature sensitivity requirements for receiving components are high. Wide band active illumination source can be used to ease the low receiving signal issue, here the active illumination can be considered as random natural illumination, which differs from the synchronized active illumination for the microwave holography approach.

1.4 Motivation of the research

Concealed target imaging involves several areas of research, for example, the optimum operation spectrum, the system architecture, the component development and data processing. The comparison of different imaging techniques is necessary, the advantages and disadvantages of different techniques need to be understood. Manufacturing of imagers is expensive and they are currently physically large, the endeavour of cost reduction and miniaturization is worthwhile. This includes the investigation of low profile component, and the optimum system parameters. Based on literature surveys and first hand experimental results, this thesis aims to provide system level parameter determination to aid the development of a target detection imager.

1.5 Outline of thesis

In chapter 1, an overview of the technologies used in CWD systems based on the survey in the open literatures is performed. It is concluded that the imaging based MMW imager combined with the EM resonance based target detector offers the best solution in terms of penetration and resolution. Technical issues surrounding such a system are reviewed and discussed. The proposal for the research and the layout of the thesis are described.

In chapter 2, two classes of MMW imagers, i.e, passive and active imagers, and their technical choices and parameters are discussed. It is determined that microwave holographic approach can meet the requirements for CWD operation. Based on this, a MMW imager, operating at 94 GHz, using microwave holography, employing mechanical scan is designed. Such an experimental system allows conceptual designs to be validated for all the investigations that will be performed in proceeding chapters.

In chapter 3, based on the active, coherent, single frequency operation imaging system designed in chapter 2, an imaging array concept was raised and its parameters such as array element spacing, array dimension, imager resolution are verified experimentally. Experimental trade-off investigation of image quality against inclination angles and transmission powers are conducted. The results achieved provides important system parametres for real system implementation.

Chapter 4 concentrates on the imager performance evaluation. A variety of targets and their combinations are used to simulate real scenarios which allows to evaluate the designed MMW imager qualitatively. To quantitatively assess the imager performance, two methods are used: 1. Imager resolution estimation using point spread function (PSF) by measuring a knife edge with a tilt angle of 2 degrees. 2. Calculate the image signal to noise ratio (SNR_I) and noise equivalent reflectivity difference (NEΔR) of a copper slab target. This is a direct method to assess the imager performance.

In chapter 5, cost reduction and imaging enhancing techniques are investigated, this includes the examining of an imaging array concept using woodpile EBG lens and waveguide, the sparse array geometry for cost reduction and the multiple frequencies operation for image enhancement.

In chapter 6, an in-depth investigation of CNR (complex natural resonance) frequency extraction based target recognition technique is performed. Through the investigation, it is concluded that such a system can be used for target detection but with a poor false alarm rate. But this drawback can be overcome if combined with the MMW imaging based system.

In chapter 7, based on the investigations, two possible imager configurations are proposed. The first is based on a conventional waveguide array feeding a focused reflector antenna system to illuminated a body at a stand-off distance of 2-3 meters. The second uses the same configuration but replaces the complex and expensive waveguide array with an array-on-a-chip solution. Both system parameters are derived based on the results achieved in previous chapters. The deployment of the resonance based target recognition is also discussed.

In chapter 8, conclusions are drawn, discussions of remaining issues and an outlook for further investigations are made.

References

[1] *http://www.homeoffice.gov.uk/counter-terrorism/*

[2] Committee on Assessment of Security Technologies for Transportation National Material Advisory Board, Division on Engineering and Physical Sciences; *Assessment of Millimetre-wave and Terahertz Technology for Detection and Identification of Concealed Explosives and Weapons* The National Academies Press, Washington, D.C.

[3] Costianes, P.J.; *An overview of concealed weapons detection for homeland security* Applied Imagery and Pattern Recognition Workshop, 2005. Proceedings. 34th. Digital Object Identifier: 10.1109/AIPR.2005.17 Publication Year: 2005. Page(s): 5 - 6.

[4] Agurto, A.; Yong Li; Gui Yun Tian; Bowring, N.; Lockwood, S.; *A Review of Concealed Weapon Detection and Research in Perspective* Networking, Sensing and Control, 2007 IEEE International Conference on. Digital Object Identifier: 10.1109/ICNSC.2007.372819 Publication Year: 2007. Page(s): 443 - 448.

[5] Paulter, N. G.; *Guide to the Technologies of Concealed Weapons and Contraband Imaging and Detection* National Institute of Justice Guide 602-00, February 2001, pp. 33 - 50.

[6] Nelson, C. V.; *Metal Detection and Classification Technologies* Johns Hopkins APL technical Digest, Vol. 24. Number 1, 2004. pp.62-66.

[7] Nelson, C. V.; *Wide-Area Metal Detection System for Crowd Screening* in Proc. SPIE AeroSence 2003 Conf. Sensors and Command, Control, Communication, and Intelligence (C3T) Technologies for Homeland Defense and Law Enforcement II, Orlando, FL(22-25 Apr 2003).

[8] Achanta, A.; McKenna, M.; Heyman, J.; Rudd, K.; Hinders, M.; Costianes,P.; *Non-linear Acouustic Concealed Weapons Detections* 34th Applied Imagery and

Pattern Recognition Workshop (AIPR05), 2005, pp. 21-27.

[9] Baum, C. E.; *On the singularity expansion method for the solution of electromagnetic interaction problem* Air Force Weapons Lab. Interaction Notes, Note 88, (Dec. 1971).

[10] Baum, C. E.; *The Singularity Expansion Method* Chapter 3 of Transient Electromagnetic Fields. Publiser: Springer Berlin/Heidelberg. ISSN: 1437-0859. Volume: 10/1976.

[11] AKELA; *US Department of Justice Final Report-Demonstration of a Concealed Weapons Detection System Using Electromagnetic Resonances* January 2001 [Online]. http://www.ncjrs.org/pdffiles1/nij/grants/190134.pdf

[12] Chuang, C.W.; Moffatt, D.L.; *Natural Resonances of Radar Targets Via Prony's Method and Target Discrimination* Aerospace and Electronic Systems, IEEE Transactions on. Volume: AES-12, Issue: 5. Digital Object Identifier: 10.1109/TAES.1976.308260. Publication Year: 1976. Page(s): 583 - 589.

[13] Mackay, A.; McCowen, A.; *An improved pencil-of-functions method and comparisons with traditional methods of pole extraction* Antennas and Propagation, IEEE Transactions on, Volume: 35. Issue: 4. Publication Year: 1987. Page(s): 435 - 441.

[14] Rothwell, E.; Kun-Mu Chen; Nyquist, D.; *Extraction of the natural frequencies of a radar target from a measured response using E-pulse techniques* Antennas and Propagation, IEEE Transactions on. Volume: 35. Issue: 6. Publication Year: 1987. Page(s): 715 - 720.

[15] Turhan-Sayan, G.; Kuzuoglu, M.; *Pole estimation for arbitrarily-shaped dielectric targets using genetic algorithm-based resonance annihilation technique* Electronics Letters. Volume 37. Issue 6. 15 Mar 2001. Digital Object Identifier 10.1049/el:20010274. Page(s):380 - 381.

[16] Harmer, Stuart; Andrews, David; Bowring, Nicholas; Rezgui,Nacer; South-

gate, Matthew; *Ultra wide band detection of on body concealed weapons using the out of plane polarized late time response* Millimetre Wave and Terahertz Sensors and Technology II, Vol.7485, No.1.(2009), 748505.

[17] Rosenblum, E. S.; *Atmospheric absorption of 10-400 kMCPS radiations: Summary and bibliography to 1961* Microwave Journal. Mar. 1961.

[18] Appleby, Roger; Bruce Wallace, H.; *Standoff Detection of Weapons and Contraband in the 100 GHz to 1 THz region* IEEE Transactions on antennas and propagation. Vol. 55, No. 11, November, 2007.

[19] Alabaster, Clive M.; *The Microwave Properties of Tissue and Other Lossy Dielectrics* Cranfield University, PhD. Thesis, March, 2004.

[20] Bomomey, Jean-Charles; Pichot, Christian; *Microwave tomography: From theory to practical imaging systems* International Journal of Imaging Systems and Technology, volume 2, issue 2. Page: 144 - 156.

[21] Sheen, D. M.; McMakin, D. L.; Hall, T. E.; *Three-dimensional millimeter-wave imaging for concealed weapon detection* Microwave Theory and Techniques. IEEE Transactions on. Sept. 2001. Page(s):1581 - 1592. Digital Object Identifier 10.1109/22.942570.

[22] Appleby, R.; Anderton, R.N.; *Millimeter-Wave and Submillimeter-Wave Imaging for Security and Surveillance* Proceedings of the IEEE Volume 95, Issue 8, Aug. 2007. Page(s):1683 - 1690.

[23] Stanko, S.; Notel, D.; Wahlen, A.; Huck, J.; Kloppel, F.; Sommer, R.; Hagelen, M.; Essen, H.; *Active and passive mm-wave imaging for concealed weapon detection and surveillance* Infrared, Millimeter and Terahertz Waves, 2008. IRMMW-THz 2008. 33rd International Conference on.

[24] *http://www.walleyetechnology.com*

[25] *http://teraview.com/terahertz/id/20*

[26] Mochizuki, K.; Aoki, M.; Tripathi, S. R.; Hiromoto, N.; *Polarization-changeable*

THz time-domain spectroscopy system with a small incident-angle beam-splitter Infrared, Millimeter, and Terahertz Waves, IRMMW-THz 2009, 34th International Conference on, 21-25 Sept. 2009 Page(s):1 - 2. Digital Object Identifier 10.1109/ICIMW.2009.5324747.

[27] Kleine-Ostmann, T.; Knobloch, P.; Koch, M.; Hoffmann, S.; Hofmann, M.; Hein, G.; Pierz, K.; *Compact and cost-effective continuous wave THz imaging system* Lasers and Electro-Optics, 2002. CLEO '02. Technical Digest. Summaries of Papers Presented at the 2002. Page(s):405-406. vol.1 Digital Object Identifier 10.1109/CLEO.2002.1034135.

[28] Gerecht, Eyal; *A Passive Heterodyne Hot Electron Bolometer Imager Operating at 850 GHz* IEEE Transactions on microwave theory and techniques, vol. 56, NO. 5, May 2008.

[29] Kohler Rudeger; Tredicucci, Alessandro; Beltram, Fabio; Beere, Harvey E.; Linfield, Edmund H.; Davies, A. Giles; Ritchie, David A.; Iotti, Rita C.; Rossi, Fausto; *Terahertz semiconductor-heterostructure laser* Nature, vol. 417, no. 6885. Page(s) 156 - 169. May 2002.

[30] *http://www.independent.co.uk/news/obituaries/sir-godfrey-hounsfield-550312.html*

[31] *http://eur-lex.europa.eu/LexUriServ/LexUriServ.do?uri=OJ:L:2004:159:0001:0026:EN:PDF*

[32] Mann, C.; *Real time passive imaging at 250GHz for security: Technology and phenomenology* Electromagnetics in Advanced Applications, 2009. ICEAA '09. International Conference on, pp.1013-1015, 14-18 Sept. 2009.

[33] Korneev, D.O.; Bogdanov, L. Yu.; Nalivkin, A. V.; *Passive millimeter wave imaging system with white noise illumination for concealed weapons detection* Infrared and Millimeter Waves, 2004 and 12th International Conference on Terahertz Electronics, 2004. Conference Digest of the 2004 Joint 29th Interna-

tional Conference on. 27 Sept.-1 Oct. 2004. Page(s):741 - 742. Digital Object Identifier 10.1109/ICIMW.2004.1422305

[34] Kozakoff, D. J.; Tripp, V.; *Antennas for concealed weapon detection* 5th International Conference on Antenna Theory and Techniques, Kyiv, Ukraine: 24-27 May, 2005.

[35] Anderton, R. N.; Appleby, R.; Borrill, J. R.; Gleed, D. G.; Price, S; Salmon, N.A.; Sinclair, G. N.; Lettington, A. H.; *Prospects of imaging applications [military]* Terahertz Technology and Its Applications, IEE Colloquium on. Digest No: 1997/151.

[36] Currie Nicholas, C.; Brown, Charles E.; *Principles and Applications of Millimetre-wave Radar* Artech House, Boston, 1987.

[37] Sinclair, G. N.; Anderton, R. N.; Appleby, R.; *Outdoor passive millimetre wave security screening* Security Technology, 2001 IEEE 35th International Carnahan Conference on. 16-19 Oct, 2001. Page(s):172 - 179. Digital Object Identifier 10.1109/.2001.962830.

[38] Novak, D.; Waterhouse, R.; Farnham, A.; *Millimetre Wave Weapons Detection System* Proceedings of the 34th Applied Imagery and Pattern Recognition Workshop, US, 2005.

[39] Murphy, K. S. J.; Appleby, R.; Sinclair, G.; McClumpha, A.; Tatlock, K.; Doney, R.; Hutcheson, I.; *Millimetre wave aviation security scanner* Security Technology, 2002. Proceedings. 36th Annual 2002 International Carnahan Conference on. 20-24 Oct. 2002. Page(s):162 - 166. Digital Object Identifier 10.1109/CCST.2002.1049244.

[40] Lffler, T.; *Towards Real-Time Active THz Range Imaging for Security Applications* 5th ESA Workshop on Millimetre Wave Technology and Applications and 31st ESA Antenna Workshop, 18 - 20 May, 2009. ESTEC, Noordwijk, The Netherlands.

[41] Basili, P.; Capom, M.; Bonafoni, S.; Mattioli, V.; *Integration of digital elevation data scanning 3D and interferometric SAR systems* Geoscience and Remote Sensing Symposium, 2004. IGARSS 04. Proceedings. 2004 IEEE International. Volume 5, 2004 Page(s):2811 - 2814. Digital Object Identifier 10.1109/IGARSS.2004.1370276.

[42] Cumming, Ian G.; Wong, Frank H.; *Digital processing of synthetic aperture radar data* Artech House, 2005. ISBN 1-58053-058-3.

[43] Stephen A.; Benton, V.; Michael Bove Jr.; *Holographic Imaging* Wiley, 2007. ISBN 978-0-470-06806-9.

[44] Slater, Dan; *Near-field antenna measurement* Artech House, 1991. ISBN 978-0-470-06806-9.

Chapter 2

Millimeter Wave Imaging Systems

2.1 Introduction

In chapter 1, we have performed a comprehensive review of the technologies that are commonly used for CWD detection and identified that MMW based imaging is promising to provide a possible solution mainly due to the resolution and penetration ability that it can offer. Also, a wide range of issues surrounding MMW imaging were reviewed and discussed. As stated in Chapter 1, there are mainly 4 types of MMW technology based imagers, i.e. microwave/MMW radar imager, broadband/Noise pulse MMW imager, microwave holography imager, and passive MMW imager. According to the nature of the illumination sources, the first three classes are active MMW imaging and the fourth one is passive MMW imaging. For the three active MMW imagers, the microwave/MMW radar imager is an object locator based on conventional pulsed radar techniques, calculating range and Doppler shifts of moving targets. The broadband/Noise pulse MMW imager differs from the passive MMW imager only in the way that there is an artificial illumination in the former. In this chapter, only the third type of active imager is used to compare to the passive MMW imager.

Compared to resonance based target identification techniques, imaging based MMW CWD are more intuitive and generally complex and expensive. In this chapter, we will further narrow down the list of techniques that can be used for CWD within the category of MMW imaging. This is done by comparing the two general classes of MMW detection techniques, i.e. passive imaging and active imaging. Their respective advantages and disadvantages with respect to the applications/scenarios will be identified.

Afterwards, the design of an active, coherent imager based on microwave holography is described. A prototype MMW imager based on such a design is constructed, and will be deployed for the investigations that will be performed in subsequent chapters.

2.2 The scenario assumed

One obvious advantage for MMW imaging over optical imaging is its penetration ability. MMW imaging applications such as concealed weapon detection [1–4] (penetrating the clothing), MMW radar aided landing [5] (penetrating cloud), remote sensing [6] (penetrating fog and rain), etc. are based on this feature. Depending on the applications the imaging system requirements are different. At this stage of the research, we concentrate on the CWD deployment environments for airport and railway station. These transport hubs are economically important and are often targeted by terrorists.

1. It is an indoor environment with poor natural millimetre wave illumination.
2. It is a controlled environment, individuals are required to enter a portal-style security checking system.
3. Medium range of detection is required.
4. The imager is required to form images for both metallic and non-metallic objects concealed within a clothed human body.
5. The imaging system is required to detect a target with a lateral dimension of 75mm, system resolution should achieve at least 1/7th of the target dimension i.e. around 10mm for possible visual recognition. Clutter is a term used for echoes from non-targets, in the case studied here, it refers to the returns from the background such as a human body, clothes, surrounding walls which can cause serious performance problem to the imaging system. Signal to clutter ratio required for a good image is 6:1. These are the parameters used for system analysis for a standoff imaging sensor by DARPA TIFT [7].
6. Real time imaging is required because airports and train stations are known to have large throughput.

2.3 Microwave holography

2.3.1 The evolution of Microwave holography

Holography was invented in 1947 by the Hungarian-British physicist Dennis Gabor [8], for which he received the Nobel Prize in Physics in 1971. SAR (Synthetic Aperture Radar) techniques were developed independently at about the same time and were described in terms of a range-Doppler approach. The holographic approach was first applied to a side-looking synthetic aperture radar by Leith and Ingalls [9], [10]. Although optical holography and SAR technology were developed independently, they resemble each other to a certain degree. One of the common factor between the two is that both use the off-axis reference wave principle. The SAR technique was termed by Leith [11] as quasi-holography as it utilizes pulsed radiation to measure range and doppler shifts to measure azimuth, which differs from the true holography, in which image coordinates are two orthogonal distances, both orthogonal to the radial direction.

The first published demonstration of microwave holographic imaging was given by Dooley [12] in 1965, A letter "A" of 2m in height was illuminated by a X-band source. The transmission through the target formed an on-axis Fresnel hologram field and it was mapped by an intensity probe. The reconstruction is optical, in which process a spatially-sampled representation of the x-band diffraction pattern, i.e. the hologram is scaled photographically to the appropriate optical hologram size which gives the desired focal length in the reconstruction. Since then, the two-step microwave holography evolved in both the hologram recording stage and the reconstruction stage. The recording of the holographic combination of the field scattered from the target with the reference field is directly received in amplitude and phase. The microwave image reconstruction stage based on optical diffraction reconstruction evolved to the digital processing method based on the Fast Fourier Transform algorithm that Gooley and Tukey [13] published. Originating from visible holography, microwave holography has evolved into a technique in its own right. It differs from visible holography in both of the recording step, using direct recording of amplitudes and phases instead of interference pattern recording, and the reconstruction step, using digital reconstruction instead of optical diffraction reconstruction.

2.3.2 Two system configurations of Microwave holography: receiver only scan vs transceiver scan

For the microwave holography based MMW imaging system, the recording sensors can have two configurations, i.e. receiver only scan and transceiver scan. As summarized in [14], the latter configuration can have an enhanced resolution over the former one. In the case of receiver only scan, if the number of transmitters are more than one, the averaged image of all the images by all the transmitters would have an improved resolution. However, this is pending validation. For the 94 GHz MMW holographic imager designed in this thesis, the transmitter and receiver simultaneous scan mode is used.

2.4 Passive imaging vs active imaging

MMW imaging based CWD relies on the emissivity contrast of radiation between the warmer and cooler objects or the reflectivity contrast between the target and its surrounding background for the natural illumination or an artificial illumination based on a certain waveform. Passive imaging and active imaging are compared, their fundamental characteristics, advantages and disadvantages for CWD operation will be identified.

2.4.1 Illumination

Passive imaging means the reflection from the target and background comes for free, from natural incoherent illumination and emission of the target itself. Every object generates EM radiations at all wavelengths, the intensity of the radiation is proportional to the product of the target physical temperature and its emissivity. The sum of emissivity and reflectivity for a target is 1. The proportion of emissivity and reflectivity varies as wavelength changes, for example, the human body has an emissivity of 65 percent at 100 GHz, increasing to about 95 percent at 600 GHz [7], so it will appear warmer than metals.

The fundamental difference between the passive imaging system and the active imaging system lies in the fact that there is an illumination source in the active imaging system, and because of this, active imaging has more techniques to manipulate than the passive imaging system. There is a variety of wave form selections. They can be CW, FMCW or pulse, etc.

2.4.1.1 Considerations for use

While natural illumination has the advantage of coming for free, there is one major issue that hinders its use in the indoor environment, i.e. the natural illumination would be very weak and the imaging would be mainly based on the emissivity contrast between the target and its background. This could be difficult if the physical temperature of the target and its background approaches the same. However there are advantages of using passive imaging, it poses no radiation hazard to individuals, and in the case of military applications, the imager has no emitted signature. In active systems the thermal contrast (between wanted and unwanted targets) constraint does not exist.

2.4.2 Imaging formation mechanism

The passive imaging system is analogous to the optics camera, in which the image is formed directly point by point, with each of them representing the spectrum intensity of a point in the scene. Since MMW naturally emitted by the targets is weak, the system dynamic range is generally low.

Note must be taken that the 2-D image formation mechanism for the passive imaging is different from the active microwave holography approach, in which the system records the scattered EM waves from the target over a planar aperture, with both amplitudes and phases associated with the coordinates being recorded. From this amplitude and phase information and by applying the holographic processing algorithm, the field distribution on the target surface can be calculated, therefore, 2D image is reconstructed. To record the amplitudes and phases across the aperture, a coherent system is required. Compared to the 2-D image produced by the passive system, the microwave holography approach offers high dynamic range because of the coherent summation. Furthermore, it does not require a focusing reflector/lens, so the system design can be simplified. The schematic diagrams of these two types of imaging systems are shown in Fig 2.1.

But if a collimating device is used, the focal plane imaging array would be much smaller than the pupil plane imaging array. A focal plane array approach or its variations are usually adopted. A quasi-optical collimating device is usually used to focus the weak natural emission/reflection signal from the target. The focal plane array is a staring array (distinct from scanning array in that it image the

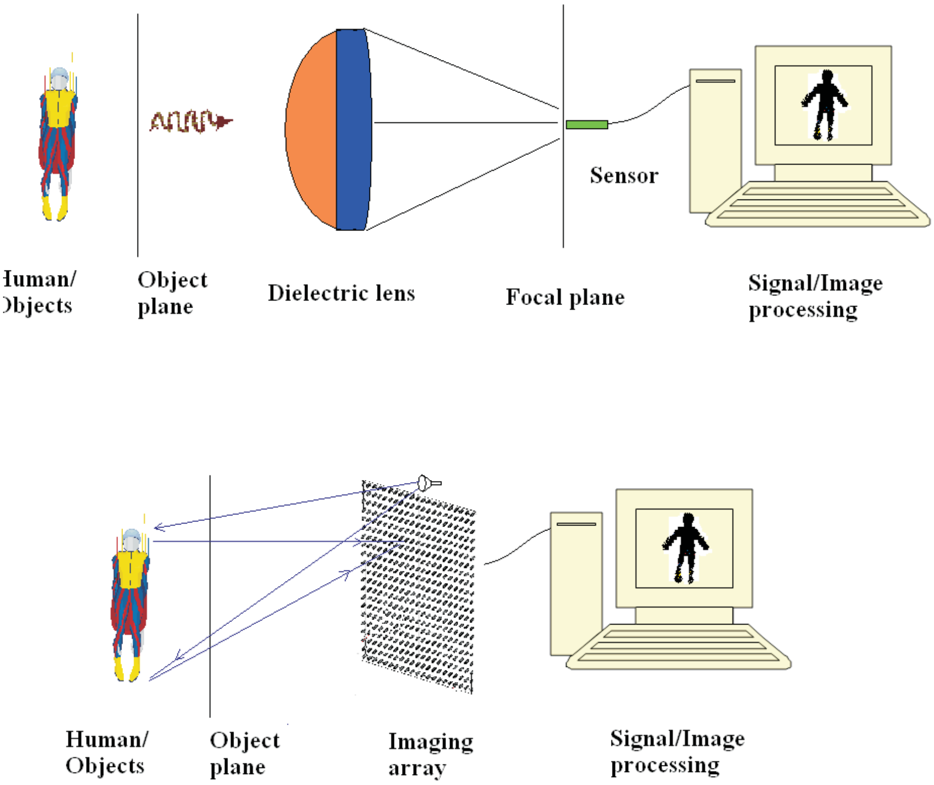

Figure 2.1: Sketches of a focal plane array based passive imaging system (upper) and a microwave holography approach based active imaging system (lower)

desired field of view without scanning), differences between responses of individual channels introduce noise to the image [4] and need to be calibrated prior to deployment.

2.4.2.1 Considerations for use

As targets RCS could vary greatly, for effective detection, a high system dynamic range is required. This can be achieved in the active, coherent microwave holography approach.

2.4.3 Direct receiving vs heterodyne

The receiving systems for passive and active imaging can be either direct or heterodyne. In [15], two W band direct detecting receivers were reported. The first one was based on a high gain (48 dB), low noise (NF 6.0 dB) amplifier and a Schottky barrier diode waveguide detector, and the second one used two 17 dB gain MMIC LNAs and a MMIC preamplified detector. Direct receiving has a few advantages such as low system temperature, no LO requirement, fewer parts, high yield and low cost, which make it suitable for the focal plane receiving array systems. Compared to direct receiving detectors, the heterodyne receiving requires a LO signal to mix with the received RF signal, the output is IF which is easier to process than the RF signal in the case of direct receiving. The Noise Figure of these systems are determined by the thermal noise, and it is always present. The lower is the system noise floor, the higher is the system sensitivity.

For the active imaging system, both the transmitter and receiver can be either be coherent and incoherent, and coherent receiving architecture is generally chosen for coherent transmission, incoherent receiving for incoherent transmission. For holographic imaging heterodyne detection is required to obtain the phase information.

2.4.3.1 Considerations for use

S/N of target and its background is another figure of interest besides reflectivity contrast between the target and its background. This is especially true for the passive imaging systems as S/N figures are generally very low in these cases which implies sensitivity requirement of detectors is high. As target RCS could vary greatly, for effective detection, a high system dynamic range is required. This can be easily achieved in the active, coherent imaging system.

Direct receiving has advantages such as low system temperature, no LO requirement, fewer parts, high yield, but the processing for the received high frequencies is difficult. For heterodyne receiving, the LO signal is required to mix with the received RF, but the advantage is the easily processed IF output.

2.4.4 Resolution

For the passive system, the angular resolution achieved by an aperture with dimension D is λ/D (see section 2.6.1), for the microwave holography with receiver only scan mode, the angular resolution achieved is the same as that of the passive system, but for the transmitter and receiver simultaneous scan, it is $\lambda/2D$.

2.4.5 Discussions, tabulation of passive and active system advantages and disadvantages

From the point of view of illumination, while passive imaging has the advantage of free natural illumination, it is not suitable for the indoor environment operation. On the other hand, active imaging uses artificial illumination and has a variety of waveforms to choose. From image forming mechanism point of view, passive images are formed pixel by pixel with poor dynamic ranges, whereas images formed by microwave holographic method have high dynamic ranges because of coherent addition. As the target RCS could vary greatly, the latter is more effective for CWD operations. Direct receiving has the advantages of no LO requirement,

Table 2-A: A comparison between passive and active imaging

	passive imaging	active imaging microwave holography
illumination	natural illumination is weak, not suitable for indoor CWD operation	artificial illumination, strong enough for indoor CWD operation
image formation	pixel by pixel, poor dynamic range	microwave holography, high dynamic range
direct receiving	1. no LO is required 2. low system temperature 3. fewer parts 4. RF output.	1 no LO is required 2. low system temperature 3. fewer parts 4. but RF output, difficult to process, rarely used.
heterodyne receiving	1. LO is required 2. IF output, rarely used.	1. LO is required 2. IF output, providing phase information for holography.
resolution	λ/D	λ/D (receiver scan only mode) λ/2D (transceiver scan mode)
flash lobes issue	no	1. Single illumination source Yes 2. Using incoherent illumination it can be overcome

low system temperature, and fewer parts, but RF output is a drawback, whereas heterodyne receiving needs the supply of LO source, but has the advantage of IF output which is easy to process. For the resolution, the angular resolution achieved by an aperture with dimension D is λ/D, for the microwave holography with receiver only scan mode, the angular resolution achieved is the same as that of the passive system, but for the transmitter and receiver simultaneous scan, it is λ/2D. For the passive system, there is no flash lobe issue, but for the single source of illumination in the active system, it is prone to such an issue, however, it can be overcome by using incoherent illumination.

2.4.6 Conclusions from comparison

From the comparisons and discussions, it is concluded that the microwave holography based active imaging system, with a CW single/multiple frequency(ies) illumination, using the heterodyne receiving architecture provides a viable solution for CWD operation for the scenarios described.

2.5 Technical challenges

Real time imaging is a challenge. Imaging can be done by scanning a single sensor across the field of view, once the data is collected the image is reconstructed by applying corresponding algorithms. However, it takes time to form an image, not practical for real-time imaging. To overcome this issue, an imaging array can be used to replace the single sensor so that the scanning time is saved or greatly reduced. An imaging array is an enabling technology to realize real time imaging.

The imaging array design issues such as spill over, side-lobe, efficiency, beam overlapping, beam separation, cross talk effect will arise [17]. Other challenges include component packaging, scanner size and cost. The use of electromagnetic bandgap (EBG) for the lens and array design provides a chance to attack the design challenge issue. Research has shown there are advantages to use EBGs such as increased directivity, less coupling between adjacent elements. More elements can be placed within a limited dimension without deteriorating the separate beam properties [18]. Active devices can be integrated with antenna radiators, thus there is less path loss of the RF signal level before it is sent to the signal processing unit.

For an imaging array, array element spacing, array dimension, number of elements are basic parameters that need to be determined before other parameters. A mechanical scan based prototype imager allows these parameters to be investigated.

2.6 The 94 GHz active prototype imager

Typical SAR systems operate in microwave band and are mainly used for earth remote sensing. The miniaturized system using MMW band frequencies (Q band, 30 GHz) was reported by Sheen [19] for security screening purposes. McMakin demonstrated a W band system in [20] and showed some details of the experimental setup, but the system parameters were not fully discussed.

When designing MMW imaging systems, system parameters such as imaging array element spacing, imaging array dimension and imaging system resolution need to be determined, operating frequency or frequencies need to be validated. In many applications where real time imaging is required, mechanical scanning should be replaced by an electronically scanned array to achieve fast imaging. In this thesis an imaging array is simulated by scanning a single transceiver. To perform the investigations, an active, coherent, single frequency MMW imaging system was developed based on the theory of microwave holography. The effectiveness of such a MMW imaging system has been demonstrated in [21, 22]. In Sheen's system [19] the wide band holography approach was adopted. The complexity of using wide band brings the benefit of speckle elimination and increased depth of focusing. However, the single frequency (95 GHz) operating system is adequate for the purpose in the investigations performed in this thesis.

2.6.1 The application of the spatial frequency concept and Nyquist sampling theorem

The essence of MMW imaging is to obtain the near field distribution on the target, however, in most cases, only the far field distribution over an aperture radiated/reflected from the object can be obtained. If a near to far field relationship can be established, then from the far field distribution the near field distribution can be calculated thus the target image can be formed.

Since the wave is propagated in a spherical wave manner, the far field is distributed in a wider area than its source (here the reflection from the target is considered as the source), so the recording aperture should be large enough to include most of energy propagated from the target. The half power beam width (HPBW) 3dB rim in the target plane defines the area to be imaged.

If the spatial to angular domain transformation is performed, the field distribution over the recording aperture can be considered as the superposition of plane waves propagated in different angular directions. see Fig 2.5, the highest possible spatial frequency $k_x = \sin(az)$ is $\sin(\pi/2)$, the unit is cycle per wavelength here. According to the Nyquist sampling theorem, the sampling density should be $1/2\sin(\pi/2)$ in order to recover the field distribution without causing aliasing. Here an assumption is made above that most of the energy reflected back from the object is included in the synthetic aperture with a limited dimension so only the low spatial frequencies exist in the aperture. Since the highest spatial frequency is limited by the lateral target dimension d and it is $\sin(d/2R)$, according to Nyquist sampling theorem, the sampling spatial frequency should not be less than $2\sin(d/2R) \cong d/R$, again the unit here is cycle per wave length. If it is expressed in distance, it becomes $\lambda \times R/d$. This is the derivation of equation (2.1).

$$\delta_L = \lambda \times R/d \tag{2.1}$$

where δ_L is the element spacing.

Assuming the distance from the image array plane to target plane is R, the cross range resolution [23] is given by equation (2.2).

$$\delta_x = \lambda \times R/2D \tag{2.2}$$

where δ_x is the lateral resolution, λ is the wavelength, R is the distance from the target to the synthetic aperture, D is the lateral dimension of the imaging array, see Fig 2.5.

Obviously the larger the dimension of the synthetic aperture D is, the finer resolution it can achieve, but since the aperture is to be replaced by an imaging array, cost and practicality for large arrays is an issue.

From equation (2.3) the required number of array elements can be calculated.

$$N = D/\delta_L = d/\delta x \tag{2.3}$$

Since the energy outside the range from $-\arctan(d/2R)$ to $+\arctan(d/2R)$ is not of interest, this allows us to use the element antenna whose HPBW is $2\arctan(d/2R) \cong d/R$. The advantage of using this narrow beam antenna is the increased signal to noise ratio of the receiver and

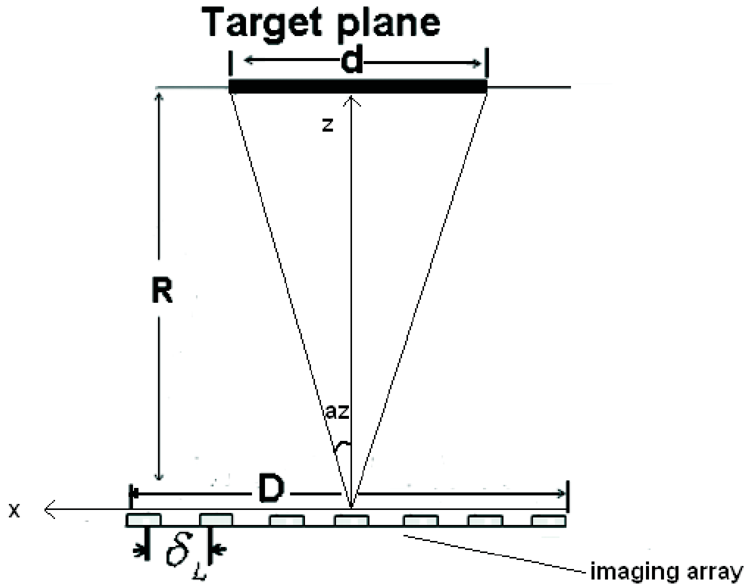

Figure 2.2: The imaging array concept

reduced clutter level from non-target area. To summarize what is stated above, the imaging array is planar and its lateral dimension is D, the array element HPBW is d/R, and the array element spacing is $\delta_L = \lambda \times R/d$.

2.6.2 The holographic processing algorithm

In microwave holography the target image is focused mathematically. See the coordinate system in Fig 2.3. The first step of the algorithm is to transform the field distribution into the angular domain as expressed in equation (2.4) [24]:

$$F(k_x, k_y) = \int\int f(x, y)e^{-i(k_x x + k_y y)} d_x d_y \tag{2.4}$$

where x, y is the position of the sampling points, k_x is the azimuth spatial frequency, k_y is the elevation spatial frequency, f(x,y) is the 2-D field distribution measured over the synthetic aperture, $F(k_x, k_y)$is the 2-D angular spectrum.

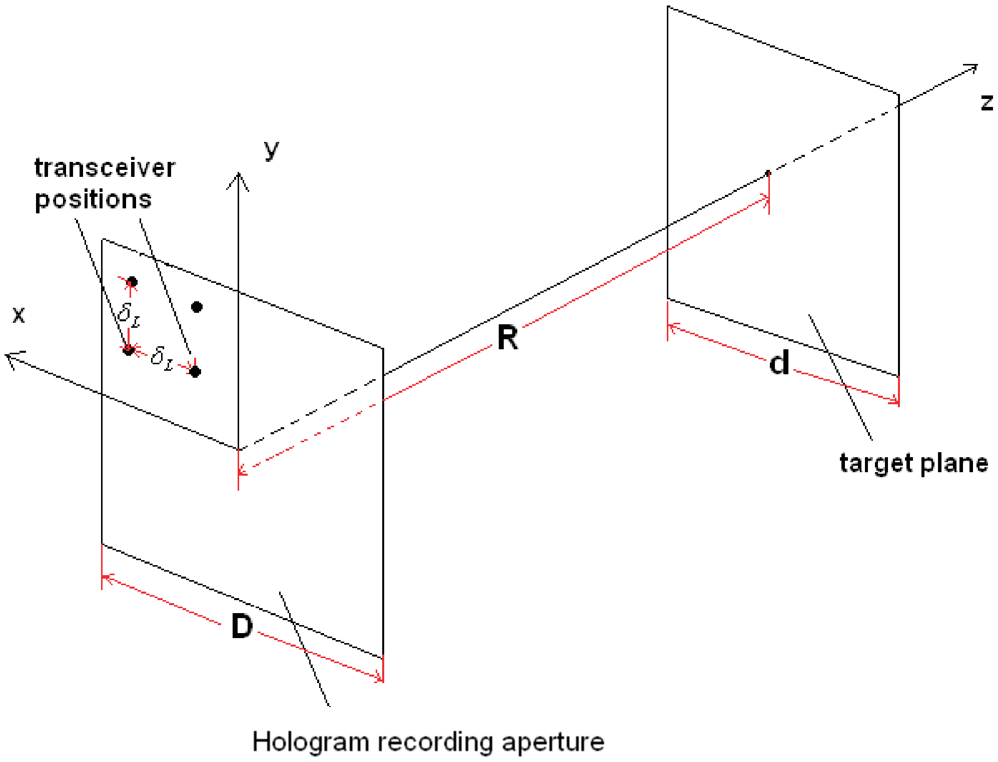

Figure 2.3: The coordinate system

Angular spectrum can be considered as the superposition of a series of plane waves which can be easily backwardly propagated. Once these plane waves are backwardly propagated into the field depth of the target, then they are interpolated in the angular frequency domain and then inversely transformed back into spatial domain. The inverse transform can be expressed in equation (2.5)and (2.6).

$$f_d(x,y) = 1/4\pi^2 \int\int F(k_x,k_y)e^{k_z d}e^{i(k_x x+k_y y)}d_{k_x}d_{k_y}; \tag{2.5}$$

$$k_z = \sqrt{4k^2 - k_x^2 - k_y^2}, k = 2\pi/\lambda \text{ [19]}. \tag{2.6}$$

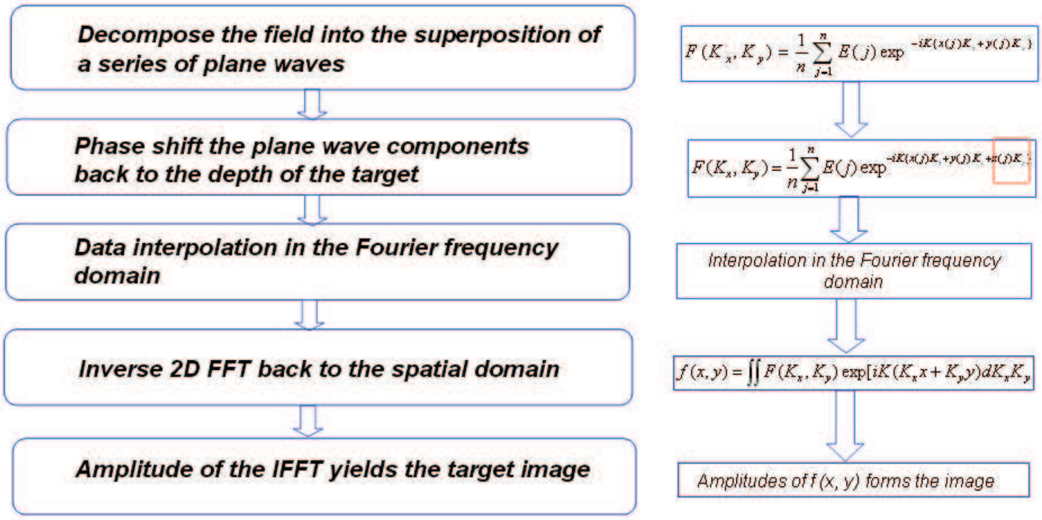

Figure 2.4: The image reconstruction procedure

where d is distance from synthetic aperture plane to target plane, $f_d(x, y)$ is the 2-D field distribution across the target plane,

The amplitudes of the inverse Fourier transform form the target. The image reconstruction procedure are summarized in Fig 2.4.

2.6.3 The MMW imaging system

The MMW imaging system can be viewed as a quasi-bistatic radar operating at 95 GHz as shown in Fig 2.5.

Fig 2.6 is the actual implementation of such a system. Agilent 8510C Vector Network Analyzer is used as the transmitter and receiver. The Hewlett Packard 83558A 75-100GHz mm-Wave Source Module provides approximately an output power of 14 dBm. HP 83558 1:10 directional coupler divided the power, delivering 1.3 dBm to the reference channel and 12.7 dBm to the transmitting horn. The transmission power can be adjusted by the attenuator. Two corrugated horns with

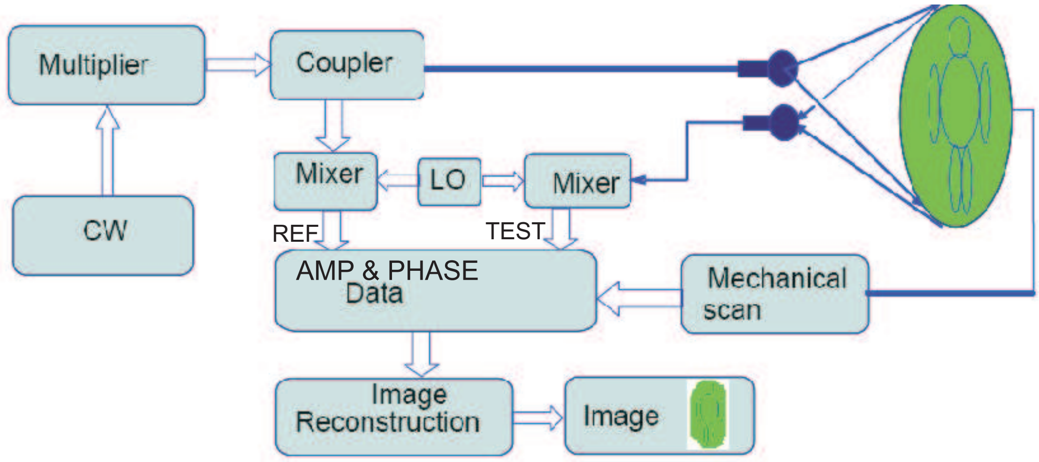

Figure 2.5: The diagram of the MMW imaging system

directivity of 22 dB are used as the tx and rx antennas. Both the transmitting and receiving antennas' far-field regions are about 1 metre away from their respective phase centres. Both tx and rx are vertically polarized. The Vector Network Analyzer receiver itself has a noise floor around -100 dB, and the whole system has a dynamic range of 60 dB. Since there is a rigid waveguide connection between the transmitting and receiving antennas and other devices, it is not feasible to scan the target in the current measurement set-up by moving the antennas up and down, instead in this prototype system, the antennas is kept still and the target is moved on the NSI 2000 x-y scanner. The whole system is placed in an anechoic chamber and so microwave absorbers forms the background. Fig 2.7 shows a photo of the prototype imager.

Microwave holography imaging is a two-step procedure. The first step is to record the hologram across the phase front recording aperture. Using the NSI 2000 measurement system (see Fig 2.8), it is simply necessary to set the parameters such as aperture dimension and sampling interval to start the scanner, and so record the hologram. A recorded hologram is shown in Fig. 2.8. The second step is raw

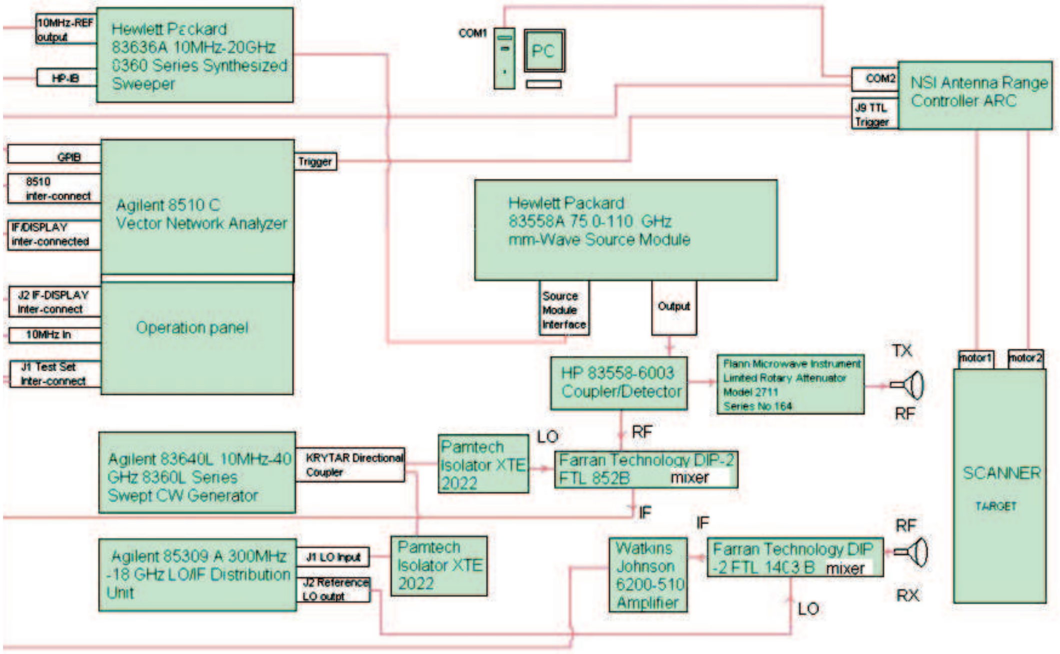

Figure 2.6: Implementaion of the 94 GHz microwave holographic imager

data processing for the recorded hologram. Using the NSI system, by setting the distance Z and number of IFFT points (see Fig 2.9), and then selecting 'Image' icon, the target image can be formed, as shown on the display in Fig 2.7.

2.7 Summary

In this chapter, a brief overview of microwave holography is conducted. The place of the MMW imager based on microwave holography within the whole family tree of holography is located. The characteristics of passive and active imagers have been summarized and compared. In terms of illumination, while passive imaging has the advantage of free natural illumination, it is not suitable for the indoor environment operation. On the other hand, active imaging uses artificial illumination and has a variety of waveforms to choose. Passive images are formed

Figure 2.7: Photograph of the 94 GHz microwave holographic imager

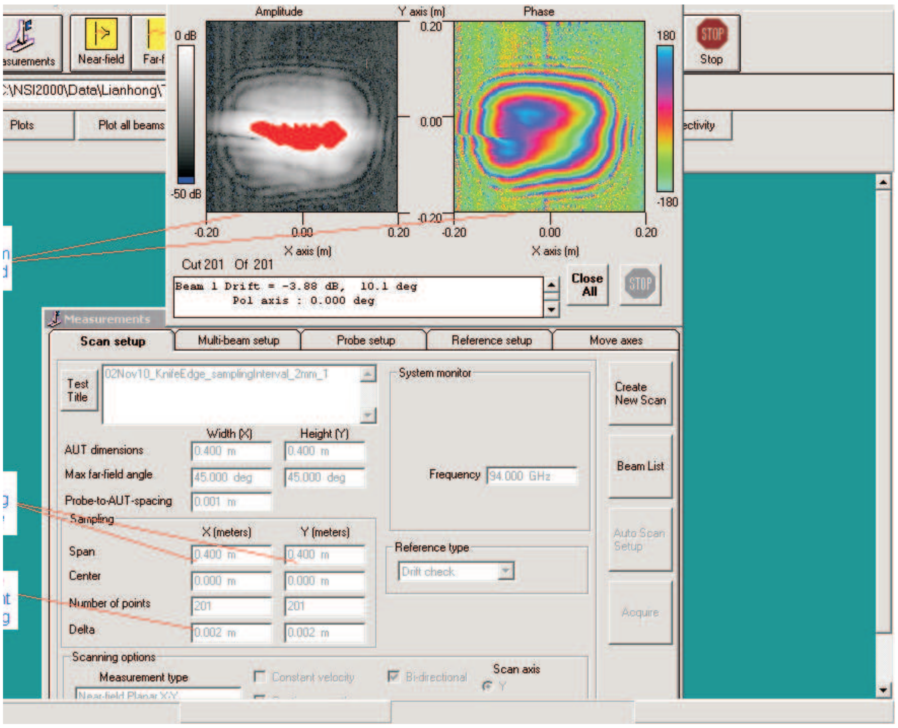

:\NSI2000\Data\Lianhong\

Cut 201 Of 201

```
Beam 1 Drift = -3.88 dB,  10.1 deg
       Pol axis : 0.000 deg
```

Test Title: 02Nov10_KnifeEdge_samplingInterval_2mm_1

	Width (X)	Height (Y)
AUT dimensions	0.400 m	0.400 m
Max far-field angle	45.000 deg	45.000 deg
Probe-to-AUT-spacing	0.001 m	

Frequency: 94.000 GHz

Sampling

	X (meters)	Y (meters)
Span	0.400 m	0.400 m
Center	0.000 m	0.000 m
Number of points	201	201
Delta	0.002 m	0.002 m

Reference type: Drift check

Scanning options

Measurement type: Near-field Planar X-Y

☐ Constant velocity

☑ Bi-directional

Scan axis: ● Y

Figure 2.8: NSI 2000 measurement system, hologram recording

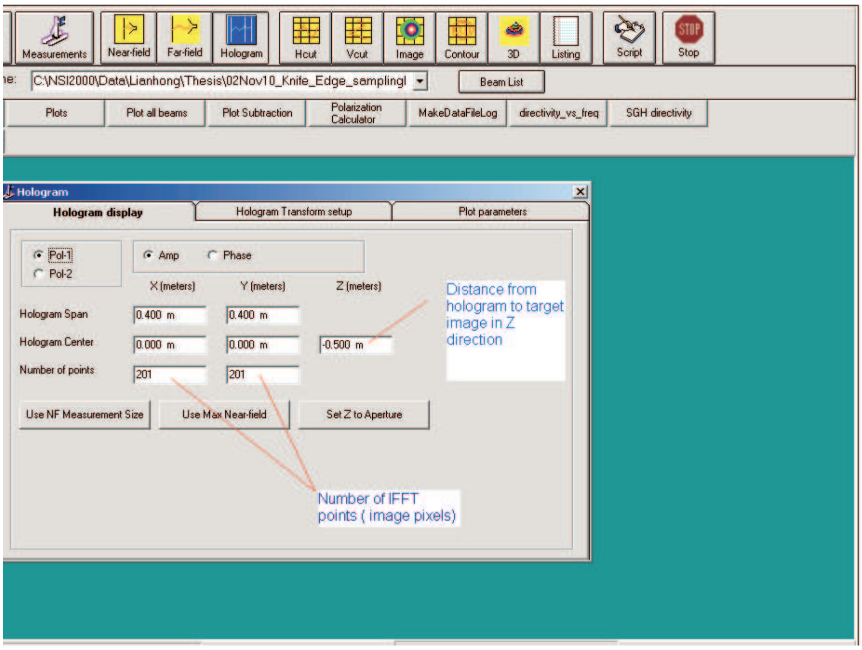

ne: C:\NSI2000\Data\Lianhong\Thesis\02Nov10_Knife_Edge_samplingl

● Pol-1
○ Pol-2

● Amp ○ Phase

	X (meters)	Y (meters)	Z (meters)
Hologram Span	0.400 m	0.400 m	
Hologram Center	0.000 m	0.000 m	-0.500 m
Number of points	201	201	

Distance from hologram to target image in Z direction

Number of IFFT points (image pixels)

Figure 2.9: NSI 2000 measurement system, image reconstruction

pixel by pixel with poor dynamic ranges, whereas images formed by microwave holographic method have high dynamic ranges. As the target RCS could vary greatly, the latter is more effective for CWD operations. Direct detector receivers need cryogenic operation to achieve high sensitivities which is a drawback, while heterodyne receiving can operate at room temperatures with high sensitivities, the latter is more viable for real system implementation. Lastly, for the same aperture dimension used, microwave holography can achieve higher resolution than passive imaging. From the comparisons and discussions, it is concluded that the microwave holography based active imaging system, with a CW single/multiple frequency(ies) illumination, using the heterodyne receiving architecture provides a viable solution for CWD operation with respect to the scenarios defined.

Based on the microwave holography theory, a prototype imager operating at 94 GHz is designed and implemented using the NSI 2000 scanner and Agilent

8510 C Vector Network Analyzer as the transmitter and receiver. Detailed system description is given. Basically the system has a dynamic range of 60 dB, an output power of 12.7 dBm. The two-step imaging procedure is also introduced, i.e, hologram recording and raw data processing. Use of the NSI 2000 Measurement system is stated. The prototype is ready to perform the investigations of interest described in the following chapters.

References

[1] Sheen, D. M.; McMakin, D. L.; Hall, T. E.; *Three-dimensional millimeter-wave imaging for concealed weapon detection* Microwave Theory and Techniques, IEEE Transactions on. Volume 49, Issue 9, Sept. 2001. Page(s):1581 - 1592. Digital Object Identifier 10.1109/22.942570.

[2] Murphy, K. S. J.; Appleby, R.; Sinclair, G.; McClumpha, A.; Tatlock, K.; Doney, R.; Hutcheson, I.; *Millimetre wave aviation security scanner* Security Technology, 2002 Proceedings. 36th Annual 2002 International Carnahan Conference on. 20-24 Oct. 2002. Page(s):162 - 166. Digital Object Identifier 10.1109/CCST.2002.1049244.

[3] Lettington, A. H.; Dun, Dennis; Attia, Magdy; Blankson, I. M.; *Passive millimetre-wave imaging architectures* Institute of Physics Publishing, Journal of Optics A: Pure and Applied Optics, 5(2003) s1-3-s110, PII:S1464-4258(03)585 38-5. [online] www.iop.org/EJ/article/1464-4258/5/4/363/oa3463.pdf

[4] Anderton, R. N.; Appleby, R.; Borrill, J. R.; Gleed, D. G.; Price, S.; Salmon, N. A.; Sinclair, G. N.; Lettington, A. H.; *Prospects of imaging applications [military]* Terahertz Technology and Its Applications (Digest No: 1997/151), IEE Colloquium on. 10 April 1997. Page(s):4/1 - 410.

[5] Korn, B.; Doehler, H. U.; *Passive landing aids for precision EVS approach and landing* Digital Avionics Systems Conference, 2003. DASC '03. The 22nd. Volume: 2. Digital Object Identifier: 10.1109/DASC.2003.1245916. Publication Year: 2003. Page(s): 9.D.1 - 9.1-8 vol.2.

[6] Nashashibi, A. Y.; Sarabandi, K.; Frantzis, P.; De Roo, R. D.; Ulaby, F. T.; *An ultrafast wide-band millimeter-wave (MMW) polarimetric radar for remote sensing applications* Geoscience and Remote Sensing, IEEE Transactions on. Volume: 40. Issue: 8. Digital Object Identifier: 10.1109/TGRS.2002.802462. Publication Year: 2002. Page(s): 1777 - 1786.

[7] Committee on Assessment of Security Technologies for Transportation National Material Advisory Board, Division on Engineering and Physical Sciences; *Assessment of Millimetre-wave and Terahertz Technology for Detection and Identification of Concealed Explosives and Weapons* The National Academies Press, Washington, D.C..

[8] Hill, P. C. J.; *Dennis Gabor - Contributions to Communication Theory and Signal Processing* EUROCON, 2007. The International Conference on; Computer as a Tool.

[9] Pasmurov, A.; Zinoviev, J.; *Radar Imaging and holography* IEE Radar, sonar and Navigation series 19, 2005, pp. 2.

[10] Leith, E. N.; Ingalls, F. L.; *Synthetic antenna data processing by wavefront reconstruction* Applied Optics, 1968, 7(3), pp. 539-44.

[11] Leith, E. N.; *Quasi-holographic techniques in the microwave region* Proc. IEEE vol. 59, 1969. pp.1305-1318.

[12] Dooley, R. P.; *X-band holography* Proceedings of the IEEE, Issue Date: Nov. 1965. Volume: 53, Issue:11. Page(s): 1733 - 1735.

[13] Puschel, M.; *Cooley-Tukey FFT like algorithms for the DCT* Acoustics, Speech, and Signal Processing, 2003. Proceedings. (ICASSP '03). 2003 IEEE Interna-

tional Conference on. Volume: 2. Publication Year: 2003. Page(s): II - 501-4 vol.2.

[14] Tricoles, G.; Farhat, N. H.; *Microwave holography - Applications and techniques* IEEE Proceedings, vol. 65, Jan. 1977, Page(s): 108 - 121.

[15] Dow, G. S.; Ton, T. N.; Wang, H.; Lo, D. C. W.; Lam, W.; Allen, B.; Tan, K.; Berenz, J.; Yujiri, L.; Mussetto, M.; Lee, P.; *W-band MMIC direct detection receiver for passive imaging system* Microwave Symposium Digest, 1993. IEEE MTT-S International. Digital Object Identifier: 10.1109/MWSYM.1993.276919, Publication Year: 1993. vol.1. Page(s): 163 - 166.

[16] Federici, John F. ; Schulkin, Brian; Huang, Feng; Gary, Dale; Barat, Robert; Oliveira, Filipe; Zimdars, David; *THz imaging and sensing for security applicationsexplosives, weapons and drugs* Semiconductor Science and Technology, Institute of Physics Publishing, doi:10.1088/0268-1242/20/7/018.

[17] Chung, Moon-Hee; Khaikin, Vladimir B.; Kim, Hyo-Ryoung; Lee, Changhoon; Kim, Kwang-Dong; Park, Kiwon; *A Next Generation Multi-Beam Focal Plane Array Receiver of TRAO for 86-115 GHz Band* Journal of Astronomy and Space Sciences, Vol. 23, no. 1. Page(s). 19-28,2006.

[18] Lee, Yoonjae; Lu, Xuesong; Hao, Yang; Yang, Shoufeng; Evans, Julian R. G.; Parini, Clive G.; *Directive Millimeterwave antennas using freeformed ceramic metamaterials in planar and cylindrical forms* IEEE International Symposium on Antennas and Propagation, San Diego, CA, USA, July 2008.

[19] Sheen, D. M., Mcmakin, D. L., Hall, T. E.; *Three-dimensional millimeter-wave imaging for concealed weapon detection* Microwave Theory and Techniques, IEEE Transactions on Volume: 49, Issue: 9, 2001. Page(s): 1581 - 1592.

[20] Mcmakin, D. L.; Sheen, D. M.; Collins, H. D.; *Remote concealed weapons and explosive detection on people using millimeter-wave holography* Security Technology, 1996. 30th Annual 1996 International Carnahan Conference. Publica-

tion Year: 1996. Page(s): 19 - 25.

[21] Zhang, L.; Hao, Y.; Parini, C. G.; Dupuy, J.; *An experimental millimetre wave imaging system* Loughborough Antenna and Propagation Conference (LAPC '08), Loughborough (United Kingdom), 17-18 March 2008.

[22] Zhang, L.; Hao, Y.; Parini, C. G.; Dupuy, J.; *An Investigation of Antenna Element Spacing on the Quality of Millimetre Wave Imaging* The 2008 IEEE APS International Symposium on Antennas and Propagation and 2008 USNC/URSI National Radio Science Meeting in San Diego, California, USA. July 05-12, 2008.

[23] Pasmurov, A.; Zinoviev, J.; *Radar Imaging and Holography* IEE Radar, sonar and Navigation series 19. 2005.

[24] Slater, Dan; *Near-Field Antenna Measurements* Artech House, Inc. 1991.

Chapter 3

Experimental System Parameters Investigation for the 94GHz MMW Holographic Imager

3.1 Introduction

In chapter 2, a MMW prototype imager based on microwave holography operating at 94 GHz has been constructed. The system description can be summarized in the TABLE 3-A. This prototype imager can be exploited to experimentally investigate system parameters. As discussed in chapter 2, an imaging array can be used to replace the single sensor mechanical scan so that the scanning time is saved or greatly reduced. An imaging array is an enabling technology to realize real time imaging. For an imaging array, the element spacing, array dimension, number of elements, are basic parameters that need to be determined before other parameters. Besides these, the spatial distribution requirement of transmitters,

Table 3-A: Summary of technical features of the 94 GHz microwave holographic prototype imager

system in use	other system choices
active	passive
Pupil plane scan	focal plane array
W band	Q band, THz
Single frequency 94 GHz, CW	Multiple frequencies, pulse
Coherent	Incoherent
Mechanical scan	beam forming, phased array
Heterodyne receiving	
system dynamic range 60 dB	
Maximum Output power 20 dBm	

the minimum required system SNR, normal operation transmission power, element antenna HPBW are also investigated and discussed. The main contribution of the investigations in the chapter is using an experimental approach to do the trade-off system parameters investigations.

As MMW images are closely related to the targets material properties, dimensions, shapes, the experimental targets description used for the investigation are provided. The spatial frequency concept is used to calculate the theoretical results of the dimension and array element spacing and these results are validated by the trade-off experimental measurement. To assist the quantitative evaluation of these MMW images, the concepts of image signal to noise ratio (SNR_I) and noise equivalent reflectivity difference (NEΔR) are introduced. These results will be used to inform the system design in chapter 7.

Table 3-B: A comparison between passive and active imaging

target	width (mm)	length (mm)	thickness (mm)
MDF gun replica	170	200	15
MDF gun replica (metallic foil wrapped)	170	200	15
copper slab	75	173	0.35
perspex slab	75	173	1.0

3.2 Target description

Four targets, i.e. a medium density fibre (MDF) gun replica, a metallic foil wrapped gun replica, a copper slab and a perspex slab, with their dimensions being listed in TABLE 3-B. The dielectric constant of MDF is comparable to that of the plastic handle of the real handgun and the material property of perspex is similar to explosive. The width of the copper and perspex slab, is the test target dimension used for imager performance assessment by the DARPA TIFT [1] program. Each of the targets is fixed to the arm of the NSI scanner for the measurements. Theoretically speaking, for the thickness near or equal to the even multiple of $1/4\lambda$, the multiple reflections from the front and the back interfaces of the slab would add up destructively, target might be invisible, however, in the real world, the material has loss, also, it would be put against the very high permittivity human body, there are minima and maxima returns existing when the thickness changes, but the minima of the return would not become zero.

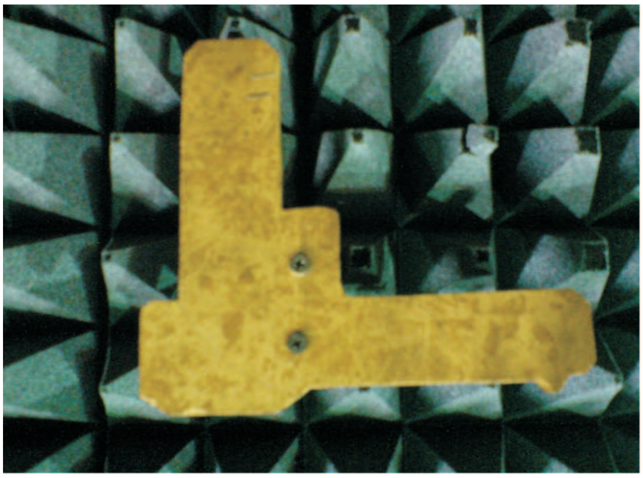

Figure 3.1: The MDF gun replica

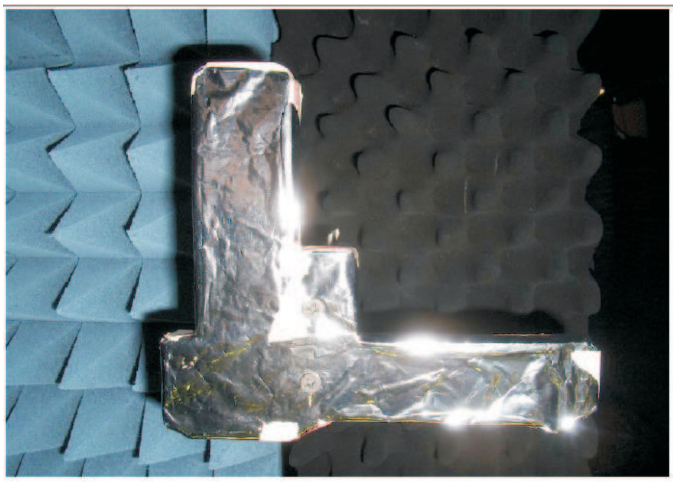

Figure 3.2: The metallic foil wrapped MDF gun replica

3.3 Image SNR and NE△R

In this chapter, MMW images will be generated. In order to quantitatively assess the quality of the images, two concepts, SNR_I and NEΔR will be introduced. SNR of the MMW images can be determined from the bright and dark areas on the image. SNR of an image is defined as the ratio of brightness' difference and the standard deviation of the dark area brightness. See equation 3.1 [2] for the

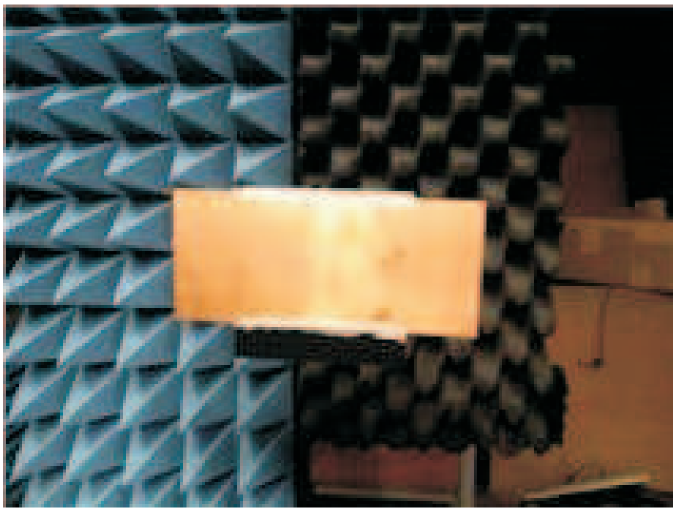

Figure 3.3: The copper slab

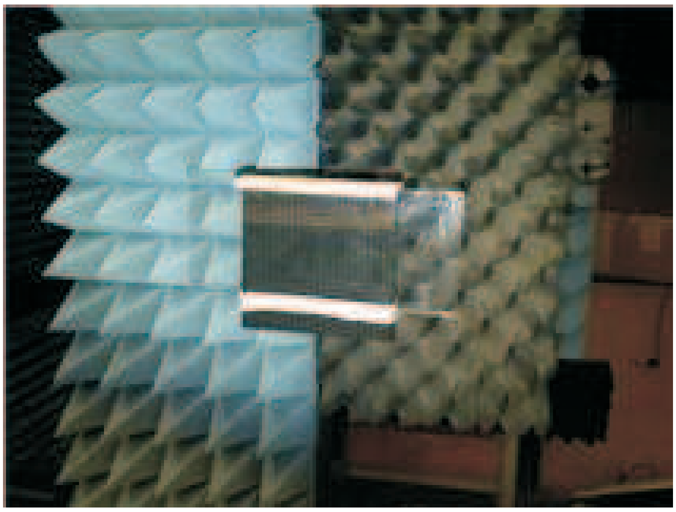

Figure 3.4: The perspex slab

mathematical expressions.

$$SNR_I = \frac{\overline{B_{bright}} - \overline{B_{dark}}}{\sigma(B_{dark})} \tag{3.1}$$

where $\overline{B_{bright}}$ and $\overline{B_{dark}}$ are the mean brightness of the target area and non-target area. $\sigma(B_{dark)}$ is the standard deviation of the dark area brightness (represented by the amplitudes of the image). Noise equivalent reflectivity difference in an image is defined in equation 3.2 and can be calculated by setting SNR_I=1.

$$NE\Delta(R) = \frac{\overline{B_{R+\Delta(R)}} - \overline{B_R}}{\sigma(\overline{B_1})} = \frac{SNR_I \sigma(B_{dark})}{\overline{B_1}} \tag{3.2}$$

where $\overline{B_{R+\Delta(R)}}$ and $\overline{B_R}$ are brightness' in areas with incremental reflectivity difference, and $\overline{B_1}$ is the brightness of the area with the reflectivity of R=1. In this case, the target area in the image is assumed to represent reflectivity of R=1, i.e., $\overline{B_1}$=$\overline{B_{bright}}$ [2]. According to Rose's Criterion [3], the contrast difference in an image detected by an observer is about 5×NEΔR. The edges between bright and dark are determined by the large areas of relatively constant maximum and minimum brightness, however, for targets with complex geometries the determination of the boundary between the target and non-target areas would be a very time-consuming job to do. A convenient way to do it is introduced in Appendix B and it is adopted for the calculations in this chapter.

3.4 Spatial frequency concept

If no multi-path and evanescent energy is present, the spatial frequency of the scattered field is 1 cycle per wavelength, thus sampling rate should not be less than 2 samplings per wavelength or 0.5 wavelength per sampling in order to retrieve the field distribution in the measurement according to the Nyquist sampling theorem. Violation of this criteria would result in aliasing in the spatial domain. In the case studied here, the recording aperture is limited in size and only the low spatial frequencies of the reflected waves can be recorded, thus the Nyquist sampling density can be lowered to 5.0 wavelengths [4] compared with the original 0.5 wavelength Nyquist sampling interval. It means that the number of sampling points (equivalent to the number of elements in the imaging array) in the measurement aperture can be greatly reduced.

Fig 3.5 is the 3-D reference coordinate system. The spatial frequency can be defined in terms of a unit length three-component vector in a right-handed coordinate system with elements.

$$k_x = \sin\theta\cos\phi, k_y = \sin\theta sin\phi, k_z = cos\theta \tag{3.3}$$

In the special case studied here, R is set as 1000 mm and the recording aperture dimension D is set as 400mm, target area d is also 400mm. Consider the 2-D case (ϕ=0), see Fig 3.6, where it should be noted here that it is a two way system, so R should be doubled which leads to $k_x = \sin\theta\cos\phi \doteq 0.1$. According to the Nyquist sampling theorem, the sampling rate should be 0.2 sampling/wavelength which means 1 sampling per 5 wavelength.

Since the highest spatial frequency exists in the recording aperture is 0.1, the high harmonics are not of interest, the beam width of the element antenna is required to cover just the target region, thus the half power beam width (HPBW) of the array element antenna can be calculated and it is arctan(0.4/1)=21.8°, a HPBW of this wide can effectively illuminate the target area even when the array element antenna is on the edge of the recording aperture. However, since microwave holography differs from the computed tomography in the way that the former relies on multipath reflection in the target area, the latter relies on direct path only, this means while wider HPBW than necessary harms the receiver S/N and collects unwanted signal from the region out of interest, a narrower HPBW

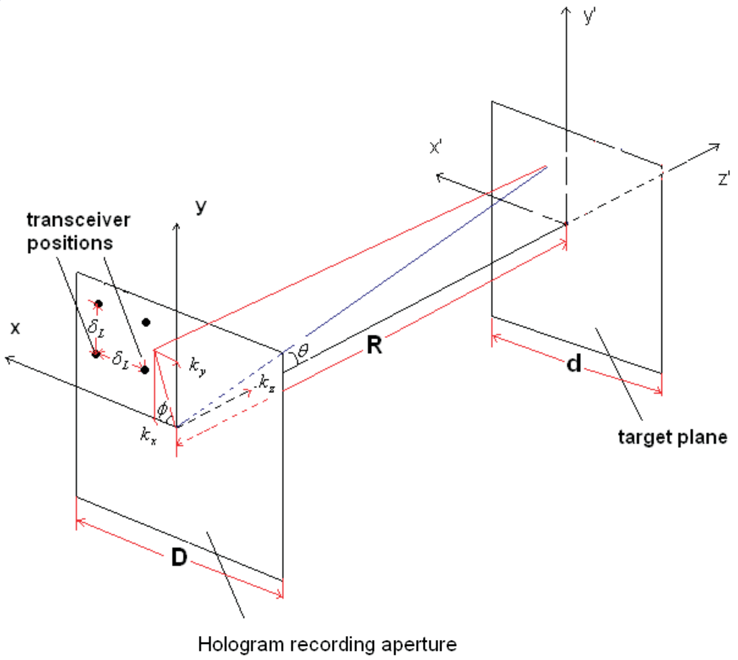

Figure 3.5: The 3-D reference coordinate system

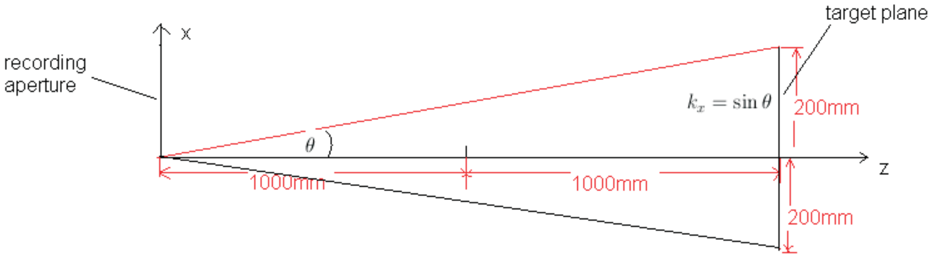

Figure 3.6: The 2-D reference coordinate system

than required for target coverage also deteriorates the imaging formation.

3.5 Array element spacing or sampling density

The procedure is to use various sampling densities from a very low rate up to the Nyquist sampling criteria, in this way the minimum required element spacing can be determined in order to reconstruct the image for a given target. This also allows

Table 3-C: experimental settings corresponding to image Fig 3.7 (a) to (g)

Figure	Total sampling points	Sampling density δ_L (λ(s) per sampling)	SNR_I	NEΔR
3.7 (a)	60×60	2.09	23.0	0.043
3.7 (b)	50×50	2.51	22.5	0.045
3.7 (c)	40×40	3.13	21.0	0.046
3.7 (d)	30×30	4.18	20.0	0.049
3.7 (e)	25×25	5.01 (theoretical prediction)	15.0	0.07
3.7 (f)	20×20	6.26	6.0	0.15
3.7 (g)	15×15	8.36	3.0	0.3

us to find out the saturation point at which there is no significant improvement in the image resolution even though the sampling density has kept increasing. Over-sampling means more receiver elements than necessary and hence increases system costs and under-sampling causes aliasing and reduced image sharpness or the contrast of the target image against its background.

The system set-up can be found in chapter 2, the MDF gun replica in Fig 3.1 is used as the target. The transmission power is set at 5 mW which is the normal transmitter output power as validated later on in this chapter. The experiment was arranged in such a way that the sampling density was set at a much higher rate than the Nyquist sampling criteria (5λ) at the beginning, then it was gradually reduced until the target image could not be correctly reconstructed. The sampling density or the imaging array element spacing details and the corresponding MMW SNR_I, $NE\Delta$R are calculated and listed in TABLE 3-C. The image quality started deteriorating (image SNR drops from 15.0 to 6.0) from Fig 3.7(e) onwards where the target was sampled at or below Nyquist sampling density. The image was completely corrupted in Fig 3.7(g) with image SNR_I just 3.0. The theoretical predictions and the experimental results agree very well.

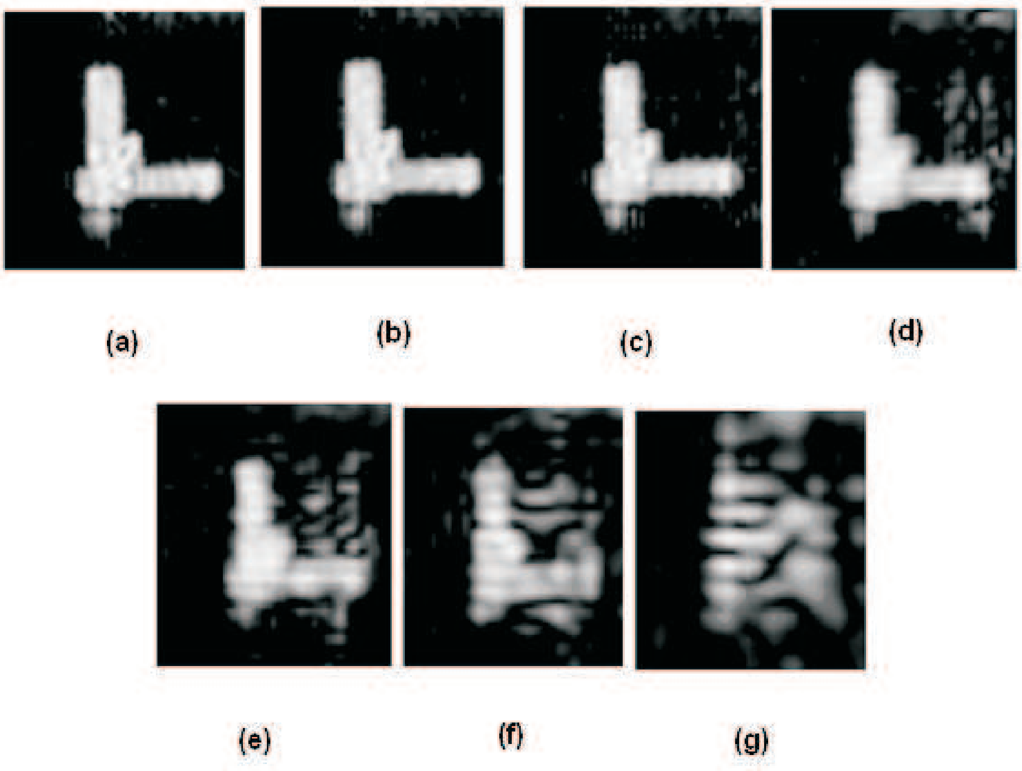

Figure 3.7: MMW images produced at different sampling points (a) 60 by 60 (b) 50 by 50 (c) 40 by 40 (d) 30 by 30 (e) 25 by 25 (f) 20 by 20 (g) 15 by 15

3.6 Required imaging array dimension

To investigate the required array dimension, the element spacing was fixed at 3.13 wavelengths then the dimension of the synthetic aperture was changed and the effect on the quality of the image was monitored. Assuming the required resolution is 8mm, by applying equation (2.2) the required synthetic dimension D can be calculated and the result is about 200mm. Aperture dimension less than this would result in a coarser resolution hence the deteriorating of the image quality. But note should be taken here, the transmitter and receiver simultaneous scan mode is adopted, the resolution achieved is higher than receiver scan only mode, in that case, aperture dimension of 400mm is required to achieve a resolution of

8mm.

The experiment was arranged in such a way that the recording aperture was set at a larger size than the required 200mm by 200mm in the beginning, then it was reduced gradually to a smaller one such that the resolution was too poor to show the detailed features.

Fig 3.8 is the optical image the MDF gun replica with a small metallic square on top and the experimental settings corresponding to Fig 3.9(a) to (i) are listed in TABLE 3-D. From Fig 3.9(a) to (g), it can be seen, as the dimension of the synthetic aperture decreases, the image quality of the target deteriorates gradually from image SNR value 20.0 to 3.0 until only part of the target can be seen. The deterioration of the image quality is due to the combined problem of resolution and dynamic range. The reduction of the recording aperture size causes the coarse resolution according to equation (2.2). In the mean time, the reduction of total number of sampling points causes the decreasing of dynamic range [5].

Fig 3.9(g) was the image obtained when the aperture dimension was set as 100mm by 100mm at a sampling density of 3.13 wavelengths. This synthetic aperture dimension was maintained and the sampling density was doubled and tripled thus the dynamic range was increased. Fig 3.9(h) and (i) show the missing part of the target image still could be recovered (no much variation of SNR_I).

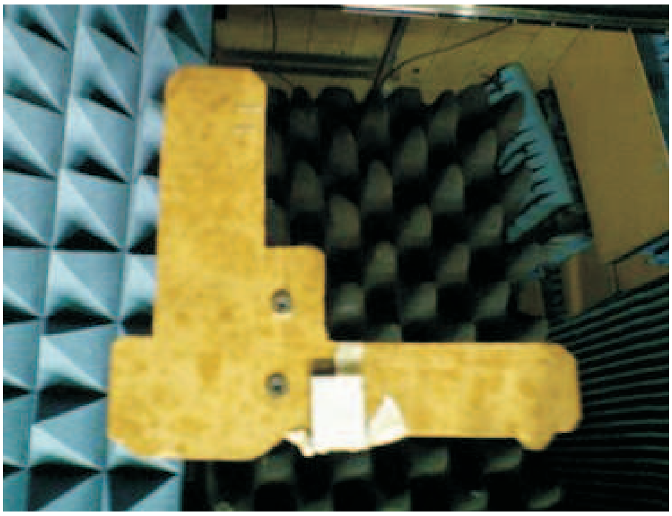

Figure 3.8: The MDF gun replica with a square metal on top

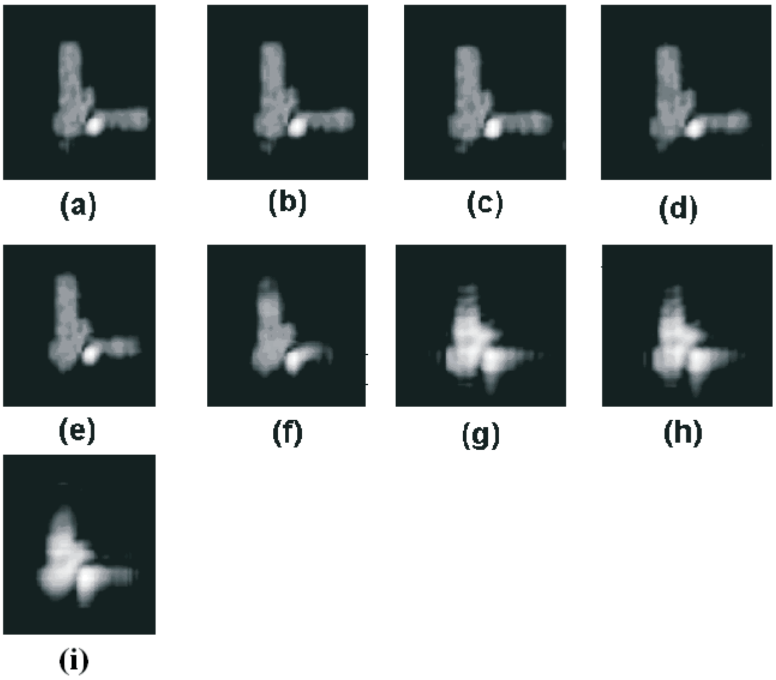

Figure 3.9: MMW images vs their aperture dimensions (a) 500mm by 500mm (b) 400mm by 400mm (c) 300mm by 300mm (d) 250mm by 250mm (e) 200mm by 200mm (f) 150mm by 150mm (g) 100mm by 100mm (h) 100mm by 100mm (i) 100mm by 100mm. Sampling density (a) to (g) 3.13 wavelengths. (h) 1.67 wavelengths. (i) 1 wavelength.

Table 3-D: experimental settings corresponding to image Figure 4.3 (a) to (i)

	Synthetic aperture dimension (mm squared)	Array element spacing (mm)	Sampling density λ(s) /cycle	SNR_I	NEΔR
Fig.3.9(a)	500 by 500	10.0	3.13	21.0	0.045
Fig.3.9(b)	400 by 400	10.0	3.13	20.5	0.047
Fig.3.9(c)	300 by 300	10.0	3.13	20.4	0.048
Fig.3.9(d)	250 by 250	10.0	3.13	20.0	0.049
Fig.3.9(e)	200 by 200	10.0	3.13	19.5	0.05
Fig.3.9(f)	150 by 150	10.0	3.13	10.0	0.1
Fig.3.9(g)	100 by 100	10.0	3.13	3.0	0.3
Fig.3.9(h)	100 by 100	5.0	1.67	3.0	0.3
Fig.3.9(i)	100 by 100	3.33	1.0	3.0	0.3

3.7 MMW images of objects with large and flat surfaces

For targets with large and flat surfaces, the reflection is mainly in the specular direction. In such cases, the target image quality is very sensitive to the normality of the target to the transmit axis. See Fig 3.10 for the tipping angle. Fig 3.11, Fig 3.12, Fig 3.13 are images reconstructed when there are just a few degrees shift from normal incidence. SNR_I, $NE\Delta$R are calculated and listed in TABLE 3-G. Fig 3.14(with SNR_I 4.0) is obtained when the tipping angle is 13.5 degrees. The shape of the target image is maintained if the tipping angle is not too large. This suggests that for targets with highly specular reflection surfaces multiple angles of illumination are needed in order to detect an arbitrary target. This work suggests angular spacing of 10 degrees between illumination ”snapshots” is required. In practise this can be achieve by using multiple transmitters with angular separation of 10 degrees.

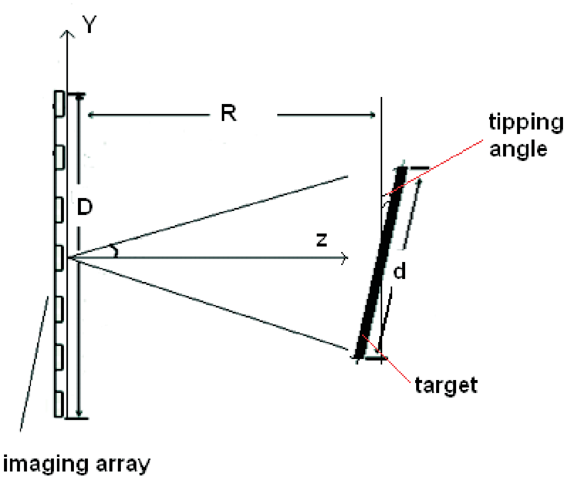

Figure 3.10: Target tipping angle from the normal incidence

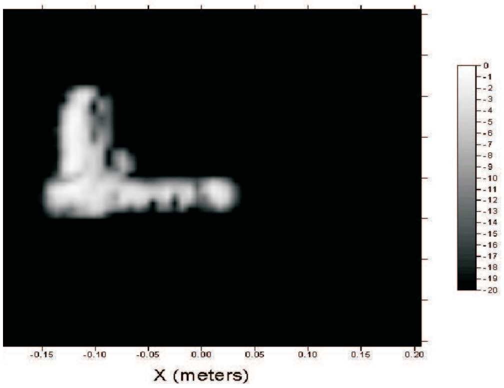

Figure 3.11: Target image in the case of 3.0 degrees shift from the normal incidence

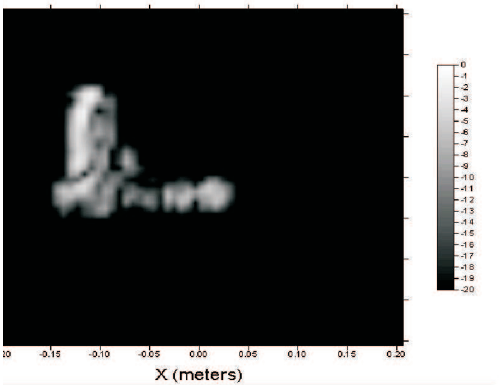

Figure 3.12: Target image in the case of 6.0 degrees shift from the normal incidence

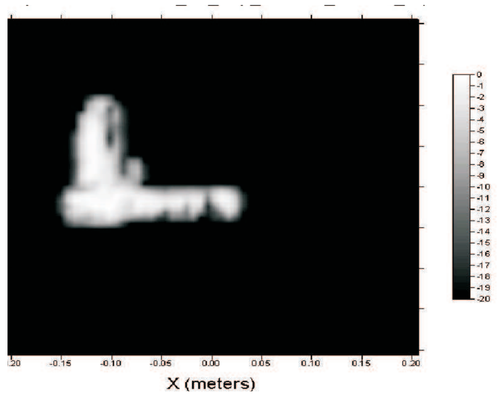

Figure 3.13: Target image in the case of 8.0 degrees shift from the normal incidence

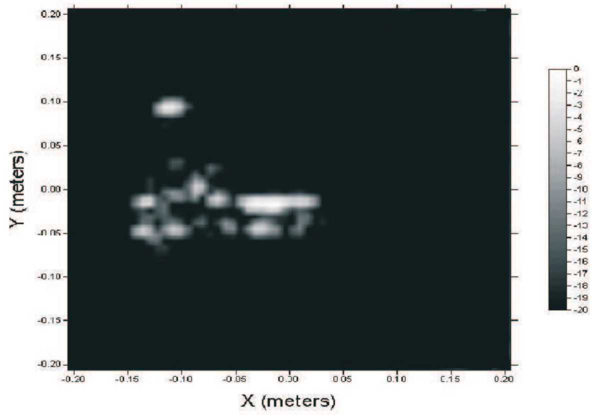

Figure 3.14: Target image in the case of 13.5 degrees shift from the normal incidence

Table 3-E: Target tipping angle vs SNR_I

MMW Image	SNR_I	$NE\Delta$R
Fig 3.11	15.4	0.06
Fig 3.12	10.5	0.1
Fig 3.13	11.9	0.9
Fig 3.14	4.0	0.25

3.8 Transmission power vs Image quality

3.8.1 Receiver SNR vs Image quality

For MMW wave imaging based detection, both receiver SNR and image SNR are of interest. In the case of passive imaging, the signal reflected or emitted for the target and its background is actually random noise. Detection of such a weak signal at microwatt level and below is particulary difficult. High performance detectors such as a Golay cell with a noise equivalent power (NEP) of $2 \times 10^{-10} WHz^{-\frac{1}{2}}$ for room temperature operation [6] are generally employed.

In the case of active imaging, receiver SNR are generally high because of the existence of the auxiliary illumination and large processing gains resulting from coherent processing (holographic and synthetic aperture, etc.) [7]. Active signals can be very easily brought up to milliwatt level.

The investigation is to validate the prototype imager has the sufficient receiver SNR for image reconstruction while the radiation power density is still under the maximum allowed $5mW/cm^2$ [8](EU standard).

Firstly, the transmit power is adjusted to the threshold level (tx power 1 dbmW and receiver SNR ranging from 7 dB to 0 dB. The receiver used here cannot display SNR below 0 dB) where the target image can just be seen (SNR_I=5.0), then the transmitting power is increased step by step until there is no obvious improvement of the image quality observed. Fig 3.15 (a) to (e) are the images produced under such an arrangement. TABLE 3-F summarizes the experiments set-ups and results.

Table 3-F: Image quality vs receiving S/N

	Receiver S/N dB	Tx power mW	SNR_I	$NE\Delta$R
Fig 3.15(a)	7	1	5.0	0.02
Fig 3.15(b)	11	5	8.3	0.012
Fig 3.15(c)	16	10	10.1	0.1
Fig 3.15(d)	21	15	20.6	0.05
Fig 3.15(e)	26	20	20.8	0.48

It can be concluded that the receiving power level must be maintained at a certain level to produce a clear image, in this particular system it is 1 mW. Note should be taken this is the output power measured at the feeder of the antenna. When it radiates into the free space in a distance (say a few meters), the power density will be several orders lower than the maximum allowed $5mW/cm^2$. In this particular system, transmission power of 5 mW is recommended.

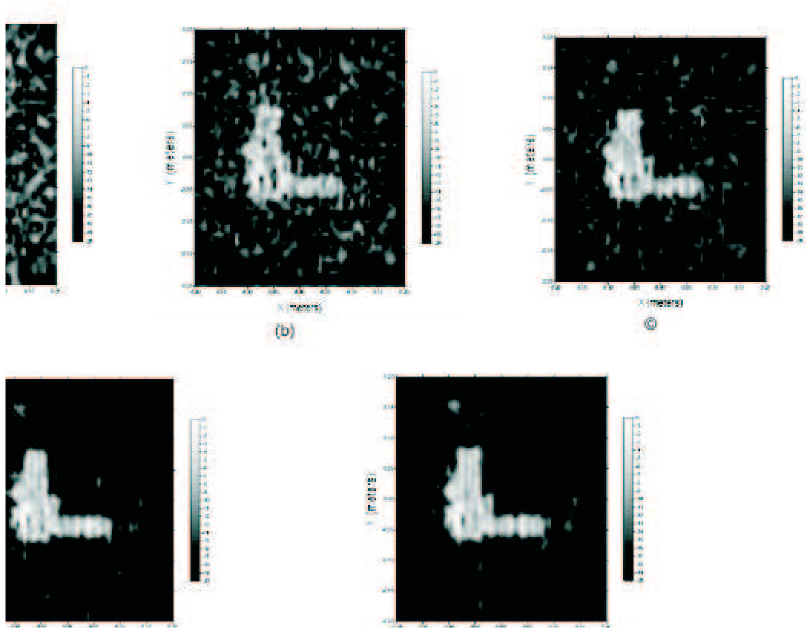

(b)

©

Figure 3.15: Image at tx power(a) 1 mW (b) 5 mW(c) 9 mW (d) 14 mW (e) 19 mW

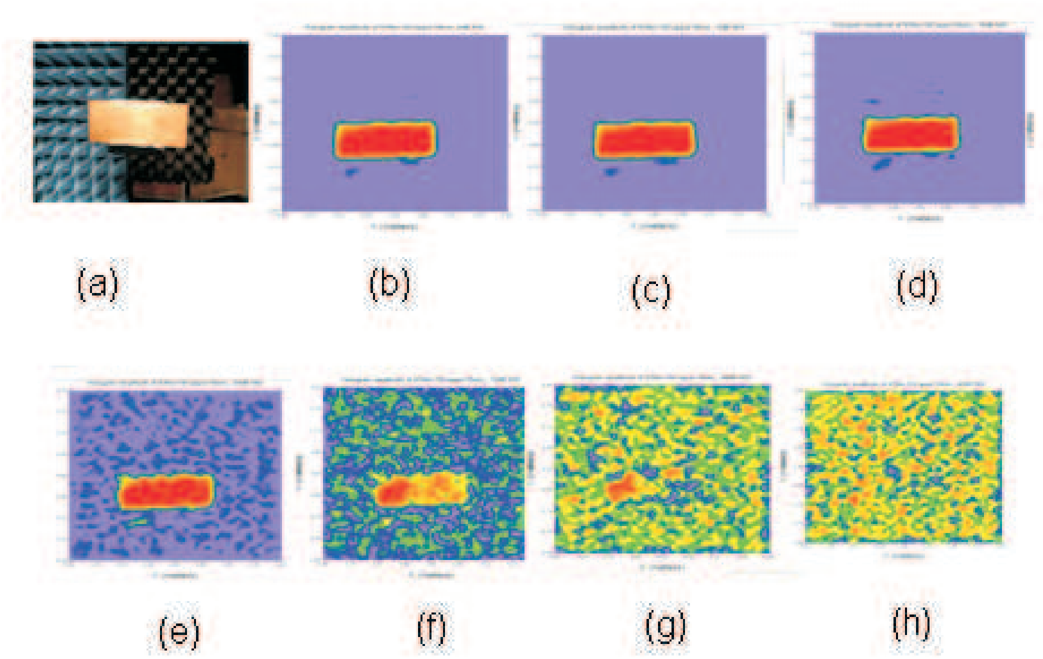
(a) (b) (c) (d)

(e) (f) (g) (h)

Figure 3.16: Copper slab (a) optical image, MMW image at tx power(b) 20 mW(c) 12 mW (d) 4 mW (e) -4 mW (f) -12 mW (g) -20 mW (h) -28 mW

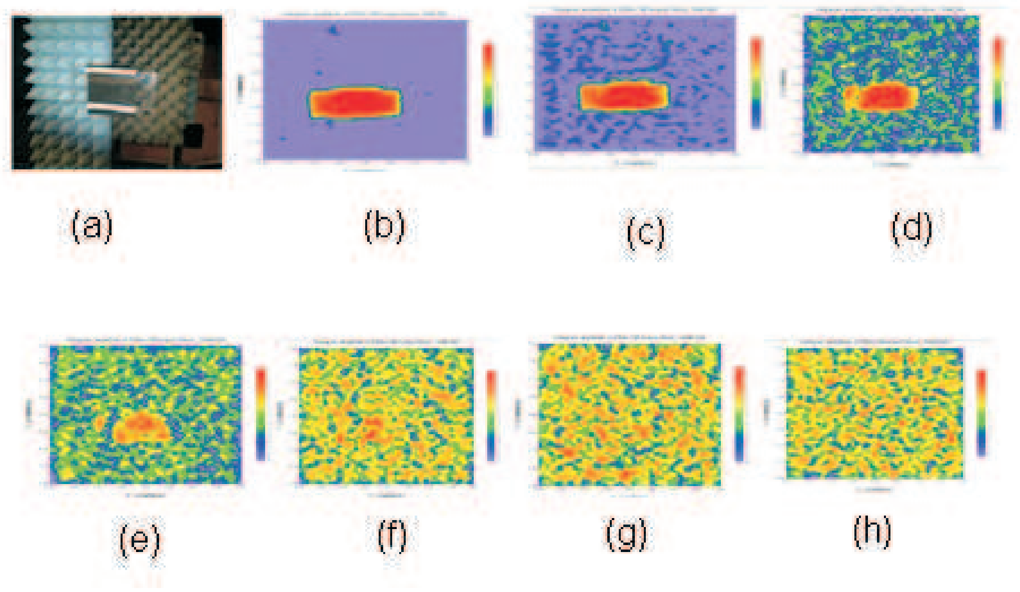
(a) (b) (c) (d)

(e) (f) (g) (h)

Figure 3.17: Perspex slab (a) optical image, MMW image at tx power(b) 20 mW(c) 12 mW (d) 4 mW (e) -4 mW (f) -12 mW (g) -20 mW (h) -28 mW

3.8.2 Transmission power vs Image quality

In this section, the relation between transmission power and image quality will be investigated. Ideally, the receiving system SNR vs image SNR relation should be investigated, but there are two reasons that this cannot be done experimentally. The first reason is that the receiver SNR is not a fixed value, it varies when the transceiver scan across the recording aperture. The second reason is that the receiving system the author used cannot display SNR values below zero. Tanninen [2] studied the system SNR and image SNR relation by artificially adding white Gaussian noise to the interference pattern, however, the author here investigates the variance of the MMW image quality as per the measurable parameter transmit power. Two targets i.e. a copper slab and a perspex slab in Fig 3.3 and 3.4 described in the target description section are used for this investigation. Fig 3.16 and 3.17 are their optical images and MMW images at different transmit power levels. Their SNR_I and $NE\Delta$R values are calculated and listed in TABLE 3-G and TABLE 3-H and Fig 3.18 is the image SNR vs transmit power plot. By visual check and SNR_I values comparison, it can be concluded that non-metallic targets cause more speckle at the same transmit power and for metallic targets, the SNR_I saturates at a lower power level, in this case, it is 5 mW for the copper slab. For the perspex slab, SNR_I never saturates within the range of power transmission studied here, but its SNR_I value manages to reach 5 which is considered acceptable for an image for recognition, at 5 mW transmission power. 5-10 mW transmission power is recommended for normal system operation in this particular prototype imager.

Table 3-G: Copper slab image quality vs transmission power

Figure	mW	SNR_I	$NE\Delta$R
Fig 3.16(b)	20	23.30	0.0419
Fig 3.16(c)	12	22.88	0.0423
Fig 3.16(d)	4	20.72	0.0453
Fig 3.16(e)	-4	11.01	0.7774
Fig 3.16(f)	-12	3.40	0.1848
Fig 3.16(f)	-20	0.3267	0.4299
Fig 3.16(h)	-28	-0.0012	0.5025

Table 3-H: Perpex slab image quality vs transmission power

Figure	mW	SNR_I	$NE\Delta$R
Fig 3.17(b)	20	18.72	0.0501
Fig 3.17(c)	12	11.32	0.0761
Fig 3.17(d)	4	4.1394	0.1630
Fig 3.17(e)	-4	1.4103	0.2920
Fig 3.17(f)	-12	0.4891	0.4024
Fig 3.17(f)	-20	0.2264	0.4535
Fig 3.17(h)	-28	-0.0070	0.5052

3.9 Discussions

The largest error source in the measurement is from the wobbling target caused by start-stop of the planar scanner motors, especially at the edge of the recording aperture. This error can be mitigated by setting a slow scan speed and dropping the data near the edge and putting the target near the center of the recording aperture. The ever present thermal noise is another source of inaccuracy of measurement, especially for the low transmission power measurement.

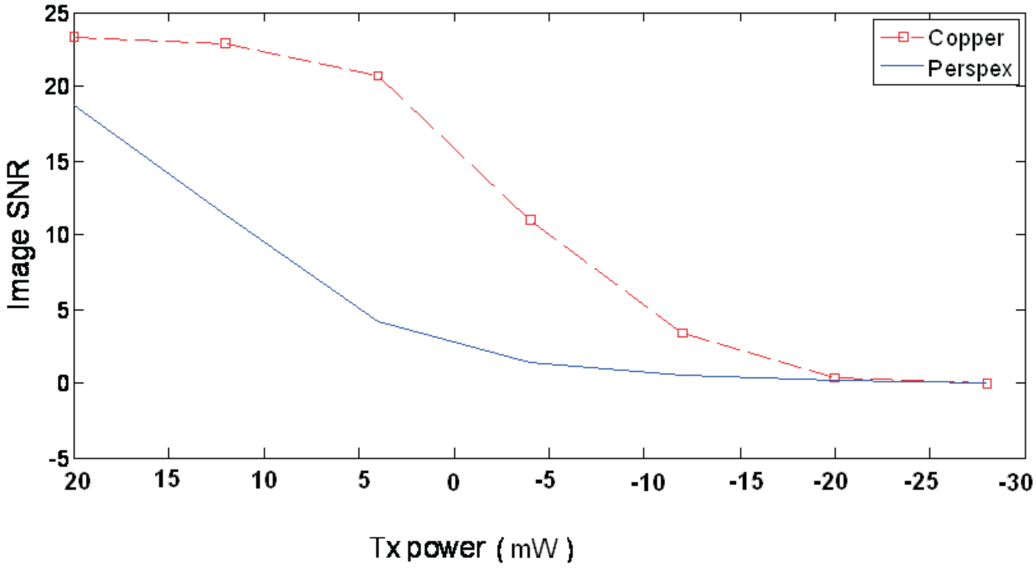

Figure 3.18: Image SNR vs transmission power

3.10 Conclusions

In this chapter, a range of system parameters are investigated. In the array element spacing investigation, the theoretical array element spacing 5λ and experimental results agrees very well. Compared to the 0.5λ array element spacing, the number of array elements are significantly reduced. In the array dimension investigation, when the dimension reduced to 200mm by 200mm, the image quality is still very good, this is due to the scan mode chosen in the measurement, which has been discussed in section 2.3.2, chapter 2. The transmitter receiver simultaneous offers higher resolution. In such a scan mode, theoretically, an aperture size of 200mm can offer a resolution of 8mm, whereas for the receiver scan only mode, it needs 400mm aperture dimension to achieve a resolution of 8 mm. For the MMW images of large and flat objects, the image quality is very sensitive to the normalities of the target to incident wave direction. 10 degrees transmitters spacing is suggested for illumination. Since the system SNR is a variable value when the transceiver

Table 3-I: Summary of system parameters

System Parameters	Quantity
imaging area	400mm×400mm
detection range	1000mm
array element spacing	5λ
array dimension	400mm×400mm
element antenna HPBW	21.8°
illumination angular spacing	less than 10°
normal system operation transmission power	5 mW
receiver SNR	above 7 dB

scans across the recording aperture, only the maximum system SNR is used for evaluation. When the transmission is 5 mW, the maximum system SNR is 11 dB for a MDF gun replica target, and at this power level, SNR_I of the copper slab saturates at 20 or so, and the SNR_I of the perspex slab is 5, which is at usable level, so 5 to 10 mW transmission power is recommended. The results achieved in the chapter are summarized in TABLE 3-I.

References

[1] Committee on Assessment of Security Technologies for Transportation National Material Advisory Board, Division on Engineering and Physical Sciences; *Assessment of Millimetre-wave and Terahertz Technology for Detection and Identification of Concealed Explosives and Weapons* The National Academies Press, Washington, D.C..

[2] Tamminen, A.; Ala-Laurinaho, J.; Risnen, A. V.; *Indirect holographic imaging: evaluation of image quality at 310 GHz (Proceedings Paper)* Proceedings Vol.

7670. Passive Millimeter-Wave Imaging Technology XIII, Wikner, David A.; Luukanen, Arttu R.; Editors, 76700A Date: 27 April 2010.

[3] Burgess, A. E.; *The Rose Model, revisited* Journal of Optical Society of America 16(3), 633-646 (1999).

[4] Zhang, L.; Hao, Y.; Parini, C. G.; Dupuy, J.; *An Investigation of Antenna Element Spacing on the Quality of Millimetre Wave Imaging* The 2008 IEEE AP-S 2008 in San Diego, California, USA. July 05-12, 2008.

[5] Slater, Dan; *Near-Field Antenna Measurements* Artech House, Inc. 1991 pp. 230.

[6] Brown, E. R.; *Fundamentals of terrestrial millimeter-wave and THz remote sensing, http://www.ece.ucsb.edu/courses/* Electrical Engineering, University of California, Los Angeles.

[7] McMillan, R. W.; Currie, N. C.; Ferris, D. D., Jr.; Wicks, M. C.; *Concealed weapon detection using microwave and millimeter wave sensors* Electrical Engineering, University of California, Los Angeles. Microwave and Millimeter Wave Technology Proceedings, 1998. ICMMT '98. 1998 International Conference on. Digital Object Identifier: 10.1109/ICMMT.1998.768213. Publication Year: 1998. Page(s): 1 - 4.

[8] *http://eur-lex.europa.eu/LexUriServ/LexUriServ.do?uri=OJ:L:2004:159:0001 :0026:EN:PDF.*

Chapter 4

The Performance Evaluation of the 94GHz MMW Holographic Prototype Imager

4.1 Introduction

In chapter 3, a range of system parameters for the 94GHz MMW Holographic prototype imager have been determined. In this chapter, we will evaluate the performance of such an imager. The evaluation methods used in this chapter are undertaken using a range of targets to simulate the real scenarios. This is the most direct way to evaluate the performance of a imager, but it is a qualitative approach. For a quantitative approach, the imager is assessed in terms of test target image SNR_I, NEΔR, and $\sigma(B_{notarget})$ and imager resolution. Two methods are used to estimate the imager resolution i.e. the Point Spread Function (PSF) estimation method and direct experimental method.

MMW imaging is based on the revealing of target reflectivity contrast against its background, so atmospheric absorption and target material property at the operating frequency (94GHz) must be understood. Atmospheric absorption across the whole electromagnetic spectrum has been long been studied and was summarized in [1]. In this chapter, since there is an active illumination source, atmospheric absorption has less impact than the material properties on the imager performance at the operation frequencies.

It is known that material properties are frequency dependent. As frequency increases, the loss tangent of the material becomes high and this weakens the penetration ability of the interrogating wave. In addition to material property, image quality is also related to target dimension and shape. When the wavelength of operation is comparable to the target dimension, resonant scattering effects may appear. Also, for the materials like fabric and clothing, the weave period could also cause resonance effect. Furthermore, for a target with mirror reflection surfaces, the reflected energy is mainly in the specular direction, which limits the field of view of detection if a single illumination source is used. All of these factors have adverse effects on the final target image quality. Despite the issues of high atmospheric absorption, high material loss tangent and potential resonance effects, a high operating frequency inherently has the advantage of high resolution, but obviously there is a trade-off here. In this chapter a prototype imaging system is used to produce realistic experimental results and thus validate the adoption of 94 GHz as the operation frequency.

Material properties of interest have been extensively studied. In [1], the emissivity, transmission, and reflectivity at various frequencies within the range from

100 GHz to 1 THz were studied, while in [2], the investigation was focused on frequencies under 100GHz. These material property investigations helps the understanding of material phenomenology and so aids imager design.

What makes the investigation unique here lies in the fact that the imager was active and the holography approach was adopted, though similar investigation has been performed in the passive imaging system. Also, this investigation differs from Tamminen's [3] in the way that the former operation frequency is 94 GHz and using transmitter and receiver in simultaneous scan mode, whereas the latter is 310 GHz and receiver only scan mode. Using test target SNR_I, NEΔR, and $\sigma(B_{notarget})$ for imager performance evaluation and determining imager resolution by PSF estimation for a 94GHz system has not been reported in the open public literature.

4.2 System set-up

The system set-up has been described in chapter 2, with the settings and configurations, unless otherwise stated, remaining unchanged. In the following measurement, the output power of the transmitter is set at 5 mW, which is the normal operation output power level validated in chapter 3.

In chapter 3, it was determined that the optimized imaging array element spacing is 3 to 4 wavelengths for an imaging array aperture dimension of 400mm by 400mm at a detection range of about 1000mm and frequency of 94 GHz. In this chapter such a system set-up will be used to demonstrate the effectiveness for concealed target detection under the following circumstances: metallic or non-metallic targets that are clothed or unclothed, placed against a human body or using anechoic chamber walls as the background. The amplitude of each pixel of the image is normalized to the highest value and the image is displayed in log scale (20 dB). The image dimension is the same as that of the scanning aperture which is 400mm by 400mm and these settings apply to all the images in this chapter.

4.3 Material phenomenology and qualitative imaging system performance evaluation

4.3.1 Target description

The targets, covers, background materials used in the measurements are listed in TABLE 4-A. Transmission coefficients of the covering materials (measured) are listed in TABLE 4-B, and targets used are listed in TABLE 4-C. The dielectric constant of MDF is comparable to that of the plastic handle of the real handgun and perspex is similar to plastic explosive in terms of dielectric constant. Cheese is similar to plastic explosive in terms of density, and since X-ray imagers detect density difference, this is a useful substitute for explosive material for system testing. However, the MMW imager detects dielectric difference, so using perspex as the target is a valid substitute material.

4.3.2 Scenario 1

Firstly, a piece of microwave absorber was used as the background. Fig 4.1(a) is the target — a MDF gun replica with a small square of metal on top of it. Fig

Table 4-A: Targets, cover, background materials used in the measurements

scenario	target	cover	background
1	a MDF gun replica a foil wrapped MDF gun replica	a suit a pullover	chamber chamber
2	a MDF gun replica	2 layers of towelling	chamber
3	a foil wrapped MDF gun replica	2 layers of towelling	chamber
4	a foil wrapped MDF gun replica	4 layers of towelling or a pullover	chamber
5	a foil wrapped MDF gun replica	a pullover	human body
6	a square of perspex with a small square of metal	a pullover	chamber
7	a square of perspex with a small square of metal	a pullover	human body
8	a square of perspex with a piece of gun shaped foil	a pullover no	human body chamber
9	a square of perspex with a foil wrapped gun replica	no	liquid
10	CD(case and disc) a foil wrapped gun replica a foil wrapped gun replica a foil wrapped gun replica	no no two layers of towelling a wool coat	chamber liquid liquid liquid
11	coin and cheese gun shaped foil and cheese gun shaped foil and cheese	no no clothing	chamber chamber chamber

4.1(c) is its MMW image. In Fig. 4.1 (b) the target is covered with cloth, and Fig. 4.1(d) is the MMW image. It can be seen that even though the target image is distorted, the gun shape is still clearly visible, especially for the small metallic square, as if the cloth were transparent. The transmission of the suit is 0.9 which causes about 1 dB loss.

Table 4-B: Transmission coefficients (measured) of the covering material used in the measurement

material	transmission
suit	0.8054
pullover	0.9423
2 layers of towelling	0.8937
4 layers of towelling	0.7779
wool coat	0.885
clothing	0.9840
leather	0.8943

Table 4-C: Targets material properties

target
MDF (thickness 15mm)
metallic foil
a square of perspex (thickness 1mm)
coin
cheese block (thickness 30mm)
human body

In Fig 4.2, a metal foil wrapped gun was used as the target to test the imaging system performance in the presence of a thick woolly cover and human body background. Fig 4.2(a) is the optical target image of the target, the chamber walls were used as the background. In Fig 4.2(b) the target was covered with a thick woolly, chamber as the background, and in Fig 4.2(c) human body background (the author) was added. Fig 4.2(d)(e)(f) are the millimetre wave images corresponding to Fig 4.2(a)(b)(c). It can be seen that the target shape can still be revealed in a very realistic situation.

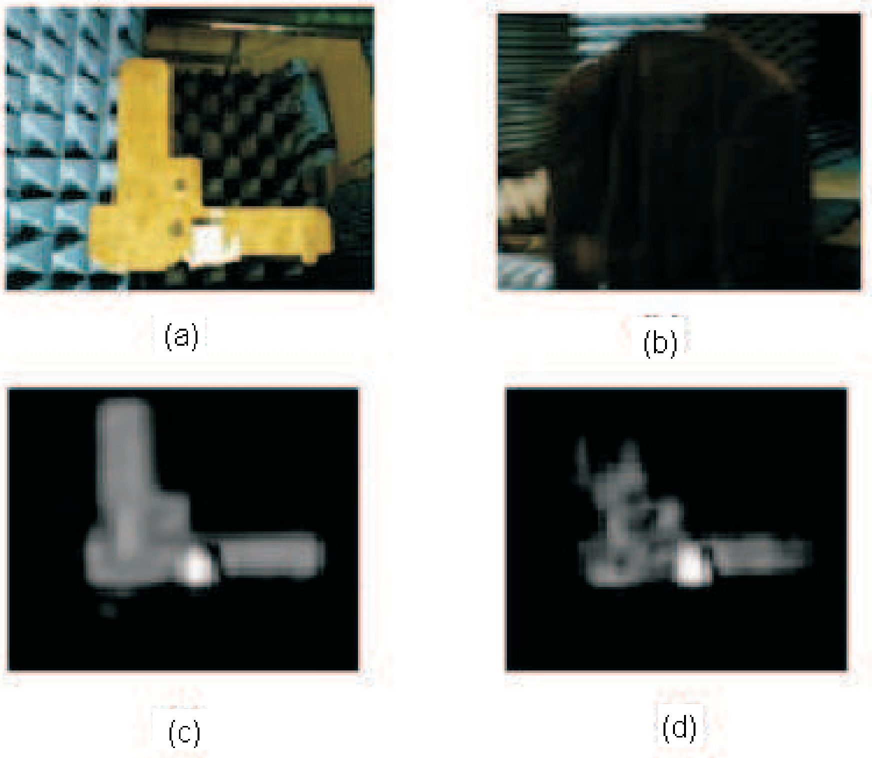

Figure 4.1: (a)The optical image of the MDF gun replica with a small metallic square on top (b) Target is covered with a suit (optical image). (c)(d) The MMW images corresponding to (a) and (b).

4.3.3 Scenario 2

Fig 4.3(a) is the target — a MDF gun replica and Fig 4.3 (b) is its MMW image, background is the chamber walls. In Fig 4.3 (c) the target is covered with two layers of towelling and Fig 4.3(d) is the MMW image. It is observed that there is not much change in terms of image quality, as if the two layers of towelling were transparent. The arm used to support the handgun is as reflective as the MDF handgun replica. From the resulting image quality, it is concluded that the imaging system not only effectively reveals the shape of the metallic subject, but also a dielectric one. This demonstrates that the system can detect concealed targets

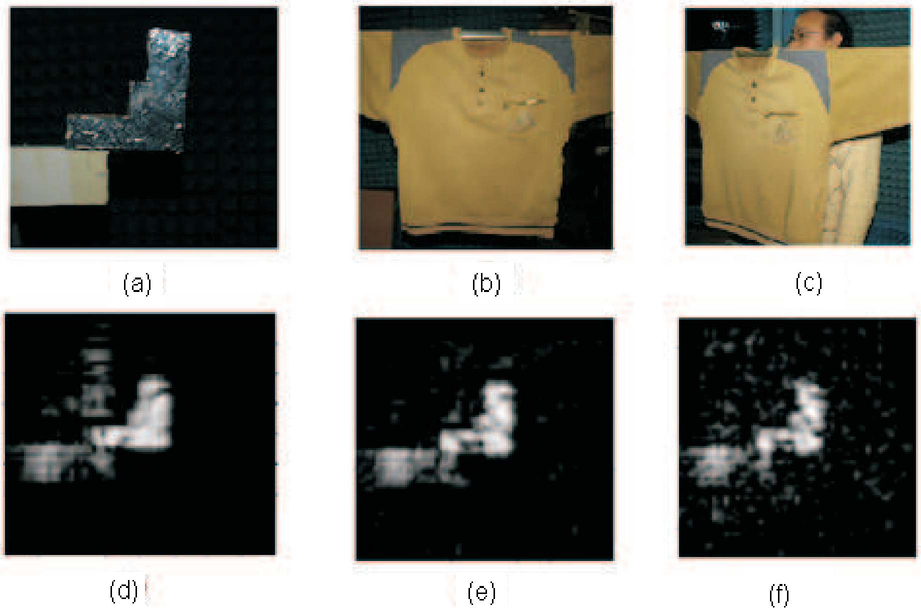

Figure 4.2: (a) The optical image of the gun model wrapped with metallic foil. (b). Target is covered with a woolly. (c) Target is covered with a woolly, human body as the background. (e)(d)(f) Millimetre wave images corresponding to (a)(b)(c).

that are largely non-metallic, for example, a handgun that is largely ceramic.

4.3.4 Scenario 3

As scenario 2, except the MDF handgun replica is wrapped with metallic foil, all other factors remain unchanged (Fig 4.4), then the measurement procedure was repeated. Fig 4.4(b) is the MMW image of the target. In Fig 4.4(c) the target is hidden behind two layers of towelling and Fig 4.4(d) is its MMW image. It is not surprising that the MDF handgun replica image is brighter than that of the arm as the flat metallic foil is more reflective.

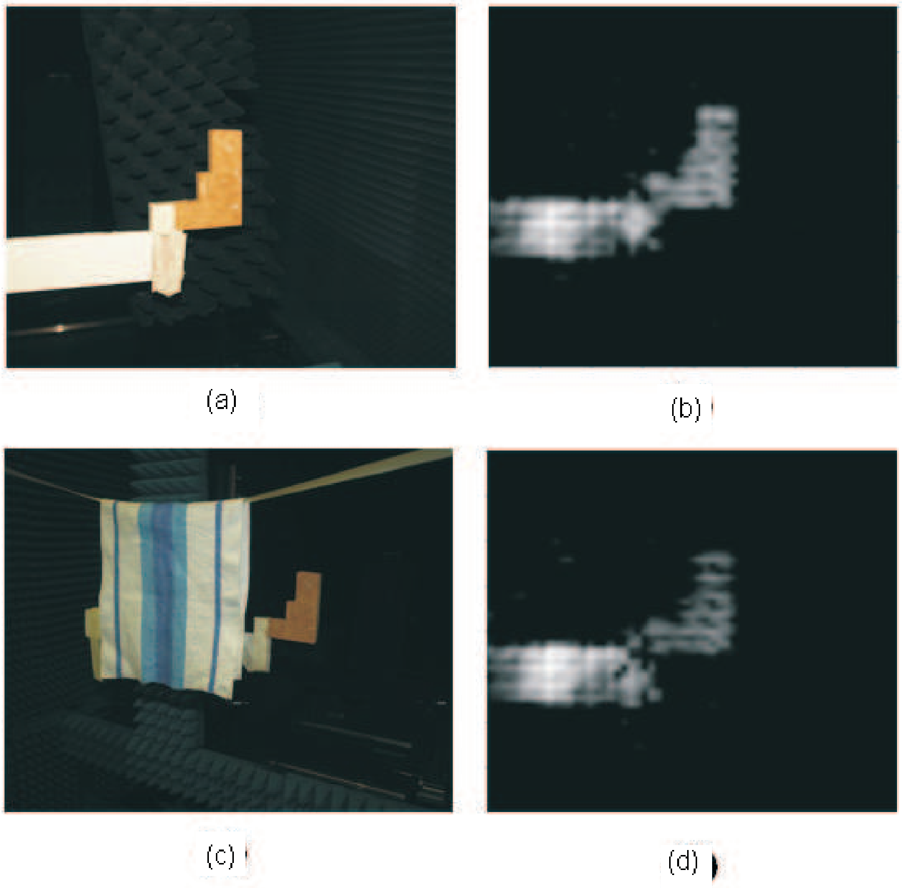

(a) (b)

(c) (d)

Figure 4.3: MMW image of a MDF handgun replica (a) optical image (b) MMW image (c) The MDF handgun replica hidden behind two layers of towelling. (d) MMW image of (c)

4.3.5 Scenario 4

As scenario 3, except the change of covering towelling from 2 to 4 layers and the use of a thick woolly as the covering material, there were no other changes to the setup Fig 4.5(a). Fig 4.5(b) is its MMW image and compared to the one covering with a thick woolly in Fig 4.5(d), it is very noisy. One reason for this is the reduced reflection strength from the target, the other reason might be due to the resonance occurred within the 4 layers towelling, given the fact that the weave period is close to the operating wavelength and the separation of each layer is in the order of a

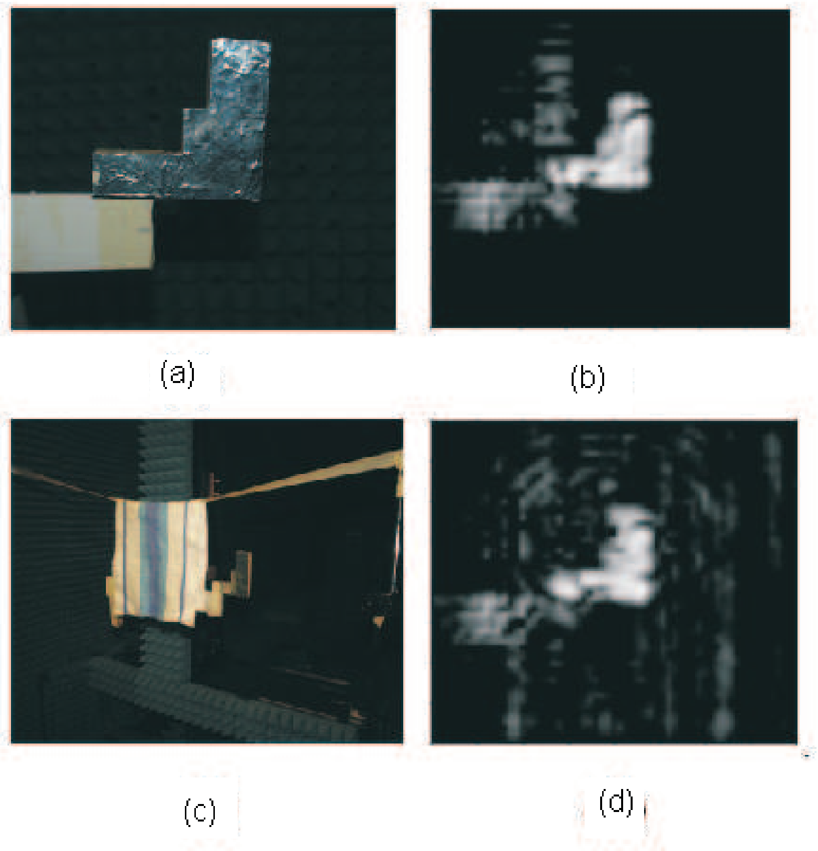

Figure 4.4: MMW image of the metallic foil covered handgun. (a) optical image (b)MMW image (c) target is concealed behind two layers of towelling (d) MMW image of (c)

wavelength.

4.3.6 Scenario 5

In Fig 4.6, concealed weapon detection in a very real scenario was demonstrated. The metallic foil wrapped handgun replica was hidden behind a thick woolly, but different from scenario 1, 2, 3 and 4, a human body is used as the background. In Fig 4.6(a) the target is hidden between the woolly and a clothed human body, Fig 4.6(b) is its MMW image which is noisier than Fig 4.5(d) (without human body background), but most of the target features still can be revealed. This is the

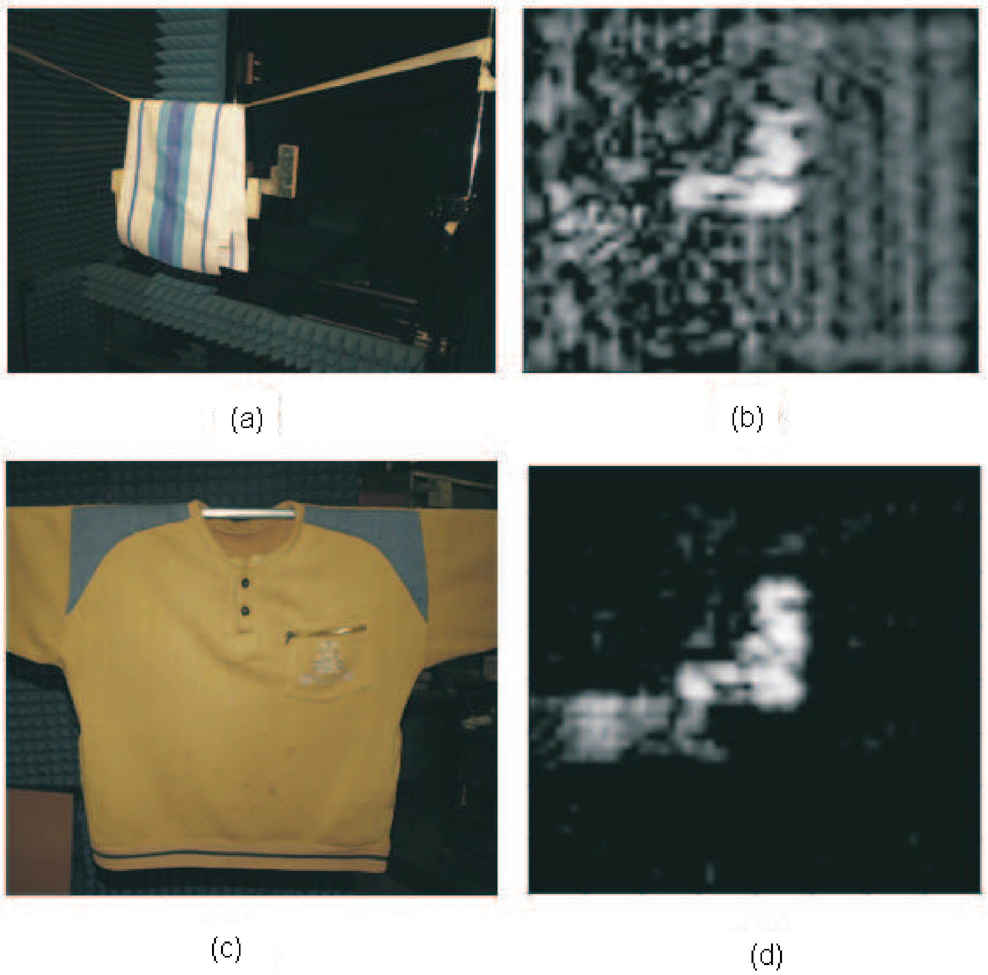

Figure 4.5: Penetration ability of investigation (a) metallic foil wrapped handgun target hidden behind 4 layers of towelling (b) MMW image of (a). (c) handgun target hidden behind a thick woolly. (d) MMW image of (c)

situation where the human is wearing multiple layers of clothing in an attempt to conceal any visible sign of object.

4.3.7 Scenario 6

In Fig 4.7(a), a square of perspex with a dimension of 150mm by 210mm on top of its corner was used as the target. Fig 4.7 (b) is its target MMW image. It is not

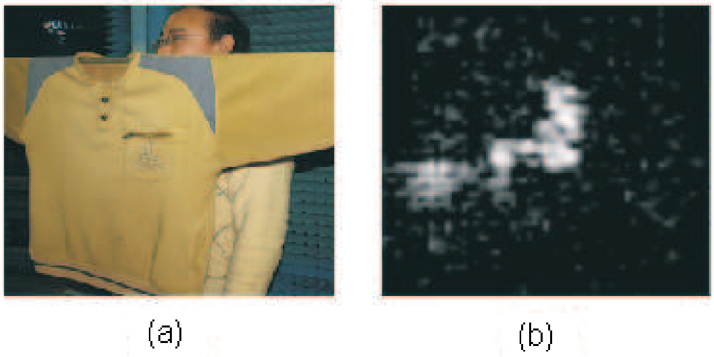

Figure 4.6: Handgun is hidden behind a thick woolly with human body as background. (a) optical image (b) MMW image.

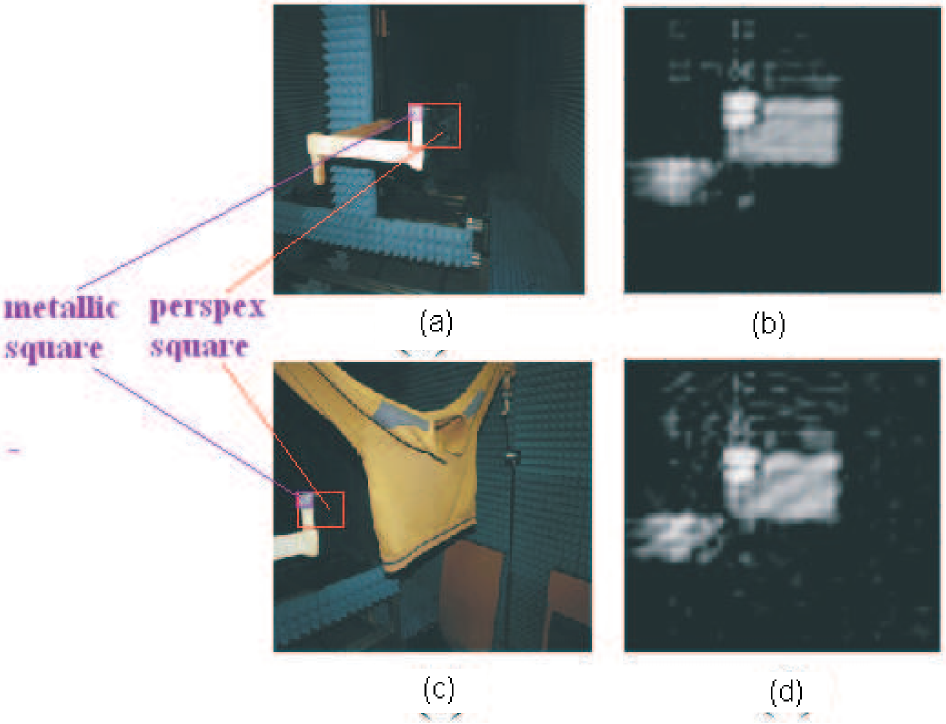

Figure 4.7: A square of perspex with a square of metal on top of its corner (a) optical image (b)MMW image (c) Target is hidden behind the woolly (d)Target MMW image

surprising that metallic square image is brighter than that of the perspex square as the former is more reflective. In Fig 4.7 (c) the target was hidden behind the woolly and Fig 4.7(d) is its target MMW image which is noisier than Fig 4.7(b) due

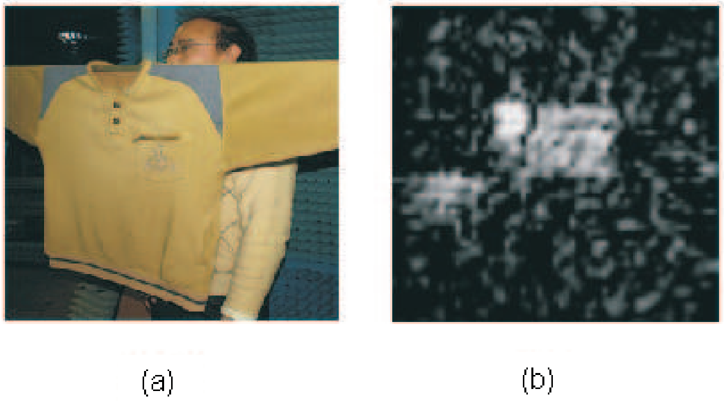

Figure 4.8: A square of perspex with a square of metal on top of its corner and human body as the background (a) optical image (b) MMW image

to scattering caused by the thick woolly, the shape of the target and the material property difference were still largely revealed.

4.3.8 Scenario 7

In Fig 4.8(a) A human body background was added to scenario 6, and Fig 4.8(b) is its MMW image. Even though body skin permittivity (at 94GHz it is 10.9-j5.0 [2])is larger than that of perspex and supposed to give more reflection, but Fig 4.8(b) shows perspex square image is brighter than that of the skin(body), this is because the perspex square is flat and the reflected energy is strong in a limited angle of view, whereas human body scatters the interrogating wave evenly distributed in all directions.

4.3.9 Scenario 8

The scenario in Fig 4.9 was designed to test the system discriminating ability for different materials. The target is a piece of gun shaped foil pasted on a square of

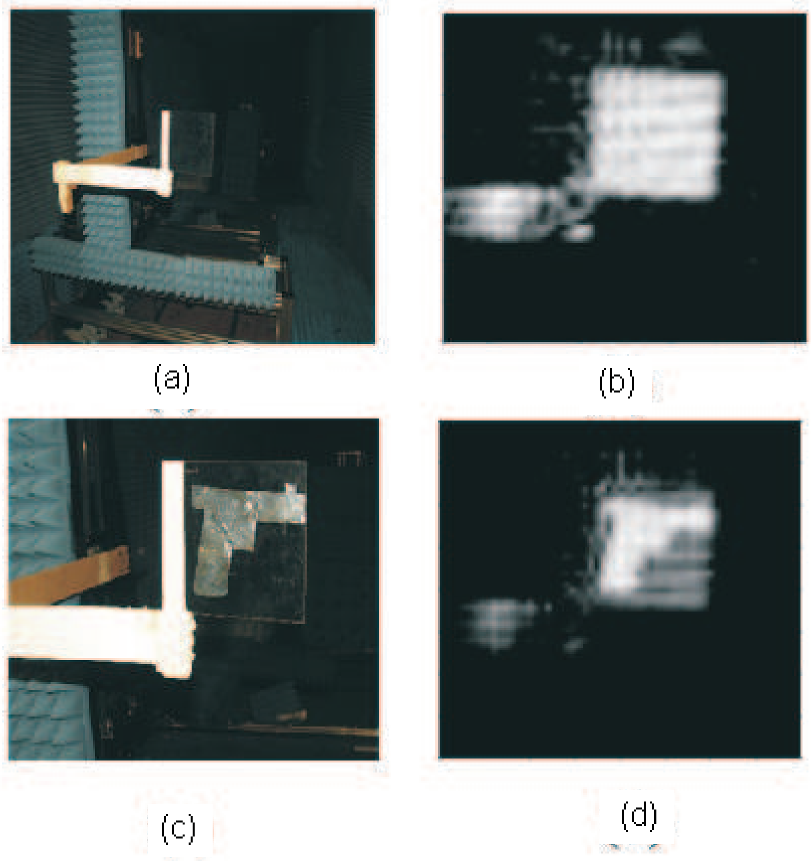

Figure 4.9: (a) the optical image of the perspex square (c) a piece of gun shaped metallic foil pasted on the detection sensor side of the perspex square, chamber walls as the background. (b)(d) the millimetre wave images corresponding to (a)(c)

perspex (thickness 1 mm). Fig 4.9(a) is the optical image of the perspex square and in Fig 4.9 (c) a piece of gun shaped metallic foil was pasted on the detection sensor side of the perspex square, the chamber walls as the background. In Fig 4.10(a) a woolly cover was added and again in Fig 4.10(c) a human body background was added. Fig 4.9(b)(d)and Fig 4.10 (b) (d)are the millimetre wave images corresponding to Fig 4.9(a)(c)and Fig 4.10 (f) (h). It can be seen that gun shaped foil images appeared brighter than that of the perspex square, both the foil gun and perspex square shapes were revealed in all cases.

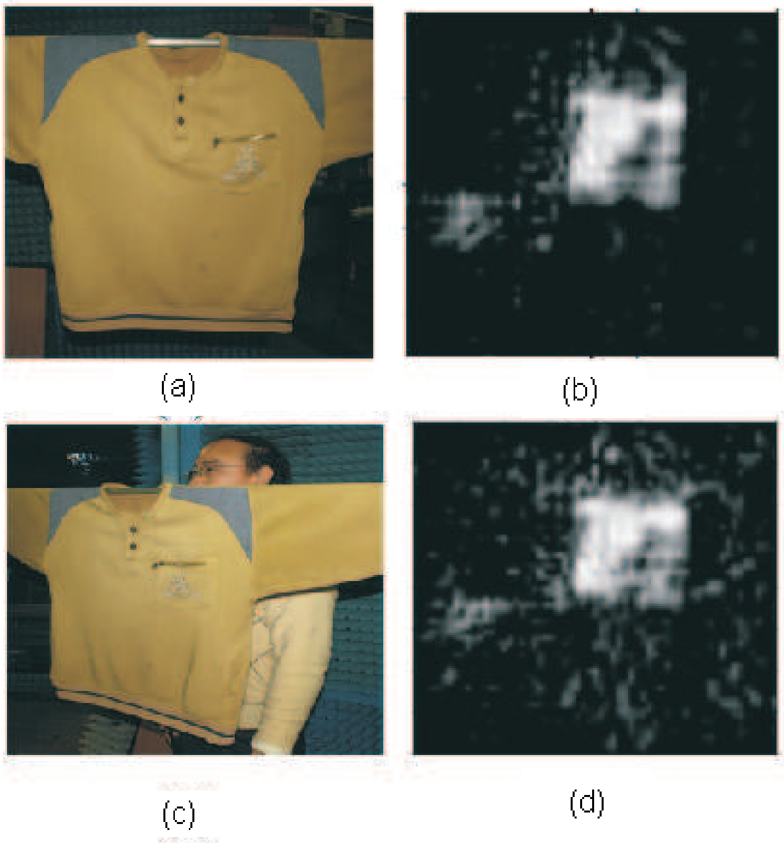

Figure 4.10: (a) a woolly cover was added. (c) a human body background was added. (b)(d) the millimetre wave images corresponding to (a)(b)

4.3.10 Scenario 9

The perspex square image is very sensitive to its orientation as the reflected energy is limited to a very narrow field of view. In Fig 4.11 the target is composed of 4 parts, the liquid (material property is close to that of human skin/tissue) contained in a plastic bubble wrapping, the wooden frame, a metallic foil wrapped wooden gun and a square of perspex in the upper right corner. In both cases of Fig 4.11 (a)(c), only a few degrees change of orientation of perspex square occurred. It can be concluded that target image quality is not only related to target material property, but also very much related to the target orientation, especially for the target with mirror surfaces.

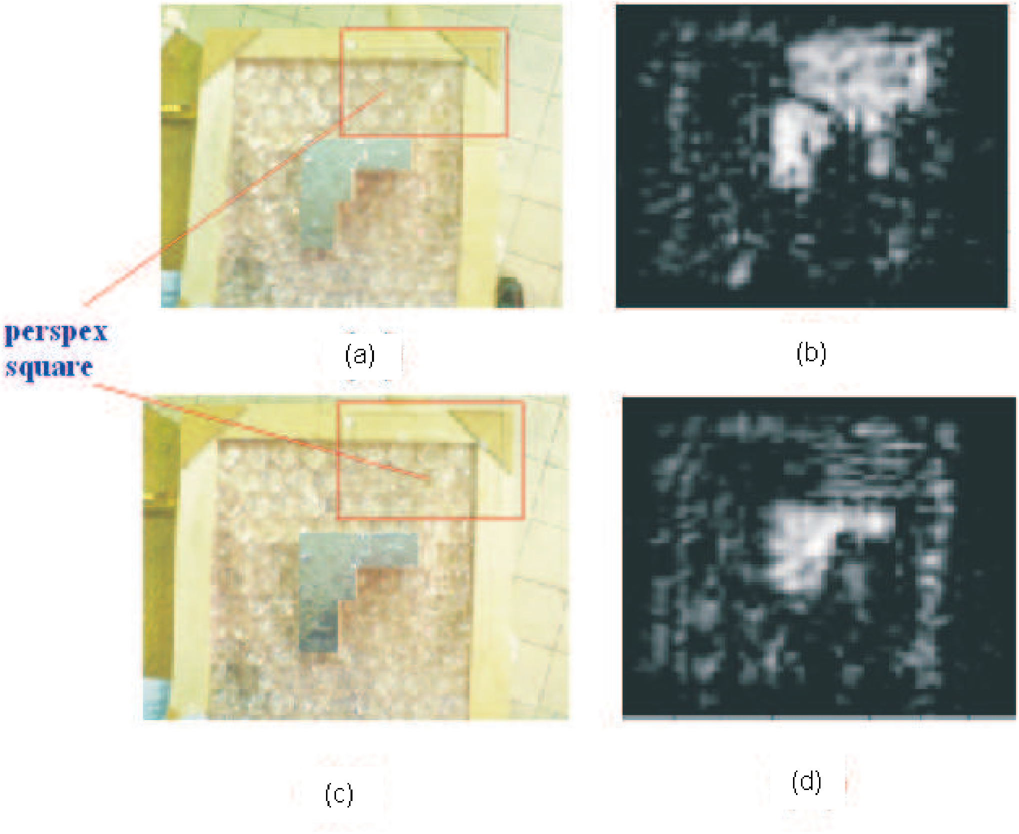

Figure 4.11: (a)(c) a metallic foil wrapped gun with a background whose material property is comparable to human tissue. In all three cases, the flat square perspex orientations are slightly different. (b)(d) MMW images corresponding to (a)(c)

4.3.11 Scenario 10

In Fig 4.12 and Fig 4.13, the penetration ability through various materials at 94 GHz is tested. Fig 4.12 (a) is a CD case (perspex) with a CD (Aluminum) inside, Fig 4.12 (b) is its MMW image, the CD shape was revealed. Fig 4.12 (c) is the optical image of a metallic foil wrapped MDF gun replica and Fig 4.12 (d) is its MMW image. In Fig 4.13 (a) and (c), the metallic foil wrapped handgun replica is covered with 4 layers of towelling and a thick woolen coat respectively, both with a background whose material property is comparable with human body. Fig 4.13(b)

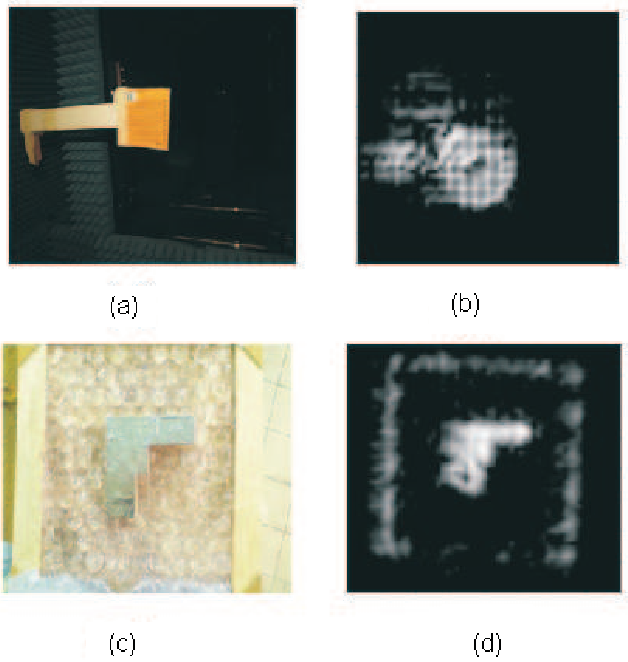

Figure 4.12: ((a) CD case (perspex) with a CD (Aluminum) inside. (b) MMW image of (a), the CD shape is revealed. (c) is the optical image of a metallic foil wrapped gun. (d) MMW image of (c).

and (d) indicate penetration to clothing at 94 GHz is very effective.

4.3.12 Scenario 11

A block of cheese was used as the background in this scenario. In Fig 4.14(a), a 50p coin was put on top of the cheese block, in Fig 4.14(b) a piece a metallic gun shaped foil was put on top of the cheese block and in Fig 4.14(c) target b was covered with towelling. Fig 4.14(d) (e) (f) are corresponding MMW images to Fig 4.14(a) (b) (c). It can be concluded that for metallic targets, cheese background has little effect on the image quality.

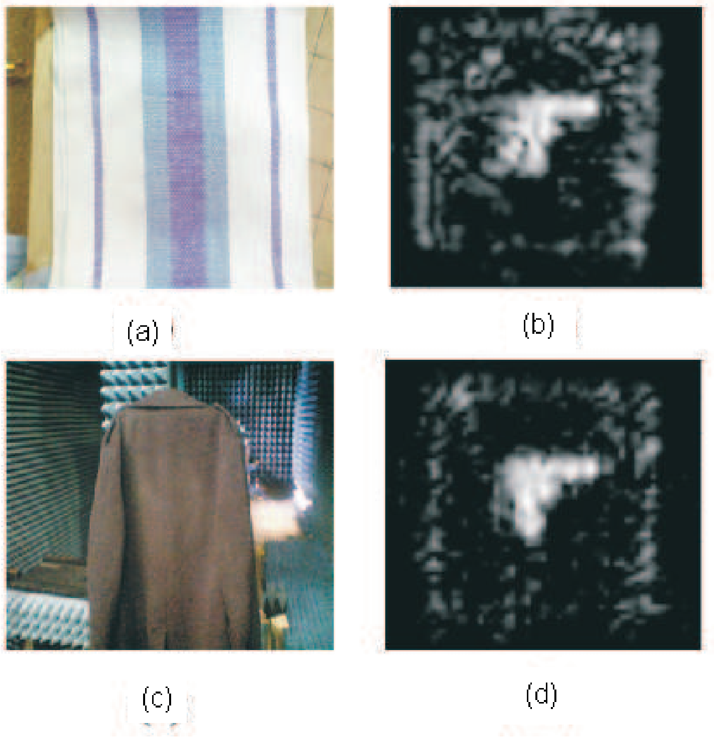

Figure 4.13: (a) and (c), a metallic foil wrapped hand gun is covered with 4 layers of towelling and a thick woolen coat respectively both with a background whose material property is comparable with human body. (b) and (d) corresponding MMW images of (a) and (c).

4.3.13 Summary of qualitative evaluation

Based on the experimental results it is concluded

1. Various types of clothing were used to test the penetration ability at 94GHz, qualitatively speaking, penetration to clothing is generally fine, the transmissions of the common clothes provided also show penetrations are generally high.

2. Discrimination of different materials is possible, as image brightness is related to material property.

3. Since the body has a very high dielectric constants and reflectivity is 0.81

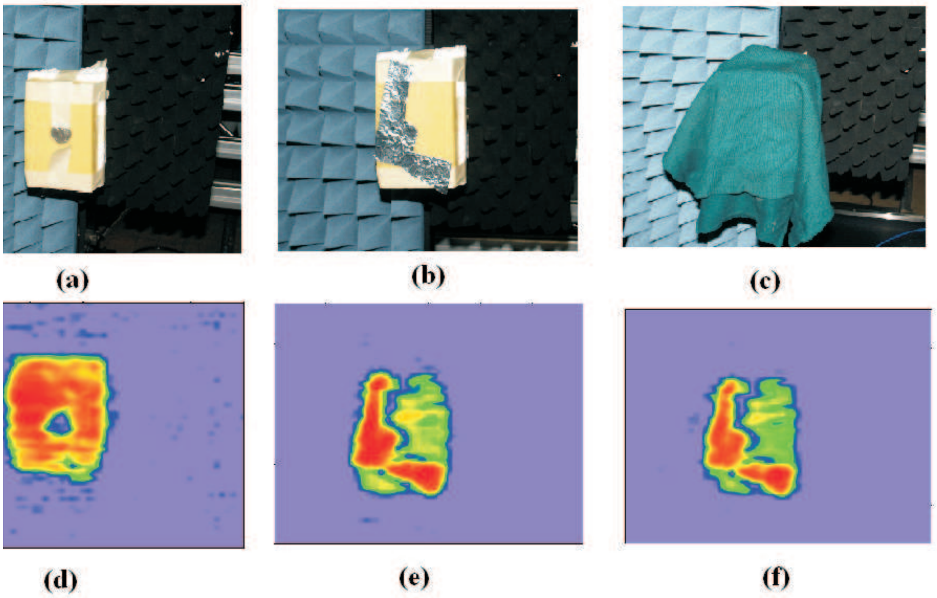

Figure 4.14: (a) a 50p coin on top of the cheese block. (b) a piece a metallic gun shaped foil on top of the cheese block. (c) target b was covered with towelling. (d) (e) (f) are corresponding MMW images to (a) (b) (c)

which is comparable to targets' reflectivity. For non-metallic objects, the contrast maybe low. But for large and flat non-metallic targets with a mirror surface, the energy only exists in the specular reflection which causes the loss of reflected signal to all other directions. The image quality is very much related to the orientation of the target.

4. For the active imaging system used here, the interaction between the interrogation wave and target (including the background and cover) could be very complex due to the resonance within the target.

Table 4-D: Copper slab and leather cover dimension and material properties

target	width (mm)	length (mm)	thickness (mm)
copper	75	173	0.35
leather	80	180	1.0

4.4 Quantitative imaging system performance evaluation: test target image SNR_I, NEΔR, and $\sigma(B_{notarget})$

4.4.1 Target description

In this section, SNR_I, NEΔR with respect to two test targets, i.e. a copper slab and a piece of leather are used to evaluate the prototype imager performance. This is the direct way of evaluation. Two targets dimensions and dielectric constants are listed in TABLE 4-D. Each of the targets is fixed to the arm of the NSI scanner for the measurements.

4.4.2 Test target knife edge SNR_I, NEΔR, and $\sigma(B_{notarget})$

Fig 4.15 (a) (b) (c) (d) (e) are the optical image and MMW images of the copper slab at different transmission power levels. Fig 4.16(a) (b) (c) (d) (e) are the optical image and MMW images of the leather covered copper slab at different transmission power levels. TABLE 4-I and TABLE 4-F are the SNR_Is, NEΔRs, calculated. It can be concluded that the imager can achieve a saturated SNR_I value of 23.3 for a copper slab test target with a NEΔR value of 0.0419. For the leather covered copper slab results, there is very little variation of the SNR_Is,

Table 4-E: Copper slab SNR_I

MMW Image	SNR_I	$NE\Delta$R
Fig 4.15 (b)	23.30	0.0419
Fig 4.15 (c)	20.72	0.0453
Fig 4.15 (d)	3.4	0.1848
Fig 4.15 (e)	-0.0012	0.5025

NE∆Rs, which means the leather is very transparency. Fig 4.17 is the plot of SNR_I vs transmission power of both copper slab only and leather covered copper slab.

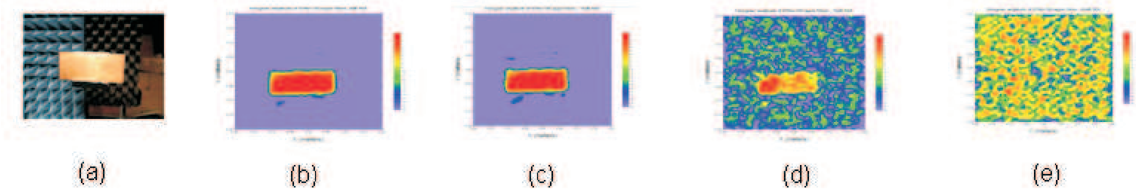

Figure 4.15: (a) Optical image of the copper slab (b) to (c) The MMW images of the copper slab at transmission power (b) 20 mW (c) 4 mW (d) -12 mW (e)-28 mW

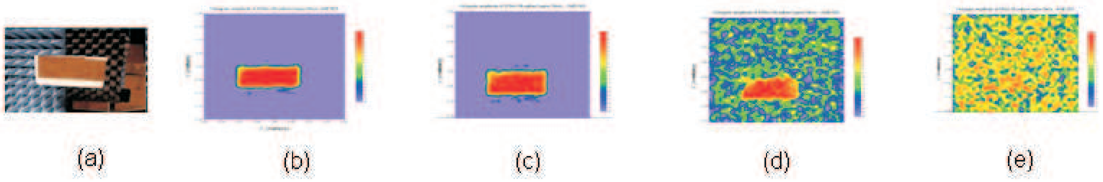

Figure 4.16: (a) Optical image of the leather covered copper slab (b) to (c) The MMW images of the copper slab at transmission power (b) 20 mW (c) 4 mW (d) -12 mW (e)-28 mW

Fig 4.18 is the absorber background of the target space, the tile absorber in the center is used to block the scanner arm to which the target is attached. The standard deviation of the image scene, when there is no target, $\sigma(B_{notarget})$ is a parameter used to describe the uniformity of the reflectivity in the background

Table 4-F: leather covered copper SNR_I

MMW Image	SNR_I	$NE\Delta$R
Fig 4.16 (b)	23.88	0.0409
Fig 4.16 (c)	19.19	0.0485
Fig 4.16 (d)	3.96	0.1674
Fig 4.16 (e)	0.3924	0.4167

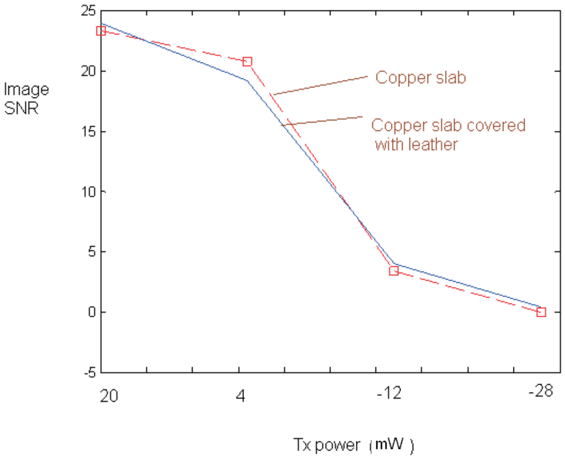

Figure 4.17: SNR_I vs transmit power plot. Target copper slab and leather covered copper slab

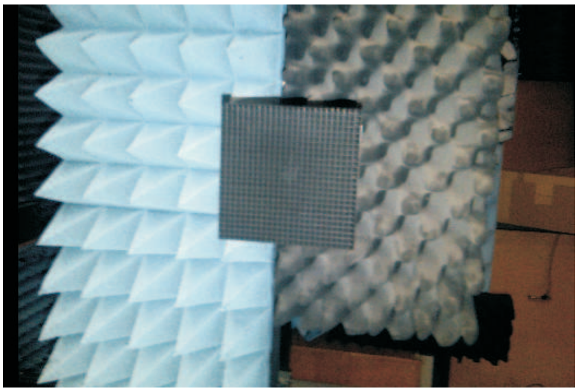

Figure 4.18: The background absorbers (including the tile absorber)

plane. Its values at different transmission power levels are compared in Fig 4.19 with the values from the non-target areas when the copper slab or the perspex slab are in the scene. Its calculation procedure can be found in Appendix B.

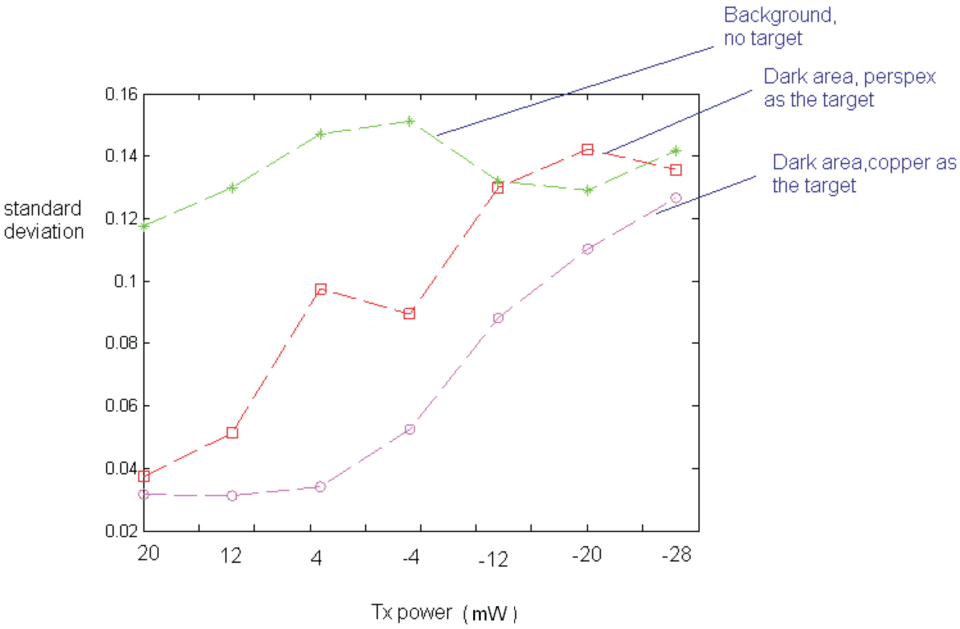

Figure 4.19: standard deviation σ of the scene background and the dark areas of the copper and perspex slabs images

These results show that the background (including the tile absorber) noise standard deviation is higher than the dark areas when the copper and perspex slabs target exist. It maybe caused by the edges of the front tile absorber as the standard deviation of the dark areas (non-target areas) are generally lower than $\sigma(B_{notarget})$ when the absorber edges are blocked by the slabs. The perspex slab has higher standard deviation of brightness in the dark area than the copper slab. This due to the more speckle caused by the dielectric target. Fig 4.19 shows, when the tx power decreases, the standard deviation of dark areas are generally increased.

4.5 Imaging system performance evaluation: resolution

4.5.1 Imager resolution estimation: PSF estimation method

4.5.1.1 OTF, MTF and PTF concepts of an MMW imager

The transfer function is used to characterize electronic systems, and is defined as the Fourier transform of the impulse response. Corresponding to this time related frequency concept, optical transfer function (OTF) is used to characterize the spatial Fourier domain [4]:

$$OTF = \frac{\int\int s(x^{'}+y^{'})exp[-j(\omega_x x^{'}+\omega_y y^{'})]dx^{'}dy^{'}}{\int\int s(x^{'}+y^{'})dx^{'}dy^{'}} = \frac{s(\omega_x,\omega_y)}{s(0,0)} = MTFexp(jPTF) \tag{4.1}$$

where $s(\omega_x,\omega_y)$ is the point Fourier transform of the spread function (PSF) or impulse response $s(x^{'}+y^{'})$. It is normalized to its own maximum which usually occurs at $\omega_x = 0$, $\omega_y = 0$. Equation (4.1) is a complex number which has an amplitude of MTF (modulation transfer function) and a phase of PTF (point transfer function). MTF is a measure of the ability of an imaging component or system to transfer such spatial modulation from input (object plane) to output (image plane). PTF is related to target image distortion.

The resolution of a imager can be evaluated by its aperture PSF. To measure PSF, it is important to determine which size of object can be considered a point object. It is the smallest element recordable in the image space. A point source corresponding to an image plane size less than that of a pixel is a good way to measure system MTF.

LSF (line spread function) is an estimate for an imager PSF, it can be obtained by imaging a bar and then obtaining the edge response ESF, then take the derivative of the transition from white and black, see equation (4.2). For a rectangular bar it is assumed to have a PSF in the form of a Sinc-function.

$$LSF = \frac{d}{dx}ESF = sinc(\frac{k_0 L\theta_{pix}}{2}) \tag{4.2}$$

where θ_{pix} is defined in equation 4.4, and L is the recording aperture dimension, see Fig4.20.

ESF can be estimated by sub-pixel sampled knife-edge brightness. For a rectangular aperture, its the knife edge brightness (amplitude) distribution near the edge that can be represented by the sine integral function in equation (4.3) and equation (4.4) [3]

$$Si(\theta_{pix}(x)) = \frac{1}{\pi}(\int sinc(\frac{k_0 L\theta_{pix}}{2})d\theta_{pix} + \frac{\pi}{2}) \tag{4.3}$$

$$\theta_{pix} = tan^{-1}(\frac{x_{sub}}{z_T - z_a}) \tag{4.4}$$

where Δy is the image pixel size in y direction in the image plane, θ_E is the knife edge angle with reference to y axis, see Fig4.20. When θ_E is small, $x_{sub} \doteq \Delta y \sin\theta_E$, z_T and z_a are target plane and aperture plane respectively.

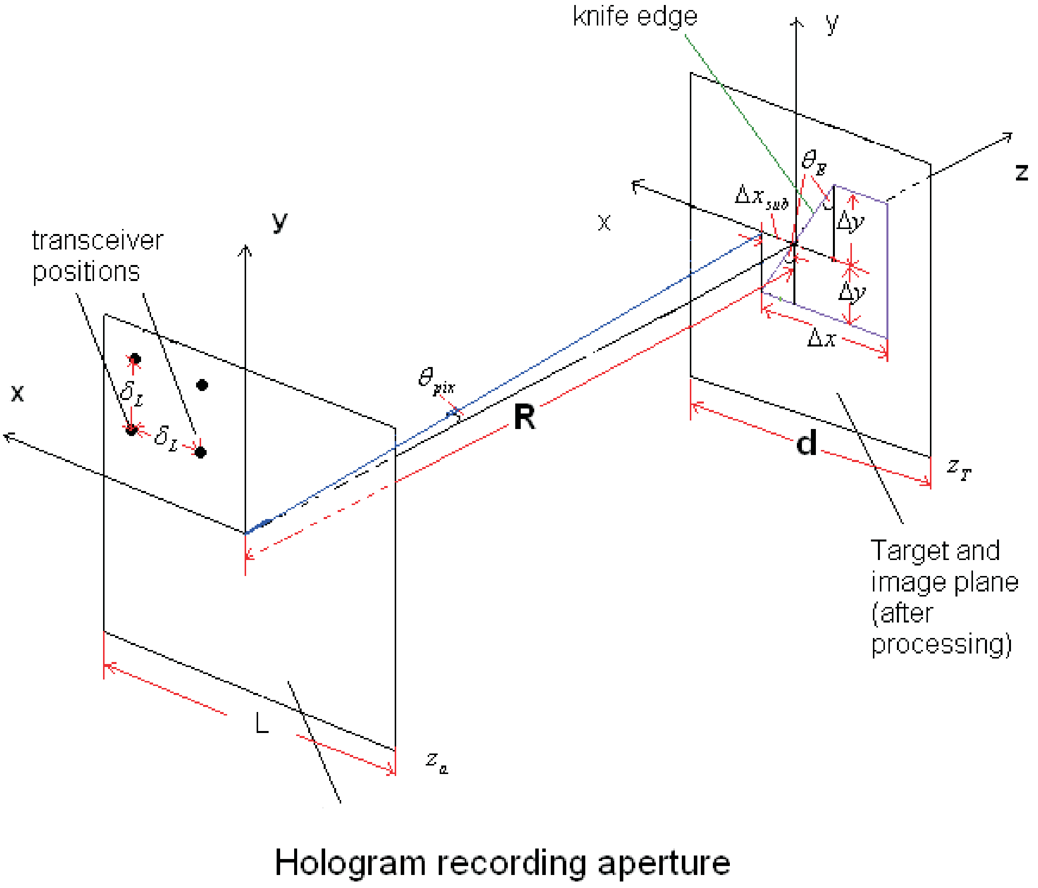

Figure 4.20: The reference coordinates system

4.5.1.2 System set-up

The system set-up has been described in chapter 2. For the settings and configurations, unless otherwise stated, they remain unchanged. In the following measurement, the output power of the transmitter is set at 5 mW, which is the normal operation output power level validated in chapter 3.

The use of NSI measurement system has been described in chapter 2 and the measurement procedure is as follows: Open the ”NI Scanner” Icon on the desktop, click on ”Measurement” icon to fill in the scan parameters, the hologram is sampled

10mm by 10mm by raster scan. Once the scan finishes, click on "hologram" icon then set up the hologram display. Display area is also set as 400mm by 400 mm. Number of points is set as 400×400, so that image pixel size is 1mm by 1mm. The edge angle θ_E is 2 degrees, thus Δx_{sub}=Δysinθ_E=1mm×sin2°=0.0349mm=$\frac{1}{30}\Delta$x, which means it requires 30 pixels ESF samplings in y direction in the image plane to be projected in x direction, corresponding to just one Δx (Fig4.20).

4.5.1.3 Knife edge horizontal (used for vertical LSF estimation)

The knife edge used for the measurement is shown in Fig 4.21 and its dimension is illustrated in Fig 4.22.

Figure 4.21: The knife edge photo

4.5.1.4 Data processing

The MMW image of the knife edge is shown in Fig 4.23. the upside edge has tilt angle of 2 degrees. The edge is used to sample the edge response in x direction, of which every 30 samplings, once projected to y direction, are equivalent to one pixel in y direction. Fig 4.24 shows the response near the edge area. Row 206 is used for the PSF estimation. In fact, rows near row 206 will produce very similar

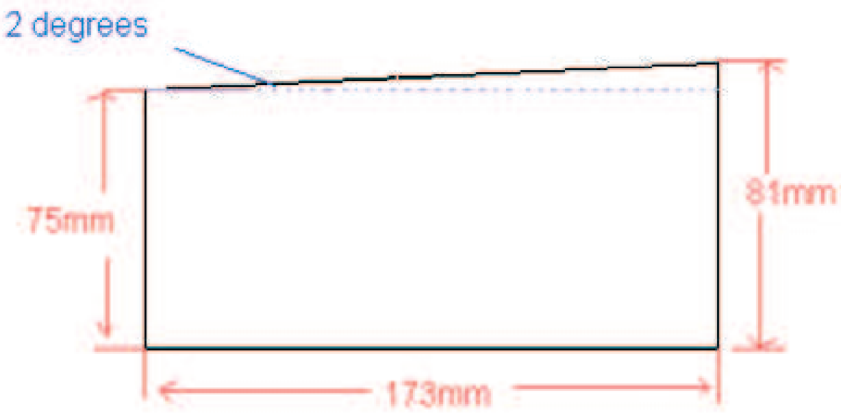

Figure 4.22: The knife edge dimension

results. The left hand side data of row 206 is not useful due to the distorted edge. The right hand side portion of row 206, from the minima to the maxima, is used for PSF estimation. Ideally, more useful data would be available for use if the knife edge were longer. The chunk of data is min-max normalized and using the min-max normalized sine integral function equation (4.3) for the curve fitting (see Appendix C for details). Again, note should be taken here, it is a two-way recording system so equation 4.4 becomes

$$\theta_{pix} = tan^{-1}(\frac{x_{sub}}{2(z_T - z_a)}) \tag{4.5}$$

which differs from the single horn Gaussian beam illumination in [3]. The best fit throws out of the answer for L equals to 335 mm (close to the actual value of 400mm). Fig 4.25 shows the best fit sine integral function and the sub-pixel sampled edge response in y direction. Once the recording aperture L is known, equation (4.2) is used to plot the estimated PSF and it is shown in Fig 4.26 along with the theoretical value. From the half power beam width, the resolution in y direction can be estimated and it is 3.0mm for the theoretical prediction and 3.9mm from the estimated PSF respectively.

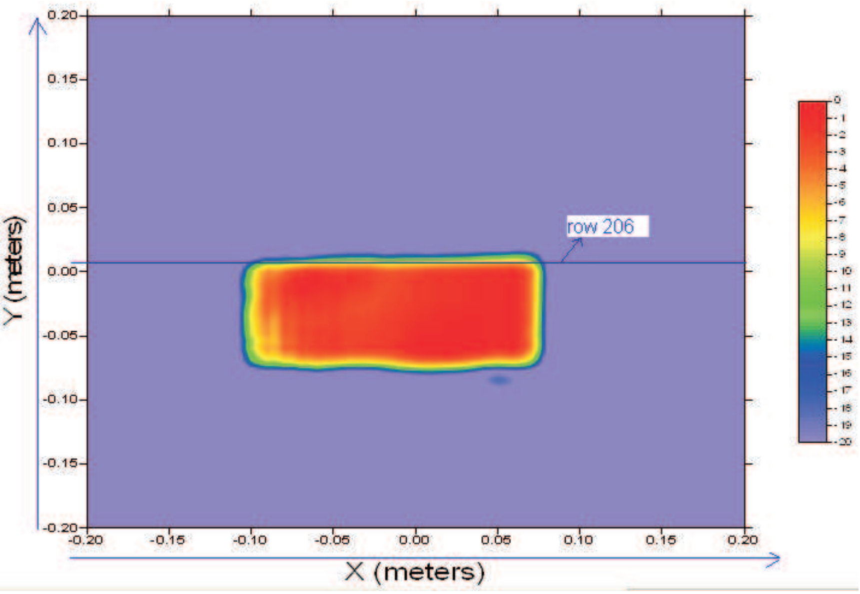

Figure 4.23: MMW image of the knife edge

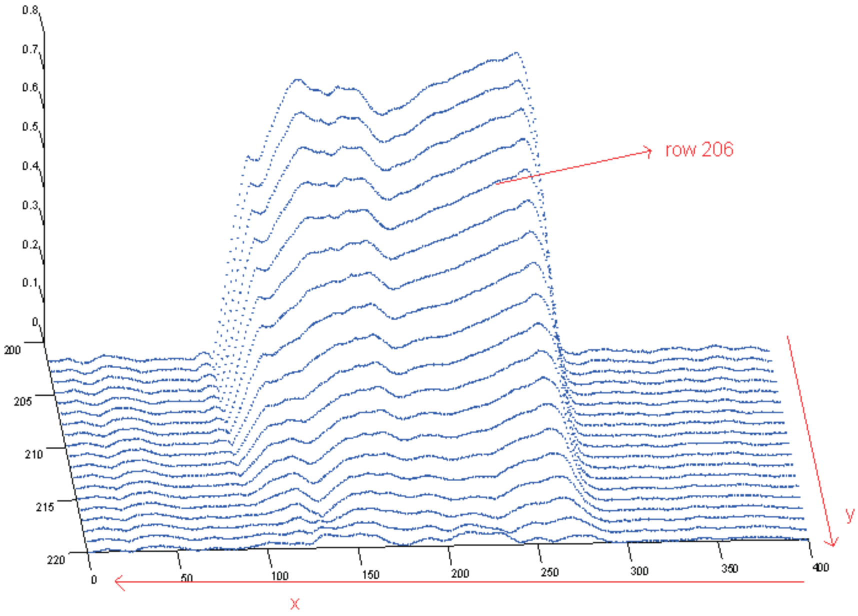

Figure 4.24: Edge response near the edge area, row 206

4.5.1.5 Knife edge vertical (used for horizontal LSF estimation)

The similar procedure is applied to the knife edge vertical sampling case and it results in the MMW image in Fig 4.27, the best sine integral curve fit plot in Fig

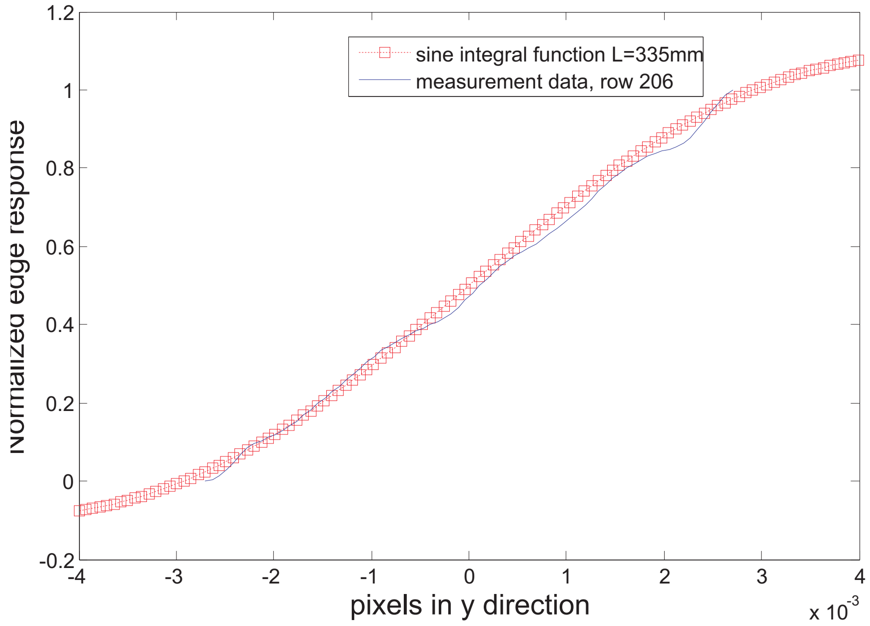

Figure 4.25: Curve fitting using sine integral function for sub-pixel sampled edge response in y direction

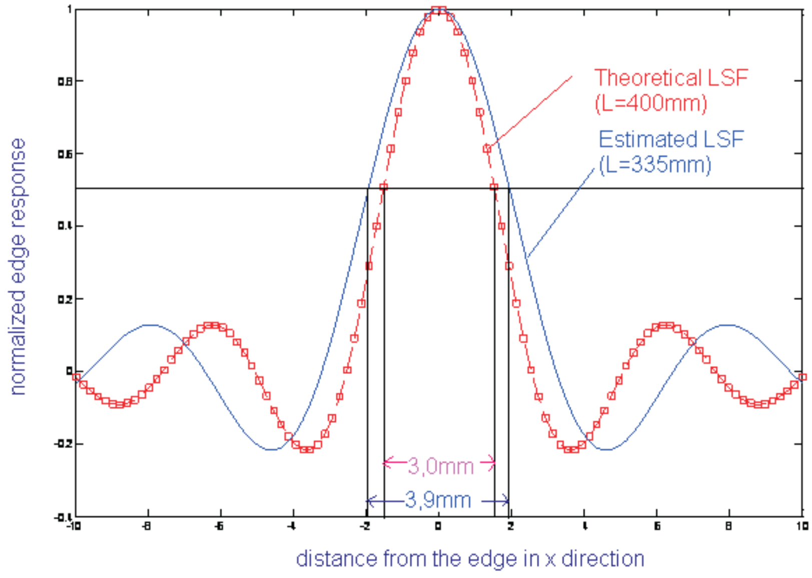

Figure 4.26: The estimated LSF in y direction

4.28 and PSF plots both for theoretical prediction and measurement estimated in Fig 4.29. The estimated resolution in x direction is 3.1 mm which is very close to the theoretical result 3.0mm.

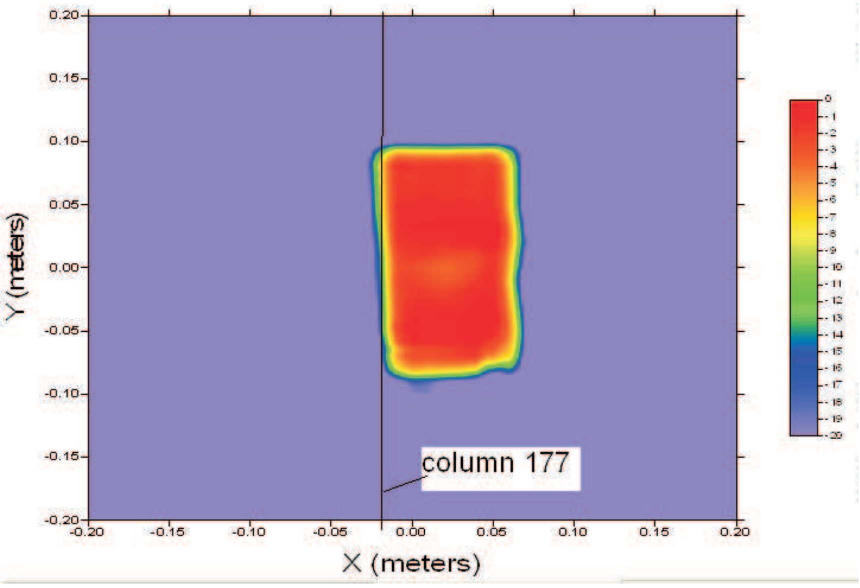

Figure 4.27: MMW image of the knife edge

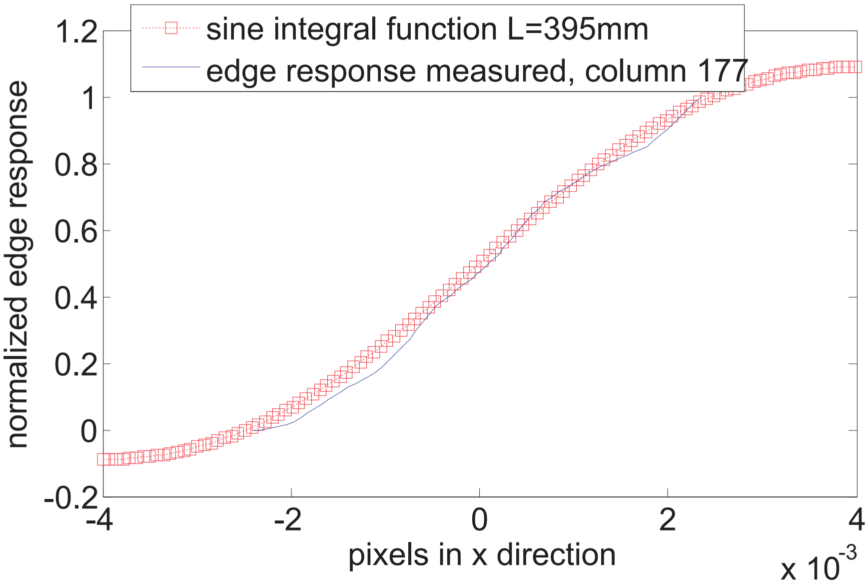

Figure 4.28: Curve fitting using sine integral function for sub-pixel sampled edge response in x direction

4.5.1.6 Discussions

The estimated vertical direction resolution is 3.9mm and the horizontal direction resolution is 3.1mm. Obviously the horizontal result is closer to the theoretical

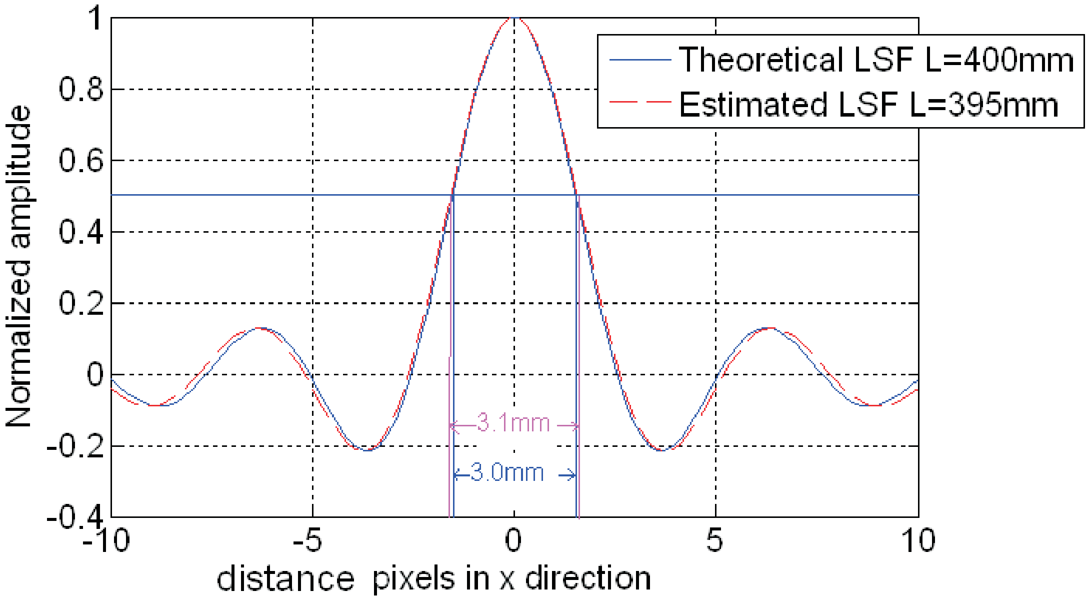

Figure 4.29: The estimated LSF in x direction

result 3.0mm. This is due to the polarization chosen in this prototype imager. The vertial polarization transmission can induce the current effectively when the knife edge is vertically placed.

4.5.2 Imager resolution estimation: experimental method

If the lateral dimension of the synthetic aperture L is fixed at 400mm, then the resolution of the imaging array can achieve is 4mm according to equation (2.1) for the given set-up which d is 1000mm at 94 GHz. Caution must be taken that in an actual system the image quality is related to several factors such as the target material property, target background, target tipping angle, dynamic range of the receiving system, etc. Also note should be taken that equation (2.1) is deduced under the assumption that energy outside the antenna HPBW rim is zero, in fact the energy is still very strong outside the 3dB beam boundary, which means

Table 4-G: experimental settings corresponding to image Figure 4.4 (a) to (d)

	target dimension dimension (mm squared)	Array element spacing (mm)	Sampling density λ(s) /cycle
a	40 by 40	10.0	3.13
b	20 by 20	10.0	3.13
c	10 by 10	10.0	3.13
d	5 by 5	10.0	3.13

reflections from non-object space are also collected with a fair amount of power.

To investigate the system resolution experimentally, a few small targets were made to determine the smallest one that the imaging system could differentiate. The dimensions of a few flat metal foil squares and experimental settings are listed in TABLE 4-G. They were pasted on a piece of flat foam, using the absorber as the background.

Fig 4.30(e) to (h) are the corresponding images to targets in Fig 4.30(a) to (d) respectively. The target still can be seen when it is as small as 10mm by 10mm. When the target is small, the reflected energy is very low, which requires a wider dynamic range of the receiving system and low noise background. The gray scale ranges are different in Fig 4.30(e) to (h). They were normalized respectively to their own maximum rather than to a fixed value. Target in Fig 4.30(d) cannot be seen as the reflected energy is out of the system dynamic range and submerges under the noise floor.

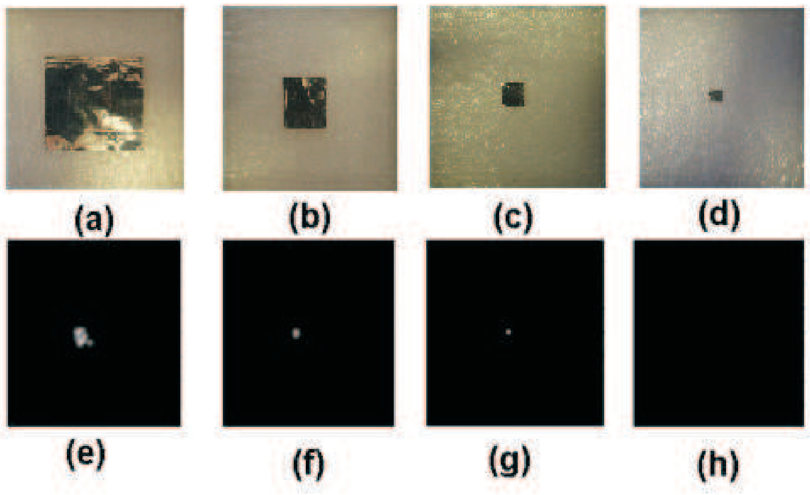

Figure 4.30: Flat metal foil squares, photographs (a) 40mm by 40 mm (b) 20mm by 20 mm (c) 10mm by 10mm (d) 5mm by 5mm. MMW images (e)(f)(g)(h) corresponding to (a) (b) (c) (d). Note: the MMW imaging area is 400mm by 400mm which is different from that of the photographs.

4.5.3 Discussions

The PSF estimated resolution is 3.9mm and 3.1mm in vertical and horizontal direction respectively. The resolution achieved by direct measurement method is between 5mm and 10mm. Even though the VNA receiver used in the imager has a dynamic range of 60 dB, due to the noisy background ($\sigma(B_{notarget})$), the 5mm by 5mm foil cannot be seen. The imager performance might be clutter limited rather than system noise limited in this particular setup. The author would suggest using the smallest metallic square to represent the background scene noise level. The main error source is from the wobbling target as the scanner moves.

4.6 Conclusions

The performance of the 94GHz MMW holographic prototype imager are evaluated qualitatively and quantitatively. For the qualitative evaluation, a range of scenarios are simulated and it is concluded that penetration to common clothes are generally fine. Transmissions of common clothes are generally high. Material discrimination is possible. Target reflectivity contrast against body background maybe low. Image quality is related to the orientation of the target. Resonance within the target could occur. TABLE 4-H summarizes the conclusions.

For the quantitative evaluation, SNR_I, NEΔR with respect to the test target i.e. a knife edge are used. For the imager resolution, two methods are used. The first one is based on PSF estimation, and it is estimated that resolutions are 3.9mm and 3.1mm in vertical and horizontal direction respectively. The second method is based on the direct measurement. The results obtained by the direct measurement method is finer than 10mm. Even though the VNA receiver used in the imager has a dynamic range of 60 dB, due to the noisy background ($\sigma(B_{notarget})$), the 5mm by 5mm foil cannot be seen. The author would suggest use the smallest metallic square visible to represent the background scene noise level. Two parameters can be used to describe the background performance, i.e. $\sigma(B_{notarget})$ and the smallest detectable metallic foil square. The results are tabulated in TABLE 4-I.

The non-metallic target such as perspex has a higher standard deviation of brightness in the dark area than the metallic target. This due to the more speckles caused by the dielectric target. When the tx power decreases, the standard deviation of dark areas are generally increased, which means target background are

Table 4-H: Qualitative performance evaluation of the 94GHz MMW holographic prototype imager

	conclusions
a	Penetration to common clothes is generally fine. Transmissions of common clothes are generally high.
b	Material discrimination is possible
c	Target reflectivity contrast against body background maybe low. Image quality is related to the orientation of the target.
d	Resonance within the target could occur. Under certain conditions, targets maybe invisible

Table 4-I: Quantitative performance evaluation of the 94GHz MMW holographic prototype imager

	quantity
Knife edge SNR_I	23.30
Knife edge NEΔR	0.0419
$\sigma(B_{notarget})$	0.118
the smallest metallic foil that can be seen	less than 10mm×10mm metallic foil
Resolution	By PSF estimate: vertical 3.9mm, horizontal 3.1mm By direct measurement: better than 10mm

generally noisier at low transmit powers than high transmit powers.

References

[1] Appleby, R.; Wallace, H. B.; *The Microwave properties of tissue and other lossy dielectrics* Antennas and Propagation, IEEE Transactions on. Volume: 55, Issue: 11, Part: 1. Digital Object Identifier: 10.1109/TAP.2007.908543. Publication Year: 2007. Page(s): 2944 - 2956.

[2] Alabaster, Clive M.; *The Microwave properties of tissue and other lossy dielectrics*

PhD thesis, Cranfield University, 2002

[3] Tamminen, A.; Ala-Laurinaho, J.; Risnen, A. V.; *Indirect holographic imaging: evaluation of image quality at 310 GHz (Proceedings Paper)* Proceedings Vol. 7670. Passive Millimeter-Wave Imaging Technology XIII, David A. Wikner; Arttu R. Luukanen, Editors, 76700A Date: 27 April 2010.

[4] Kopeika, Norman S.; *A system engineering approach to imaging* SPIE optical engineering press. ISBN 0-8194-2377-7.

[5] Slater, Dan; *Near-Field Antenna Measurements* Artech House, Inc. 1991. Page: 121.

Chapter 5

Investigation of Low Profile New Devices and Techniques for Image Enhancement

5.1 Introduction

In chapters 3 and 4, the investigations were focused on the system parameters and performance evaluation of the 94 GHz MMW holographic prototype imager. The imaging array concept have been raised and its parameters such as elements spacing and array dimension have been investigated. However, manufacturing of such an array is still expensive, so, in this chapter, low profile components and cost reduction techniques will be concentrated.

The main contribution of this chapter is the use of the medium gain woodpile Electromagnetic Bandgap (EBG) antenna for millimeter wave imaging at 95 GHz.

The main advantage of using such an antenna lies in the fact that a shared antenna aperture by the antenna array elements makes it attractive for array forming, as the aperture size limitation is usually a major issue. Also, the woodpile EBG antenna has other advantages over conventional millimeter wave antennas such as low profile, low cost. Its feasibility study and antenna system evaluation has been undertaken via simulation and measurements in the author's group. This is the first application found for such an antenna. The second investigation made in this chapter is the use of the sparse array technique to replace the full array in order to reduce the number of elements. Different sparse array morphologies are tried, and this is a further effort to reduce the number of array elements in addition to the investigation of the maximum possible element spacing made in chapter 3. Since single frequency operation is prone to speckle effect, the third investigation is about an image enhancement technique using multiple frequency operation aiming at tackling this issue. Again, the parameters obtained in this chapter form the bases for the final system design in chapter 8.

5.2 Woodpile EBG Structure For Millimeter Wave Imaging Enhancement

Conical and pyramid horns are often used for conventional millimeter wave antenna systems, one disadvantage of using this type of antennas is that they are bulky and difficult to be integrated with other circuitry when applied to the imaging system. In this section, a free-formed woodpile EBG structure for use in the design of antennas for millimeter wave imaging will be investigated. Compared with the conventional antenna array technology, the woodpile EBG antennas are low profile and easy to fabricate. In [1], it has been demonstrated that the woodpile EBG antenna can achieve a gain of 7 dB with respect to a reference waveguide antenna and HPBW 10 degrees in E-plane and 14 degrees in H-plane, which has comparable performance to those of the horns used in the MMW imaging systems in [2, 3].

In the following sections, a brief review of the design of woodpile EBGs is given first, then the advantage and effectiveness of using woodpile EBG antenna is verified by experiment. An improvement of image quality is observed when the receiving antenna gain increases.

5.3 System set-up and target description

The system set-up used in this chapter remain the same as that has been established in chapter 2 unless otherwise stated. The target used in this chapter is the MDF gun replica that has been described in chapter 3.

5.3.1 Woodpile EBG lens and waveguide structure

5.3.1.1 Requiremenst for the array element in the millimeter wave imaging system

In the proposed millimeter wave imaging system, the receiving antenna can be regarded as a high spatial frequency filter, which only collects the reflected waves at low spatial frequencies from the object space. The deployment of high gain receiving antennas in the imaging system can improve the quality of data acquisition. A directional element pattern would suppress side lobes and increase the S/N level of the receiver.

In [2], a pair of pyramid horns were used as respective transmitting and receiving antennas. However, there are constraints in applying the horn antennas in the design of millimeter wave imaging arrays. Firstly, the element spacing tends to be large due to the excessive aperture dimension of pyramid horns, therefore, it may lead to the violation of sampling criteria which is 5 wavelengths as validated in chapter 3. Secondly, the millimeter wave imaging array based on highly directive metallic horns is bulky due to the length of horn needed to create the radiating aperture and so it is less cost-effective. Planar antennas with the advantages of low profile, small size, light weight, easy fabrication and low manufacturing cost are urgently needed.

5.3.1.2 Description of the woodpile structure EBG Antenna

A directive millimeter wave antenna based on a woodpile electromagnetic band gap (EBG) material at W-band has been developed by Dr Y. Lee at the Antennas and Electromagnetics Group, Queen Mary University of London. The Finite Difference Time Domain (FDTD) method has been applied to compute the dispersion diagram and the band gap frequency of the woodpile EBG [4]. The woodpile is made from high purity ceramics; the filament diameter and spacing at 95GHz are found to be 0.41mm and 1.7mm respectively with a permittivity ε_r= 9.6.

The woodpile structure possesses face-centered-tetragonal symmetries and provides a full three dimensional band gap. Such a periodic structure can be fabricated for microwave applications using columns of individually machined dielectric materials but this is a complex and expensive process. The designed woodpile structure has been fabricated using a novel extrusion free-forming technique. The fabrication facility developed in the material department, Queen Mary University of London (QMUL) is currently capable of making ceramic filaments as thin as 80 μm with 20 μm spacing. High purity alumina powder was used as a dielectric material and mixed with a solvent and binder to prepare pastes. The ceramic pastes were extruded from a metal tube driven by a micro-extruder positioned over a three axis high performance linear motor table capable of high acceleration and speed. After drying, the woodpile samples were sintered, the design taking account of the approximate 20% shrinkage that occurs after sintering.

The proposed antenna consists of a metallic ground plane and a partially reflecting/transmitting layer (superstrate) with area separated from the ground plane normally with a distance approximately a half wavelength at the operating frequency. The overall antenna geometry is shown in Fig 5.1. This type of antenna is often referred to as *Fabry-Perot cavity antennas* or EBG resonator antennas because they utilize the resonance of the cavity formed by the ground plane and the superstrate to obtain a directive radiation pattern. When the cavity resonates, the field inside the cavity spreads out over the entire cavity area achieving a uniform distribution of the aperture field on the superstrate which is considerably larger than the feeding waveguide aperture. Fig 5.2 shows the computed dispersion diagram of the woodpile structure with w/a = 0.25, where w is the width of the dielectric rod, and a is the period of the square lattice. The dielectric constant of the rod is 9.6. As seen from the figure, it is clearly observed that a complete bandgap exists between the normalized frequencies of 0.44 and 0.5. The actual bandgap frequencies for a unit-cell with a = 1.6mm are 82.5 GHz and 93.75 GHz,

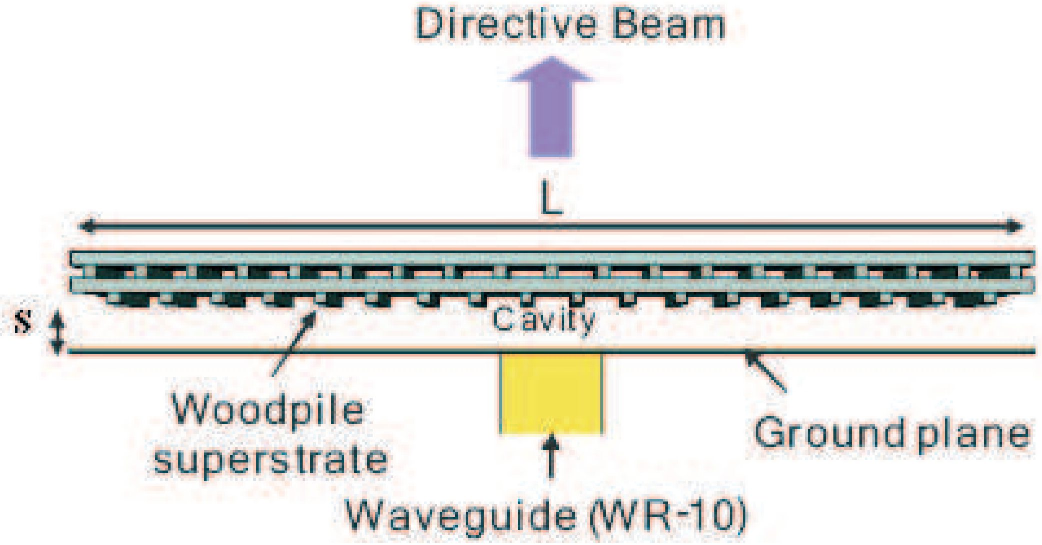

Figure 5.1: Geometry of woodpile superstrate antenna [5]

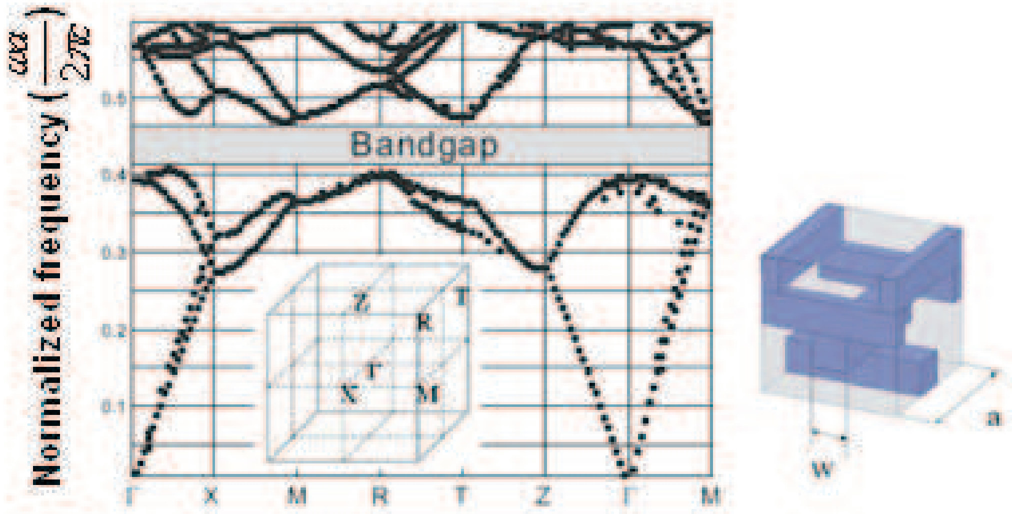

Figure 5.2: Unit-cell of woodpile structure and Brillouin zone [5]

respectively [5].

The antenna pattern of the composite antenna has been measured in an anechoic chamber and the measured antenna patterns are shown in Fig 5.3 and Fig 5.4 [6]. A clear improvement of the antenna directivity is observed both in E and H-plane

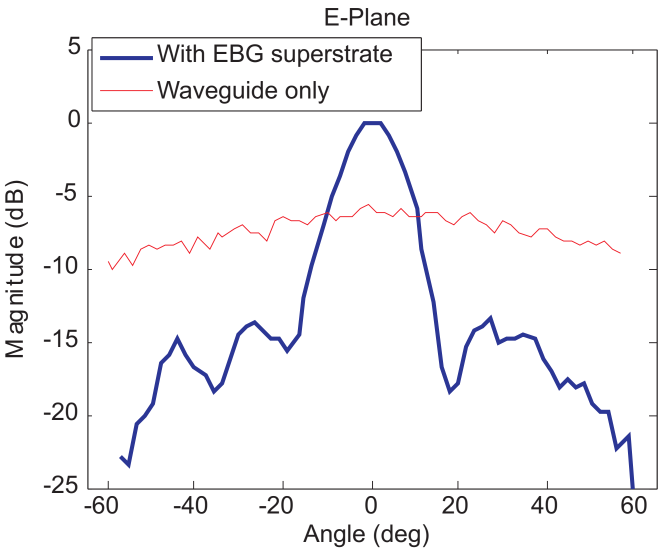

Figure 5.3: Measured normalized directivity pattern of woodpile superstrate antenna, E-plane [5]

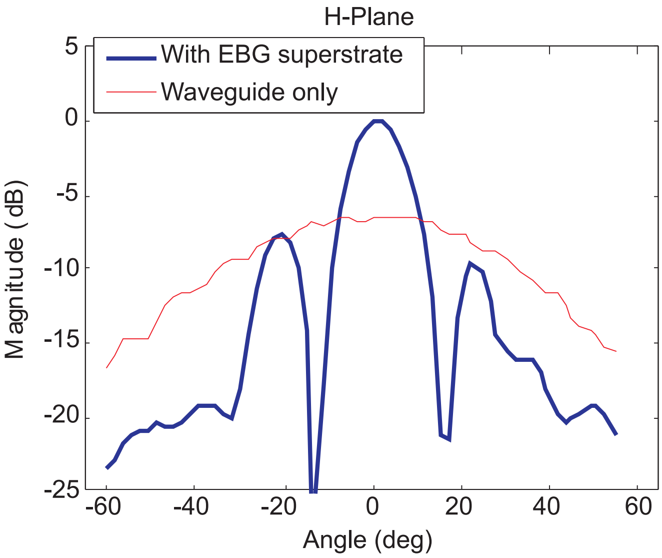

Figure 5.4: Measured normalized directivity pattern of woodpile superstrate antenna, H-plane [5]

patterns. The half-power beamwidths (HPBW) of the prototype antenna are 14 and 10 degrees for E-plane and H-plane, respectively, and the measured gain of the antenna is 13 dBi. The 3dB gain bandwidth of the antenna is approximately 1 GHz. In the following section, this structure will be compared to the corrugated horn, and Fig 5.5 shows the measured corrugated horn pattern. The parameters

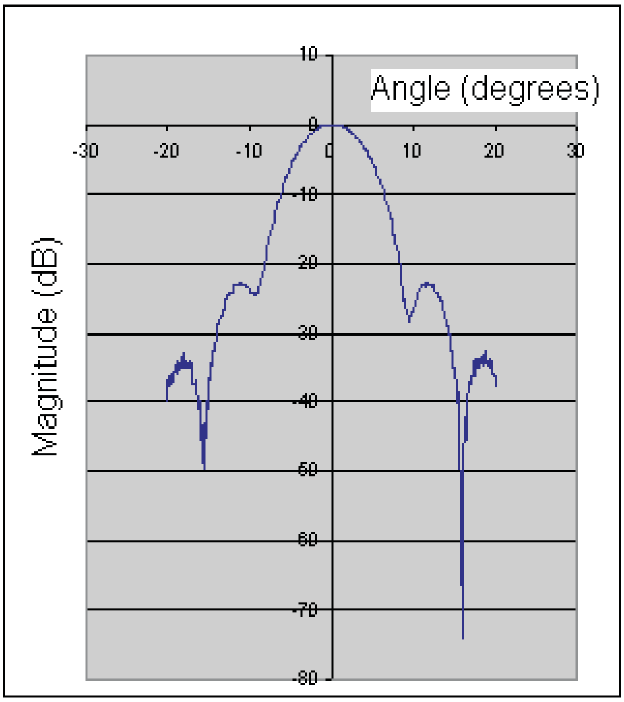

Figure 5.5: Measured normalized directivity pattern of the corrugated horn antenna, E plane and H plane are almost the same.

Table 5-A: Comparison of the three types antenna, i.e. waveguide, waveguide woodpile EBG, corrugated horn

	Bandwidth	HPBW	Gain
waveguide	110-75=35 GHz	80 degrees in E plane 55 degrees in H plane	4 dBi in E plane 6 dBi in H plane
woodpile EBG	1 GHz	14 degrees in E plane 10 degrees in H plane	13 dBi
corrugated horn	110-75=35 GHz	5.2 degree in both E and H planes	24 dBi

of these three types of antennas are listed in TABLE 5-A.

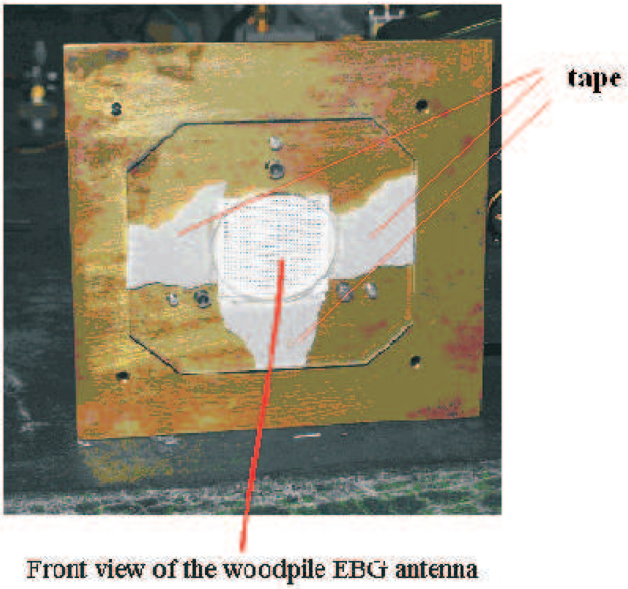

Figure 5.6: Front view of receiving antennas of the mm wave imaging system antenna,H-plane

5.3.2 Image quality comparison of using high gain and low gain antennas

The woodpile EBG antenna antennas used in the millimeter wave imaging system are shown in Fig 5.6 and Fig 5.7, where the thin tape is used to hold the EBG in place. This is a three element E-plane array with element spacing of 5mm. Applying high gain antenna in the proposed imaging system has two effects: the increased receiving signal level, and the reduced side lobe level which would collect the reflections from non-target areas, both contribute to the improvement of the image quality. The antenna can be considered as the low pass spatial frequency filter, only the spatial frequencies of the target are of interest, high harmonics beyond these are filtered out.

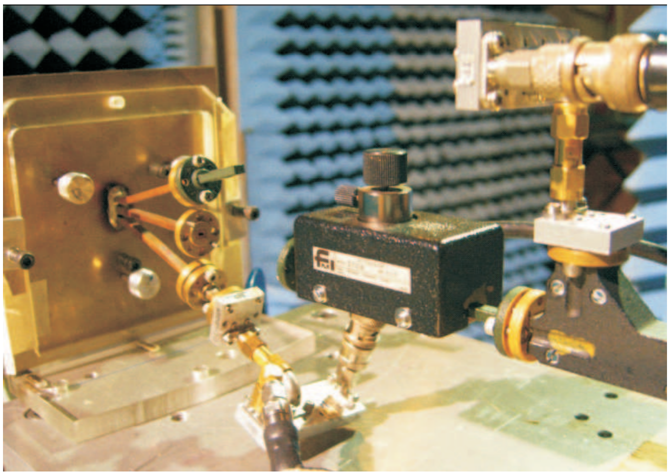

Figure 5.7: Woodpile superstrate antenna with three waveguide feeds (s=5mm)

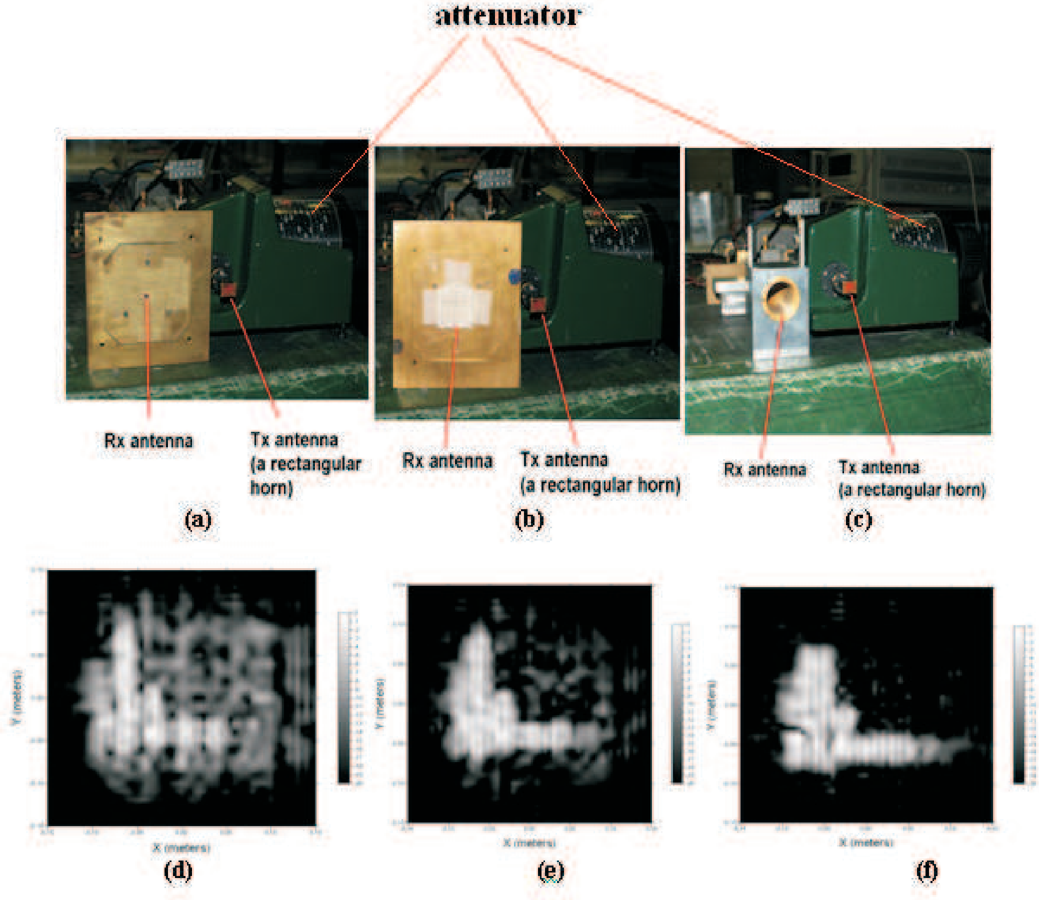

Figure 5.8: Woodpile EBG antenna performance comparison with other types of antennas (a)open ended rectangular waveguide (b)Woodpile EBG antenna (c)pyramid horn (d)(e)(f)MMW images corresponding to (a)(b)and (c)

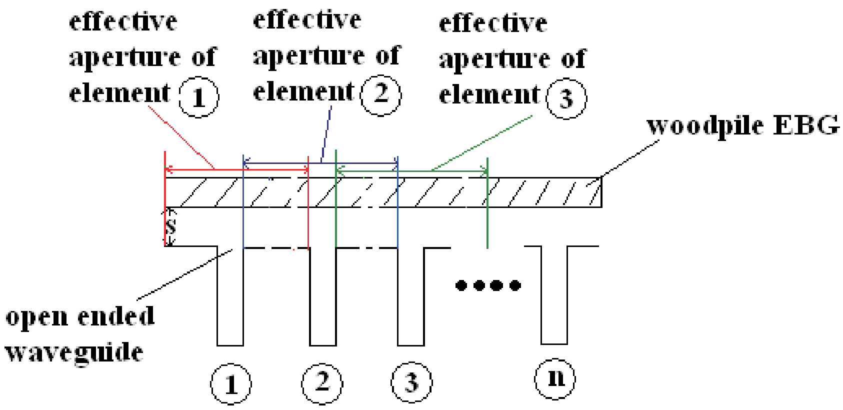

Figure 5.9: Woodpile superstrate antenna with waveguide feeds (s=5mm)

Table 5-B: Image quality comparison of the images produced by the three types of antennas

Image produced	SNR_I	NEΔR
waveguide Fig 5.8 (d)	1.5469	0.3072
woodpile EBG Fig 5.8 (e)	5.9288	0.2401
corrugated horn Fig 5.8(f)	6.9566	0.2249

An investigation of the imaging performance using the same transmitting antenna but three different types of receiving antennas (open-ended waveguide, woodpile EBG and pyramid horn), offering a range from wide to narrow HPBW, were used. They are illustrated in Fig 5.8 (a) (b) and (c). In order to investigate how the antenna beam width affects the target image, the same transmission power level 5 mW for all the three cases were maintained by adjusting the attenuation of transmit antenna, Fig 5.8(d)(e)(f) show the target images obtained from 3 different antennas as illustrated in Fig 5.8 (a) (b) and (c) respectively. The image quality can be seen greatly improved as the receiving antenna beam width decreases, see SNR_I and NEΔR values listed in TABLE 5-B. The improvement of the image quality is due to the increased receiver SNR and spatially filtering of high harmonics brought by the narrow beam width antenna.

Table 5-C: Size and volume reduction. Comparison of the woodpile EBG antenna and corrugated horn

Antenna	Minimum array element spacing	Length
corrugated horn	30mm	200 mm
woodpile EBG antenna	5 mm in E plane, 7 mm in H plane	50mm
size reduced	70 to 80 percent	70 to 80 percent

The proposed woodpile EBG antenna produces a good quality target image, which is better than that offered by an open end waveguide and it is comparable to the one by a high gain (and very large and expensive) corrugated horn antenna. EBG antenna has the benefit of being planar, easy fabrication and low manufacturing cost. But the most attractive feature of the woodpile EBG lens lies in the fact that it creates an array with overlapping effective aperture, see Fig 5.9, hence creating a very compact high gain array suitable for this imaging application. Since we wish a system with 5mm element spacing, this is an essential technology to realize an imaging array. See TABLE 5-C for the size reduced compared to the corrugated horn used. Volume reduction is more than 90 percent. Due to the size of the waveguide (1.27mm by 2.54mm), the minimum spacing is suggested to be 5mm in E plane and 7mm in H plane as investigation [5] shows that cross coupling between adjacent array element is still negligible for such a compact design.

5.4 Sparse Array In The Millimeter Wave Imaging System At 94 GHz

5.4.1 background

In chapter 3, it has been experimentally validated that the antenna element spacing of the imaging array does not have to be 0.5 wavelength or less in order to maintain the grating lobe free region within the field of view of 180 degrees. Since the target is only within a limited field of view angle (much less than 180 degrees) and the region outside of it is not of interest. For a measurement aperture of 200mm×200mm, 21×21 elements with uniform spacing of 3.13λ (f=94 GHz)a target of 200mm ×170 mm in dimension at a detection range of 1000mm can be effectively imaged. An array with such an element spacing has a grating lobe free field of view of about 40 degrees. The number of elements has been significantly reduced compared to that of the aperture with 0.5 wavelength element spacing. However, the number of elements can be reduced further if a sparse array is employed in the millimetre wave imaging system. Image quality produced by these less expensive arrays is comparable to those of the fully filled array. In the latter case spatial frequencies are sampled redundantly within the field of view and those redundant samplings would not contribute more information to the reconstruction of the target image.

It is ideal to choose a morphology and form an array so that the redundant samplings of the spatial frequencies are zero, however study has shown [7] that for the two dimensional array, except for the small 2D array, there is no zero redundancy sampling array existing, so the second best choice is to find out the minimum redundancy array. Hexagonal grids and cross product sparse arrays have been studied [8, 9] and their spatial frequency sampling redundancies are found to be significantly low, so they are used to form the array morphologies in the following measurements.

5.4.2 Active Millimeter Wave Imaging System Using a Sparse Array

There is considerable flexibility in choosing the morphology of a sparse array so that the redundant sampling of the spatial frequencies can be minimized. Finding out the minimum redundancy morphology for a large array involves heavy computation, as an initial step, the morphologies chosen in this section are determined via an empirical approach guided by the existing knowledge about sparse arrays.

Fig 5.10 to Fig 5.14 have the same dimension which is 200mm×200mm, Fig 5.10 is a sparse array composed of 9 hexagonal grids with 99 sampling points and Fig 5.11 has 9 cross products sub-arrays with 144 sampling points. Fig 5.12 is evolved from Fig 5.10 by adding more elements at those areas that are too sparse (elements within each small enclosed border are added), Fig 5.13 is evolved from Fig 5.12 (again elements within the enclosed borders are added) with 175 and 221 sampling elements respectively. Fig 5.14 is a fully filled aperture with 441 sampling elements. Note should be taken that the hexagonal grid and cross product sub-array are formed by keeping the corresponding elements that fall on these patterns and removing the rest, so their element spacing d (3.13λ) is the same as that of the corresponding full array in Fig 5.14, but different from the hexagonal grid spacing

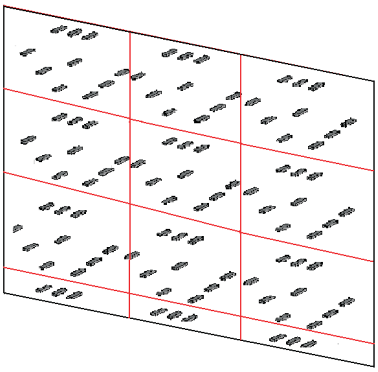

Figure 5.10: a sparse array composed of 9 hexagonal grids with 99 sampling points

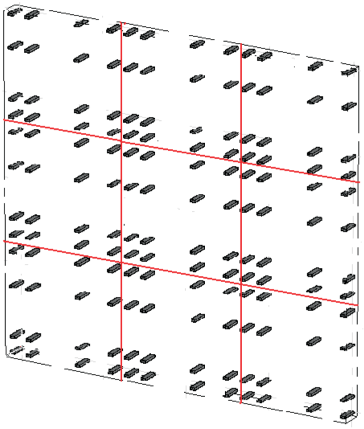

Figure 5.11: a sparse array composed of 9 cross products sub-arrays with 144 sampling points

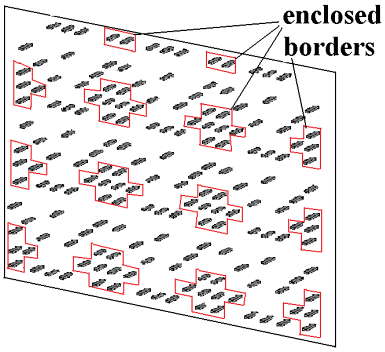

Figure 5.12: adding more elements at those areas that are too sparse (elements within each small enclosed border are added,with 175 sampling elements)

defined in [8] and this is for the convenience of measurement.

Experimental verification of the effectiveness of these sparse arrays on imag-

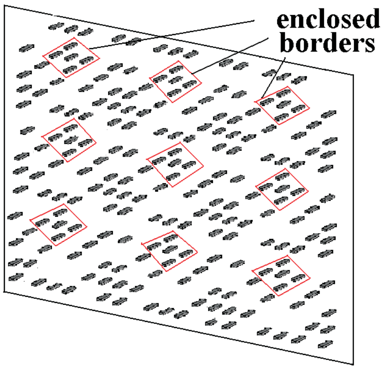

Figure 5.13: adding more elements at those areas that are too sparse (elements within each small enclosed border are added,with 221 sampling elements

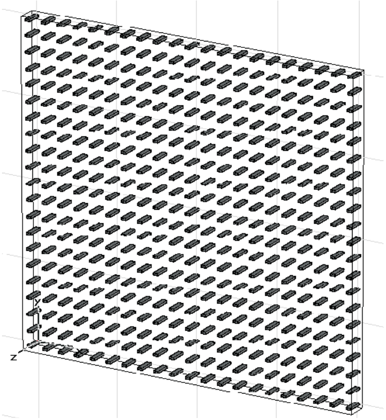

Figure 5.14: fully filled array aperture with 441 sampling elements

ing follows the same procedure as that of the fully filled array, except setting the received field intensity as 0 for those elements which do not coincide with the hexagonal grid and cross product pattern. The same holographic processing algorithm is used to generate target images.

5.4.3 Experiments results

Fig 5.15 is the optical image of the target (200mm by 170 mm in dimension) and it is placed 1000mm away from the measurement aperture. Fig 5.16(a) (b) (c) (d) (e) are field distributions across the measurement apertures using the morphologies

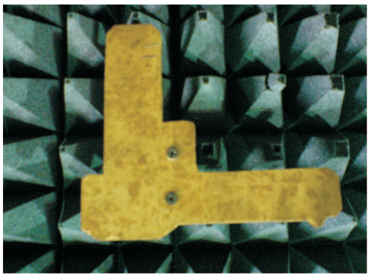

Figure 5.15: optical image of the target

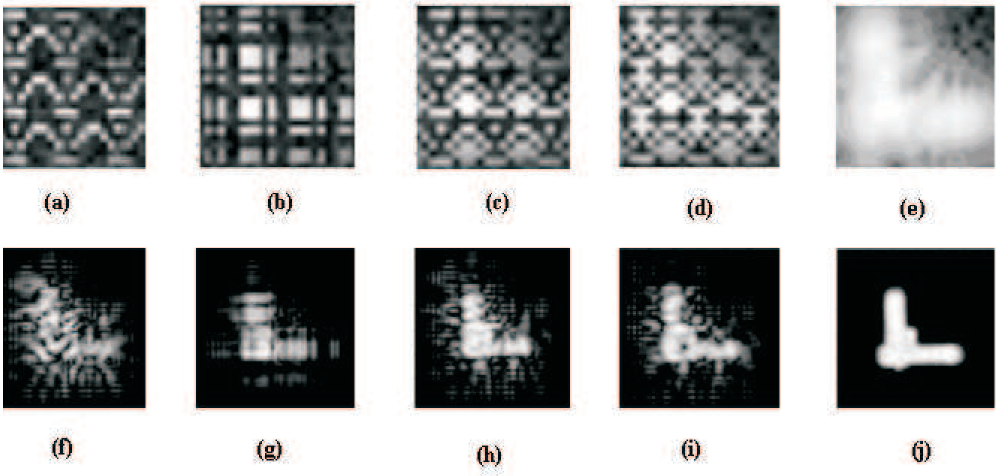

Figure 5.16: (a) to (e) field distribution (amplitude only) across the sparse array aperture (f) to (j) target images produced by different sparse arrays.

Table 5-D: Image quality of the scans according to three types of morphologies

morphology	SNR_I	NEΔR
Fig 5.16(f)	3.3834	0.2422
Fig 5.16(g)	4.9288	0.2001
Fig 5.16(h)	5.4708	0.1800
Fig 5.16(i)	6.3116	0.1596
Fig 5.16(j)	32.45	0.0229

in Fig 5.10 to Fig 5.14 respectively. Fig 5.16(f) to (j) are the corresponding images produced by holographic processing, their SNR_I and NEΔR are calculated and listed in TABLE 5-D.

Comparing the image qualities from Fig 5.16(f) to (j), it is found Fig 5.16(i) has a SNR_I of 6.3116 and it is reasonably acceptable even without using any other image enhancement techniques, in which only 221, i.e. about half of the 441 full array elements were used. It is the best array geometry in terms of image quality and array elements count used.

5.4.4 Discussions

The investigation performed in this section verified the feasibility of using a sparse array (though the morphology is not optimized) for the millimeter wave imaging. A slight compromise of the image quality is rewarded by a significant reduction of the number of imaging array elements. An optimized sparse array morphology for a given number elements and aperture dimension is a mathematically problem [9]. The optimization involves heavy computation, which is pending further study. Similar work has been done in phased array radar, while the same theory of finding out the best geometry of the sparse arrays applies, the difference lies in the signal processing. In the case studied here, the microwave holographic processing is used, while the radar technology uses correlations between selected element pairs to work out of the sensitivity at different spatial frequencies [7].

5.5 Multiple frequency/Wide Band Holographic Millimetre Wave Imaging

5.5.1 Background

Much has been done in the previous investigations using the single frequency holographic imaging technique. Although such a system can be used to retrieve the target image effectively, and implementation is relatively easy compared to the wide band frequency operation system, there are at least two areas where the technique needs to improve. Firstly, the single frequency operation system cannot resolve range although this is not a major criteria for a security imaging system. Secondly, and more importantly the 2D target image produced by the single frequency holographic approach is prone to speckle caused by the roughness of the target surface.

Theoretically speaking, if the frequencies satisfies the Nyquist sampling criterion, the more frequencies are used, the more effectively the speckle is removed. This is because the speckle distributions at these frequencies are different and when they add up, the image brightness increase more than the speckle, hence the image to noise contrast increases. For demonstration purpose, 5 frequencies are used in the following experiment. The phase shift resulting from a change in wave number Δk is $2\Delta k R_{max}$ when the frequency scans. Appling Nyquist sampling criterion, we have $2\Delta k R_{max} \leq \pi$. Substituting Δk with $2\pi\Delta f/c$ yields equation (6.1) [10].

$$\Delta f \leq c/(4 \times R_{max}) \tag{5.1}$$

Where Δf is the sampling frequency interval, c is the light speed, R_{max} is the maximum target range. In the case studied here R_{max} is 1 metre, so Δf is 0.075 GHz.

In general, using multiple frequencies brings a process gain or the increased system dynamic range which is equal to the square root of the number of frequency samples [11]. For example, if 512 frequencies are used, the process gain will be $20\log\sqrt{512}$=22.6 dB. If 5 frequencies are used, then a factor of $20 \log\sqrt{5}$=7 dB is improved.

5.5.2 The experiment of the multiple frequency/wide band holographic imaging system

Experimental verification is based on the single frequency holographic imaging system but the frequency is changed and the data set is recorded each time. The recorded raw data sets are processed frequency by frequency, then the images for all the frequencies are averaged, processed and rescaled. 5 frequencies were selected, i.e. 94.0, 94.03, 94.06, 94.09, 94.12 GHz, at an interval of 0.03 GHz (satisfying the sampling frequency interval criteria $\Delta f \leq 0.075$ GHz). The image produced by the sparse imaging array used in Fig 5.13 has the speckle effect and was chosen for this demonstration. Fig 5.17(a) to (e) shows the target images at selected frequencies. Speckles are very obvious in each image, but their distributions in each image are slightly different.

Fig 5.18 is the addition of 5 images, i.e. from Fig 5.17 (a) to (e). Their SNR_I NEΔR are calculated and listed in TABLE 5-E. It can be seen that there is sig-

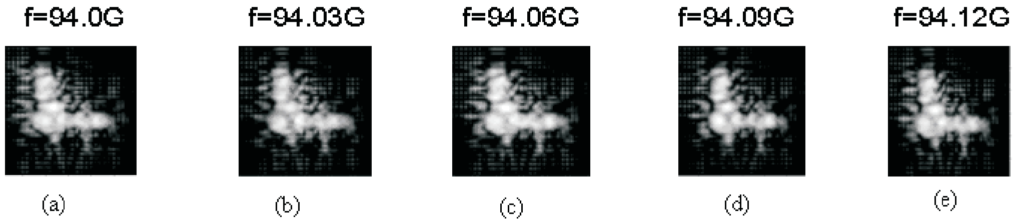

Figure 5.17: (a) to (e) target images produced at frequency 94.0, 94.03, 94.06, 94.09, 94.12 GHz respectively

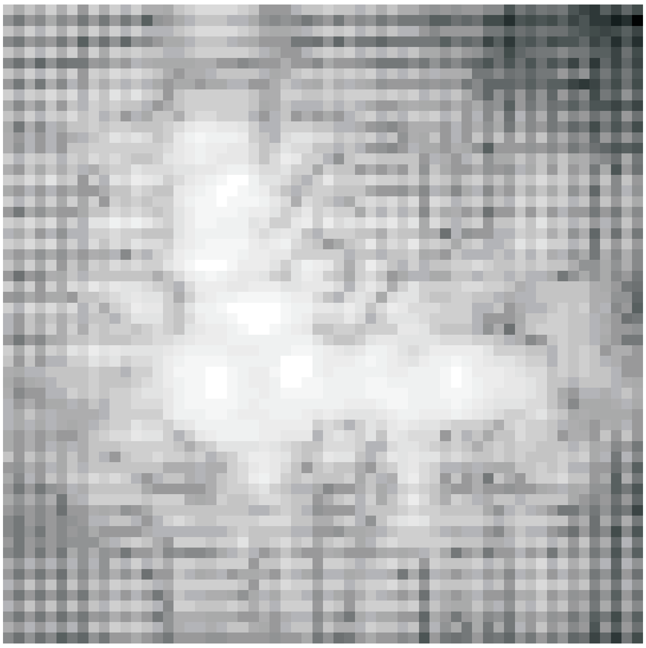

Figure 5.18: Addition of Fig 5.17 (a) to (e))

nificant increase of SNR_I values from about 4 in Fig 5.18 to 40 in Fig 5.19. Note must be taken there is a change of the grey scale range for the image resulted. The grey scale range of Fig 5.18 was rescaled back to 20dB which is the case in Fig 5.17, then Fig 5.19 was resulted. It can be seen speckles were greatly eliminated.

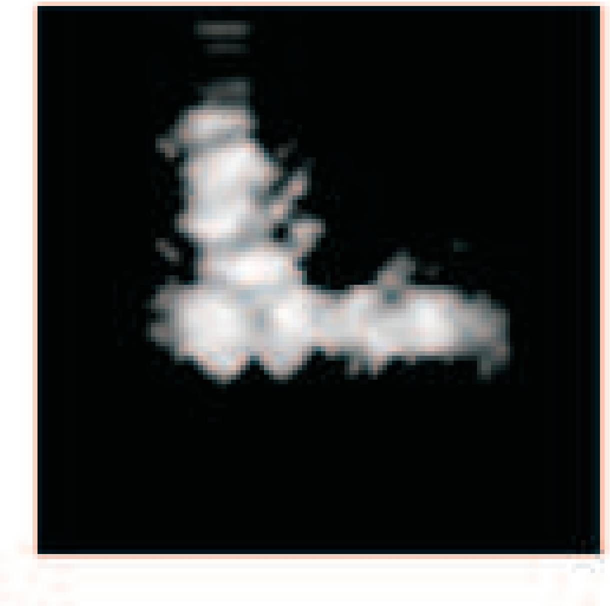

Figure 5.19: Image after grey-level rescaling, curtesy of Pengwei Hao, School of Electronic Engineering and Computer Science, Queen Mary University of London

Table 5-E: Image quality of the scans using five different frequencies, i.e. 94.0, 94.03, 94.06, 94.09, 94.12 GHz

frequency	SNR_I	NEΔR
Fig 5.17(a)	5.6488	0.1556
Fig 5.17(b)	4.3908	0.1982
Fig 5.17(c)	4.2312	0.2057
Fig 5.17(d)	5.8247	0.1515
Fig 5.17(e)	5.6730	0.1557
Fig 5.18	40.2030	0.0248

5.5.3 Discussions

The speckle removal technique using multiple frequencies are based on speckle distribution difference at different frequencies. The difference is due to the electric path length change when the frequency scans. The change of electric path length causes the addition (constructively and destructively) pattern variance which is exploited for image enhance. When the images at different frequencies add up, the speckle brightness increases slower than that of the target area, so the contrast increases and this is the reason why image quality is enhanced. Although only 5 frequencies were chosen for the averaging to eliminate the speckles, it can be seen that this very narrow bandwidth (0.13 percent) is rather effective in terms of image quality improvement, giving a seven fold (8 dB) increase in SNR_I, in line with $20log\sqrt{5}$=7 dB. In a real wide band imaging system, more sampling frequencies could be used. For the woodpile EBG antenna, the bandwidth is 1 GHz, if the interval of 0.03 GHz is used, then overall 33 frequencies could be used. This brings a dynamic range increase of $20\log\sqrt{33}=15.2$ dB.

5.6 Conclusions

The feasibility study of applying a woodpile EBG antenna in millimeter wave imaging is presented. The experimental results verified that the proposed antenna has the capability of producing good quality target images comparable to conventional high gain horns due to the shared aperture possibility. When forming an imaging array using woodpile EBG antenna, due to the size of the waveguide, the minimum spacing is suggested to be 5mm in E plane and 7mm in H plane.

It is feasible to use a sparse array (though the morphology is not optimized) for the millimeter wave imaging for the reduction of array elements. A morphology with just a half of the full array element counts still offers an acceptable image quality, though the optimization is pending further study.

For the investigation of the image enhancement using multiple frequencies, it can be seen that multiple frequency imaging is rather effective with significant

Table 5-F: summary of the investigation on new device and technique for image enhancement

device or techniques	quantity
woodpile EBG antenna bandwidth	1 GHz
woodpile EBG antenna HPBW	E plane 14 degrees, H plane 10 degrees
woodpile EBG antenna gain	13 dBi
woodpile EBG antenna array element spacing array element spacing	5 mm in E plane, 7 mm in H plane
sparse array morphologies	potential reduction of the array elements, but need optimization.
multiple frequency for image enhancement	33 frequencies, 0.03 GHz interval dynamic range increase: 15.2 dB

increase of the SNR_I. TABLE 5-F summarizes the investigations performed in this chapter.

References

[1] Lee, Yoonjae; Lu, Xuesong; Hao, Yang; Yang, Shoufeng; Evans, Julian R. G.; Parini, Clive G.; *Rapid Prototyping of ceramics millimeter wave matematerials: simulations and experiments* Microwave and Optical Technology Letters, Vol. 49, No. 9, September 2007, pp. 2090.

[2] Zhang, L.; Hao, Y.; Parini, C. G.; Dupuy, J.; *An experimental millimetre wave imaging system* Loughborough Antenna and Propagation Conference (LAPC '08), Loughborough (United Kingdom), 17-18 March 2008.

[3] Zhang, L.; Hao, Y.; Parini, C. G.; Dupuy, J.; *An Investigation of Antenna Element Spacing on the Quality of Millimetre Wave Imaging* The 2008 IEEE APS International Symposium on Antennas and Propagation and 2008 USNC/URSI National Radio Science Meeting in San Diego, California, USA.

July 05-12, 2008.

[4] Lee, Yoonjae; Lu, Xuesong; Hao, Yang; Yang, Shoufeng; Evans, Julian R. G.; Parini, Clive G.; *Low-Profile Directive Millimeter-Wave Antennas Using Free-Formed Three-Dimensional (3-D) Electromagnetic Bandgap Structures* Antennas and Propagation, IEEE Transactions on. Volume: 57, Issue: 10 , Part: 1. Digital Object Identifier: 10.1109/TAP.2009.2029299. Publication Year: 2009. Page(s): 2893 - 2903.

[5] Lee, Yoonjae; *Design and Analysis of metamaterial-based antennas* PhD thesis, Queen Mary University of London, 2009.

[6] Lee, Yoonjae; Hao, Yang; Parini, C. G.; *Low profile high directivity millimetre-wave antenna using freeformed metamaterial* Infrared and Millimeter Waves, 2007 and the 2007 15th International Conference on Terahertz Electronics. IRMMW-THz. Joint 32nd International Conference on. Publication Year: 2007. Page(s): 943 - 944.

[7] Moffet, Alan T.; *Minimum-Redundancy Linear Arrays* IEEE Transactions on Antennas and Propagation, VOL. AP-16, No.2, MARCH 1968.

[8] Salmon, N. A.; Beale, J.; Parkinson, J.; Hayward, S.; Hall, P.; Macpherson,R.; Lewis, R.; Harvey, A.; *Digital Beam-forming for passive millimeter wave security imaging* The Second European Conference on Antennas and Propagation EuCAP 2007

[9] Meurisse, Yann; Delmas, Jean-Pierre; *Bounds for Sparse Planar and Volume Arrays* IEEE Transactions on Information Theory, Vol. 47, No.1, January 2001.

[10] Sheen, David M.; Mcmakin, Douglas L.; Hall, Thomas E.; *Three-dimensional millimeter-wave imaging for concealed weapon detection* IEEE Trans. MTT, vol. 49, no. 9, pp. 1581 - 1592, 2001.

[11] Slater, Dan; *Near-Field Antenna Measurements* Artech House, Inc. 1991, pp.

230.

Chapter 6

Natural Resonant Frequency Extraction for Concealed Target Detection

6.1 Introduction

In this chapter a resonance based target recognition approach is investigated as a possible way of providing extra information about the target and thus offer improved levels of threat detection from a microwave and millimetre wave imaging system. The method, which is called singularity expansion method (SEM), was first reported by C. E. Baum in 1971 [1], it is based on the analytic properties of the electromagnetic response as a function of two-sided Laplace transform variables which can be called the complex frequency. These complex frequencies are associated with the target shape, size and material, hence they are called natural resonance frequencies which can be used to characterize the target. One important feature of complex natural resonance (CNR) frequencies is that they are aspect independent, which is suitable for real situations that the incidence angle of the interrogating pulse to the object can not be fixed for non-cooperative targets.

There are two steps when applying the resonance based target recognition approach. The first step is to obtain the impulse response from the object under detection. A pulse of microwave/radio frequency or a swept frequency source is used to illuminate the target space, once the impulse response is obtained, the second step is to extract the CNR frequencies.

My contribution in this area of study is to use the transient solver in CST Microwave Studio [2] to obtain the impulse response, which differs from conventional frequency domain techniques such as method of moment (MoM), then applying Inverse Fourier Transform to obtain its time domain data sets as demonstrated in [3].

As for the CNR frequency extraction, the techniques developed include Prony's method, the pencil-of-functions(PoF) method, E-pulse method. However, there are limitations when applying these techniques. For example, Prony's method and PoF method are sensitive to noise while E-pulse and K-pulse need an initial guess [4]. Genetic Algorithm (GA) is a statistical optimization algorithm and does not need an initial guess for optimization and is not sensitive to noise. As proved in [5], even though the number of modes are underestimated, the CNR frequencies extracted are still correct, whereas for the same case Prony's method would fail. In view of this, the GA is chosen for the CNR frequency extraction in this study. The extracted target signature (characterized by the extracted complex natural resonance frequencies) is compared to the database that stored signatures of the all the known weapons to determine whether there is a match. If yes, an alarm is automatically activated.

In the following sections, the procedure of the extraction of the CNR frequencies is introduced first, then it is applied to a few targets whose CNR frequencies either can be calculated theoretically or can be obtained by other means. By comparison, we can understand the effectiveness and limitations of using the resonance based target recognition approach for concealed target detection, however, the limitations can be circumvented by the combination with imaging based CWD approach.

6.2 Theory of resonance based target recognition and the application of GA for CNR frequency extraction

Baum proposed a mathematical model to represent the late time response in the early 1970s. The mathematical model [6] is

$$r(t) = \sum_{m=1}^{M} a_m e^{\sigma_m t} cos(\omega_m t + \phi_m) \quad t \geq T_L \tag{6.1}$$

Where r(t) is the residue of the late time response, a_m and ϕ_m are aspect dependent amplitude and phase of the m^{th} mode, $s_m = \sigma_m + j\omega_m$ is the complex natural frequency of the m^{th} mode and it is aspect independent. T_L is the beginning of the late time. M is the number of resonant modes estimated, and the late time starts when the forced response vanishes. This forced response is caused by direct reflection from the illuminated targets and it is called the early time response. When the pulse hits the surface of the target, it induces surface current. The surface current flows on the surface and radiates EM wave. Since the geometry of the object decides how the excited current flows, it is not surprising that the CNR frequencies are related to the target geometry. This is the physics of resonance based target recognition.

Beginning of late time can be estimated using the following formula,

$$T_L = T_b + 2T_{tr} + T_p \tag{6.2}$$

Where T_b is the incidence wave travelling time from the source to the leading edge of the target plus the travelling time from the leading edge back to the probe. T_{tr} is the one-way transient time along the line of sight of the object and T_p is the width of the interrogating pulse (measured between the two percent of maximum points), see Fig 6.1. Note should be taken that since the resonance mechanism of the dielectric objects is much more complex than that of their metallic counterparts, equation 6.2 cannot be used directly to estimate the beginning of late time if the objects under interrogating are not metallic. For dielectric objects, incidence EM can propagate inside the objects and excite the interior resonances. The forced response vanishes later than it would be if it is an conducting object of the same dimension, which will be demonstrated in Section 6.3.2.

Theoretically, since CNR frequencies are independent of incident angles, for any incidence angle, from its corresponding impulse response the same CNR frequencies should be able to be extracted. However, in practice not all the modes can be extracted at some angles. This is because the residue r(t) in equation 6.1 can be

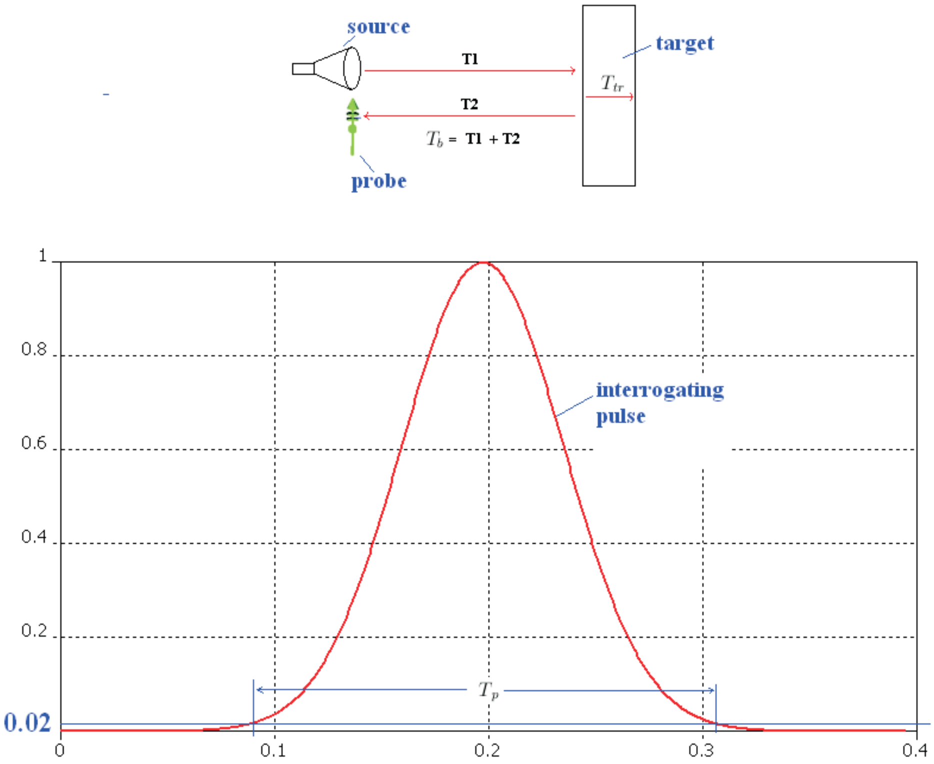

Figure 6.1: The illustration of Tb, Ttr and Tp

very small even zero for some modes as a_m and ϕ_m are aspect dependent.

Once the late time response is obtained either by simulation or measurement, the remaining task is to use equation 6.1 to represent the late time response. There are a few extraction methods such as Prony's method [7], the pencil-of-function method (PoF) [8] and E-pulse method [9], however, a GA based optimization program is used here as it possesses a few advantages that other methods lack. First of all, it does not require an initial guess which prevents the optimization from falling into a local minima. Secondly, it is insensitive to noise, and what is more, even though the number of modes are underestimated, the results extracted are still very accurate. In the real case, the a priori information of the number of resonant modes of the concealed objects is not available and the measured impulse response is not noise free.

The curve fitting java code based on Genetic Algorithm which is an open source code for general purposes [10]. The author here made some modification and used it for the extraction of CNR frequencies. To use it, save the late time response obtained from CST Microwave Studio as y.txt first, then set the mathematical expression that is used to represent the late time response as equation 6.1, then load y.txt and specify the time step and number of sampling points, then run the code and get the 4 coefficients for equation 6.1, $s_1 = \sigma_1 + j\omega_1$ is the first mode of the resonant frequency, then subtract $s_1 = \sigma_1 + j\omega_1$ from y.txt, repeat the procedure to get the second mode and so on. Fig 6.2 is the flow chart of the CNR frequency extraction procedure based on GA.

In the GA code developed for this chapter, there are 4 genes which represent $\alpha_m, \sigma_m, \omega_m, \phi_m$ in (6.1) in one chromosome and the population of chromosomes is 100. The Fitness is defined as the inverse of the absolute value of the difference between the original data set and reconstructed waveform. Using two point crossover, two decimal points precision, a mutation probability of 10 percent, maximum number of generations 4000, for a data set of 400 elements, the extraction computing time for one mode is about 20 seconds in a Pentium III, CPU 1.7 GHz, Memory 512 MB PC. Minimizing the computation time has not been considered here.

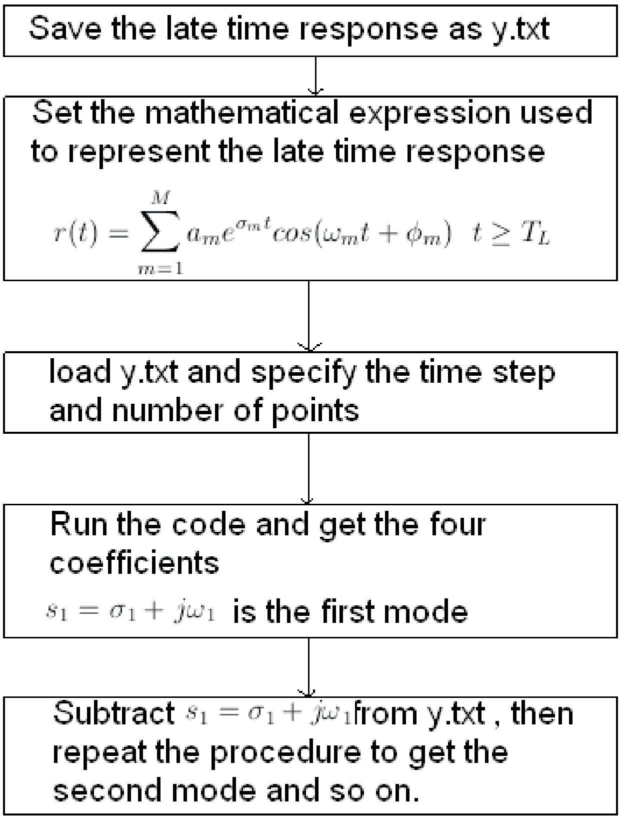

Figure 6.2: Flow chart of the CNR frequency extraction procedure based on GA

6.3 Simulation results

The theory and CNR frequency extraction procedure based on GA has been introduced above. In this section, examples to verify its validity will be given. The simulation tool used here is CST microwave studio. With its transient solver, which is suitable to solve scattering problems, the impulse responses of a metallic sphere, a dielectric sphere and a thin wire with two different inclination angles are simulated. The reason of choosing these particular targets is because their theoretical results can be exactly calculated. By comparison, the validity of the simulation results can be confirmed. Once its validity is verified, the same simulation can be extended to other more complex targets.

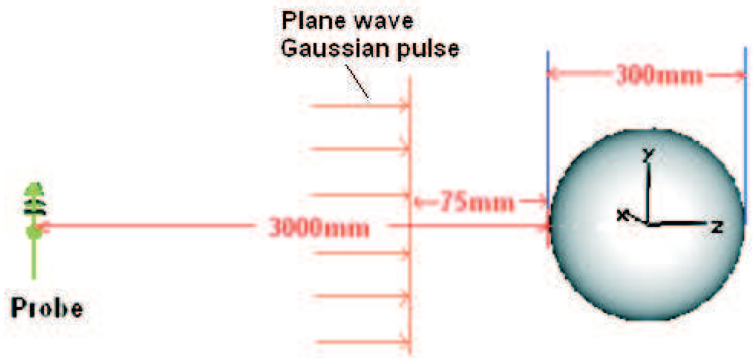

Figure 6.3: The conducting sphere D=300mm

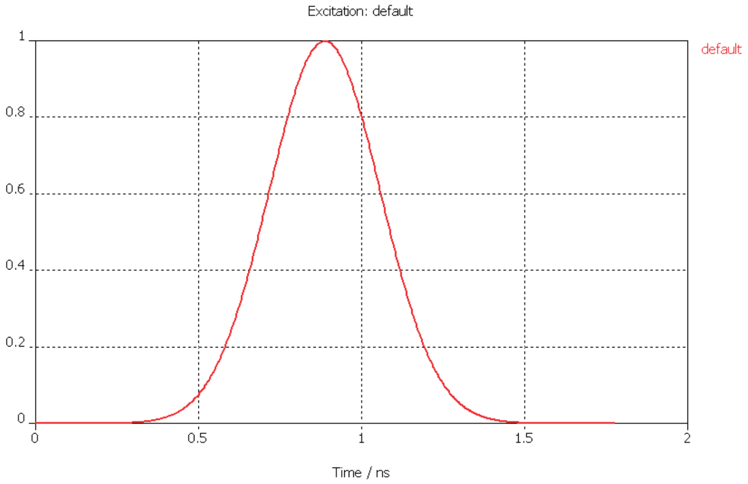

Figure 6.4: The interrogating Gaussian pulse signal

6.3.1 The conducting sphere

Fig 6.3 shows a conducting sphere of 300mm in diameter. The incidence Gaussian pulse plane wave signal is shown in Fig 6.4 and it travels along the z axis and the E field is parallel to x axis. Fig 6.5 is its backscattering impulse response received by a probe in the far field. Apply equation 6.2, for this particular setting, T_p is about 1.1 ns, T_L is estimated to be 13.39 ns, the late time response is shown in Fig 6.6.

By applying GA to the late time response the first 11 modes can be extracted.

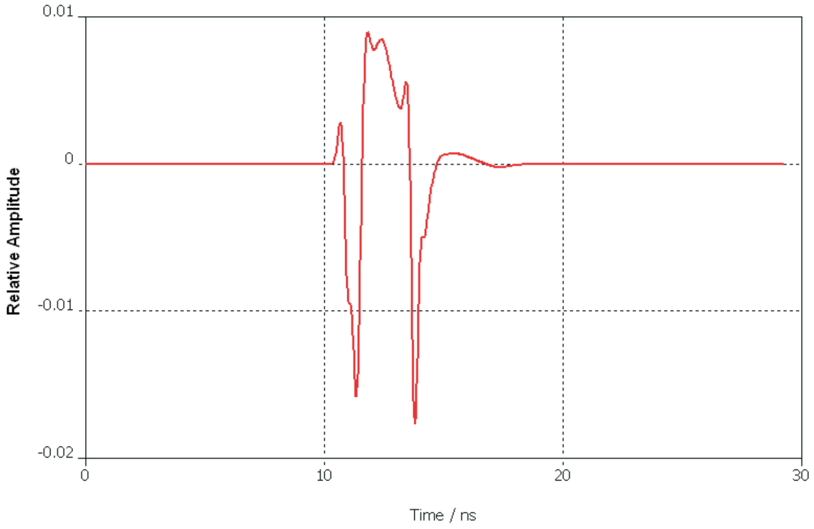

Figure 6.5: Backscattering impulse response of the conducting sphere

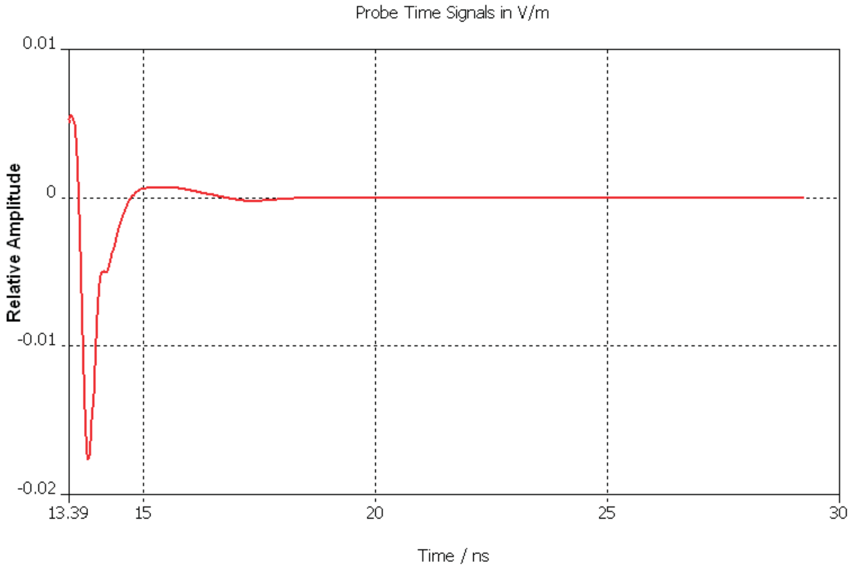

Figure 6.6: The late time part of the impulse response of the conducting sphere

The extracted CNR frequencies are listed below in the left column of TABLE 6-A. Their corresponding theoretical results in the right column is taken from [11].

By comparison, it can be seen that the imaginary parts of the corresponding CNR frequencies between the simulation and theoretical results are quite close to

Table 6-A: The extracted CNR frequencies

Simulation	Exact theoretical results
S1=-0.43+j1.14	S1= -0.5+j0.866
S2=-0.41+j1.79	S2=-0.7020+j1.807
S3=-2.017+j2.55	S3=-0.8430+j2.758
S4=-0.59+j3.81	S4=-0.9540+j3.715
S5=-1.30+j4.99	S5=-1.048+j4.676
S6=-0.73+j7.59	S8=-1.267+j7.58
S7=-1.26+j8.74	S9=-1.327+j8.553
S8=-2.58+j11.51	S12=-1.483+j11.48
S9=-1.88+j12.55	S13=-1.528+j12.46
S10=-1.25+j15.74	S16=-1.653+j15.40
S11=-1.723+j19.74	S19=-1.762+j18.34

each other. The real parts do not agree as well as the imaginary parts, but for target recognition purposes the imaginary parts are sufficient. The complex frequency $s_m = \sigma_m + j\omega_m$ is the m^{th} singularity in the plane formed by the the variable s of the Laplace transform of the impulse response. Equation 6.1 is a summation of m damped sinusoids, in which the real part (a negative value) determines how fast this mode decays and the imaginary part characterizes its sinusoidal frequency. The first 11 modes are good enough to represent the original late time response. The comparison between the original simulated late time response and the 11 modes reconstructed waveform can be found in Fig 6.7. The results indicate the proposed approach can extract CNR frequencies for a metallic sphere correctly.

6.3.2 The dielectric sphere

Dielectric objects behave differently from conducting ones when illuminated by interrogating pulses. For conducting objects such as a metallic sphere, the incidence EM does not penetrate into it, and the contribution of the backward scat-

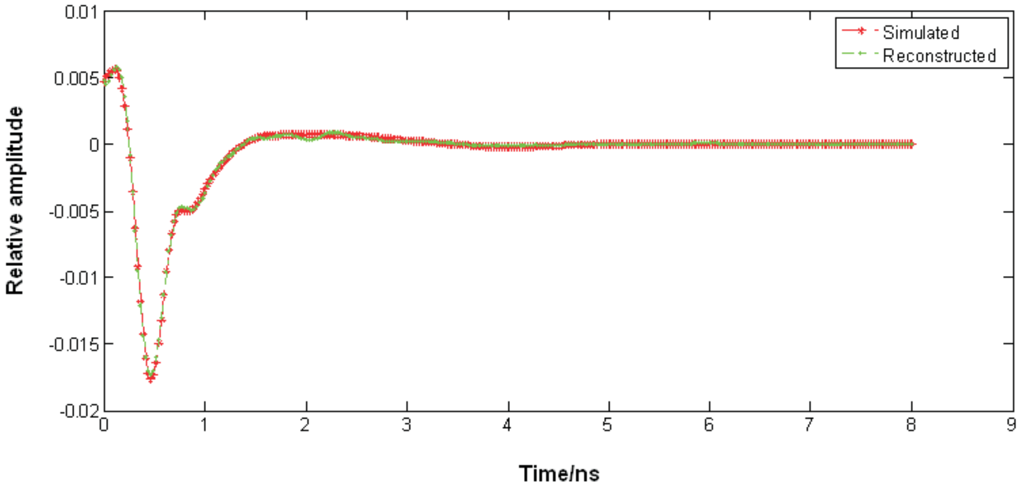

Figure 6.7: Comparison between the original simulated late time response and the 11 mode reconstructed waveform

tering is composed of two parts, one is contributed by the specular reflection, the other part is contributed by the creeping wave. In order to induce a resonant response in an object, it is necessary to illuminate it in the frequency band of natural resonance. In general, the frequency dependence of an object's radar return can be categorized into three overall regions: Rayleigh, resonance, and optical regions. Fig 6.8 [12] shows the Radar cross section (RCS) of a sphere as a function of its circumference measured in wavelengths, $\frac{2a\pi}{\lambda}$=ka, where a is the radius of the sphere and k=$\frac{2\pi}{\lambda}$ is the wave number. The RCS is plotted normalized to the geometric cross section of the sphere, πa^2. The resonance region return of the sphere has several peaks which corresponds to a the natural electromagnetic resonances of the sphere. The location of the resonances frequencies is directly related to the circumference of the sphere. The first peak, and the highest RCS, corresponds to the point where the circumference equals exactly one wavelength. At this frequency, a wave travelling completely around the sphere's surface constructively adds to a wave scattered from specular point at the sphere's front surface. But the resonance mechanism of a dielectric object is much more complex than a metallic one as the incidence EM can penetrate into it and excites interior resonance. The interior multipath reflections and surface creeping wave might add constructively to the specular point at the sphere's front surface. Considering a dielectric sphere of 1 meter in diameter and permittivity 5 in Fig 6.9. The interrogating Gaussian pulse plane wave signal is shown in Fig 6.10 and its impulse response is shown in Fig 6.11. The determining of the start point of the late time should not be the same as a conducting sphere of the same size. The estimation of the T_L is done by calculating the time when forced response vanishes. When the interrogating pulse penetrates into the dielectric sphere, it propagates inside it and hits the other side of the interior wall it is partly reflected back, then penetrates the dielectric sphere again into free space and contributes to the backscattering. There could be multiple backward reflections, here we consider the first one as it is the major one. As this is the forced response, we must exclude it from the late time response. The beginning of late time response starts just after this forced response vanishes. The transit time T_{tr} in equation 6.2 should have a time factor $\sqrt{\varepsilon_r}$ as the incidence EM travels $\sqrt{\varepsilon_r}$ times slower in the dielectric sphere than it would in free space. T_L is estimated to be 61.147 ns in this particular case, in which pulse width T_p is 4.5 ns. The late time response is shown in Fig 6.12.

The same extraction procedure is repeated as was done for the conducting sphere case. Fig 6.13 is the comparison between the simulated late time response and reconstructed late time waveform of the first 16 extracted modes. The left column of TABLE 6-B are extracted imaginary parts of CNR frequencies and the right column are their corresponding theoretical results [13]. Note should be taken that the theoretical results of the CNR frequencies are normalized in the literature. In order to make it comparable with the simulated results in this chapter, they are

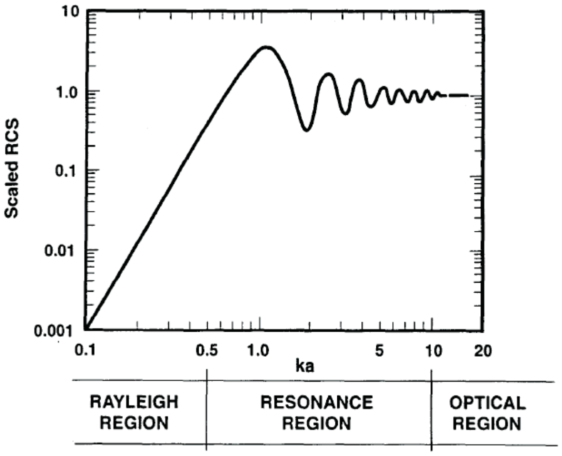

Figure 6.8: Radar cross section is enhanced in the resonance region [12].

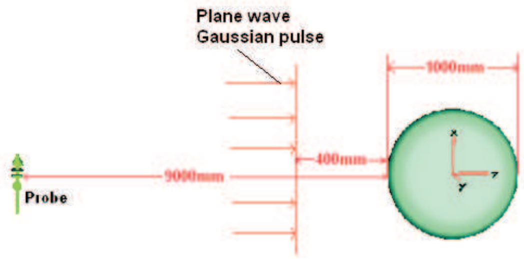

Figure 6.9: Dielectric sphere of 1 meter in diameter and permittivity 5

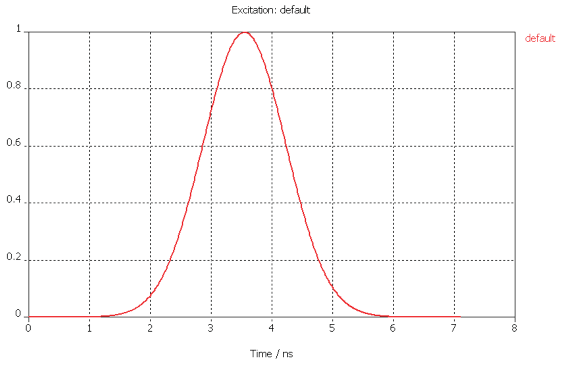

Figure 6.10: The interrogating Gaussian pulse signal for the dielectric sphere

converted back to radians.

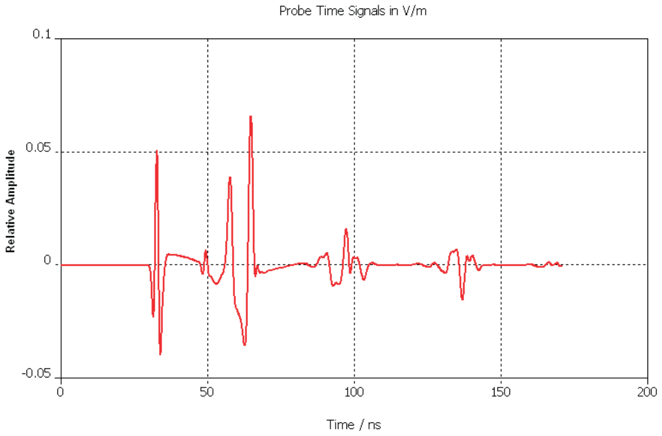

Figure 6.11: Impulse response of the dielectric sphere

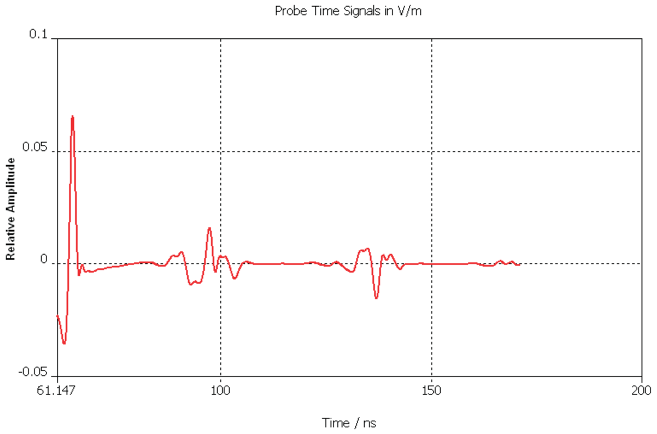

Figure 6.12: Late time response of the dielectric sphere

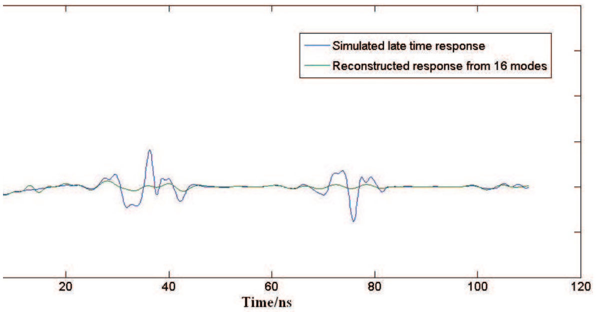

Figure 6.13: The comparison between simulated late time response and reconstructed late time response

Table 6-B: The extracted CNR frequencies

Extracted radian Freq. by GA in this chapter	Theoretical Freq. [13]
0.22	
0.36	0.3890
0.48	
0.56	0.5622
0.64	
0.75	0.732
0.97	
1.00	
1.03	1.0353
1.16	1.2168
1.38	1.3894
1.46	
1.55	1.5493
1.97	2.0990
2.23	2.2949
2.55	2.4859

By comparison it can be concluded, for a dielectric sphere, its resonance frequencies can be largely extracted, but with a lot of false and inaccurate results. Since the density of the distribution of the CNR frequencies is very high, sometimes 2 or 3 closely located frequencies represent one frequency. The results can be improved by more accurately estimating of the starting point of the late time.

In the next simulation, such a method is used on a thin wire with different inclination angles, which is to prove that the approach still works in a practical situation.

6.3.3 Complex natural resonant frequency extraction at arbitrary incidence angles.

In the real CWD situation, the target orientation can be arbitrary. The extraction of CNRs from a thin wire shows that the approach adopted i.e. using the transient solver of Microwave Studio to obtain the impulse response then using GA to extract the CNRs is still applicable. The complete set of an object's CNRs can be obtained by changing the angles of the object in the simulation. According to the theory of Singularity Expansion Method (SEM) [1], the late time response of a target from an interrogation pulse can be represented by a sum of series of damped sinusoids. What makes it interesting is the incidence aspect independent nature of the CNR frequencies as in the real situation the incidence angle will be arbitrary. But the issue is that not all the resonant modes can be excited due to the small residues excited at some incidence angles. In order to build up the database of the CNR frequencies for a particular object, it has to be interrogated at different incident angles. On the other hand, since a set of excited modes corresponds to a particular incidence angle, by looking at the modes excited, the orientation of a particular target can be estimated. A thin wire is used as the example to verify the validity of the proposed approach. Two sets of CNR frequencies are extracted for the incidence angle 15 degrees and 75 degrees respectively. It is found that only part of the CNR frequencies are extracted in the latter case.

The wire is 1 metre in length with a length to radius ratio L/a 200. It is in z-y plane and the inclination angle to the z axis is 15 degree, see Fig 6.14. The interrogating incidence pulse propagates along z axis and E-field is parallel to y-axis. Fig 6.15 is its simulated late time response and the reconstructed late time

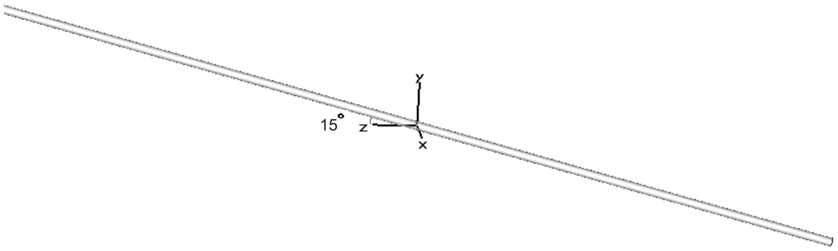

Figure 6.14: A thin wire with inclination of 15 degree

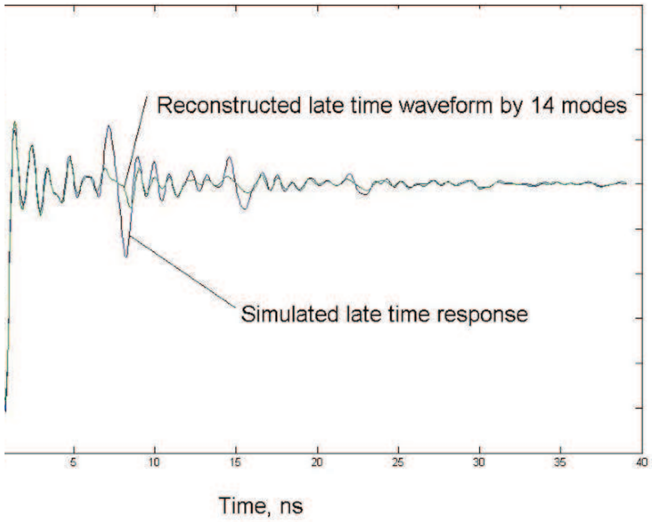

Figure 6.15: Comparison between the reconstructed and the original waveform

waveform by the first 14 modes. TABLE 6-C is the comparison between the results by MoM [14] and the simulated results in this chapter. Only the imaginary parts of the CNR frequencies are considered.

For the first 14 modes extracted, some of them are very close hence are considered as one frequency. In column 2, the normalized results in column 1 by MoM methods are converted into radian for easy comparison with the simulated results in column 3. Although some of the modes are correctly extracted, there are modes that are missing, repeated and inaccurate.

Table 6-C: Comparison between results by MoM and the technique proposed in this paper for 15 degree incidence angle

MoM(normalized) [14]	Results by MoM converted to radian	Fequencies extracted by GA in this chapter
2.91	0.87	0.86
6.01	1.80	1.74; 1.75
9.06	2.72	2.45; 2.58
12.2	3.66	3.40
15.3	4.59	4.3; 4.98; 4.99
18.4	5.52	5.38; 5.88
21.5	6.45	6.57
24.6	7.38	7.39
27.7	8.31	not excited
30.8	9.24	8.98

Changing the orientation of the wire by adjusting the inclination angle between the wire and z axis to 75 degree, see Fig 6.16, the extraction procedure is repeated. Fig 6.17 is its simulated late time response and the reconstructed late time waveform by the first 13 modes. TABLE 6-D are the comparison to the results in [3, 14]. Only the imaginary parts of the CNR frequencies are considered. Again, the closely located CNR frequencies are merged as one frequency. By comparison, it can be seen the 5th, 7th and 9th modes are not excited at 75 degree incidence. For the modes excited, there are repeated and inaccurate results.

6.4 Discussions

In this chapter, only the simulation results of the CNRs of the sphere and thin wire were obtained and the validation of the simulation results is by comparison to the investigations by other simulations or theoretical calculations. A recent report by the group in Manchester Metropolitan University [15] shows that it is possible

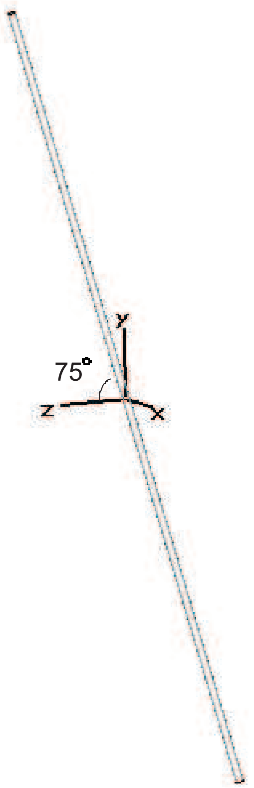

Figure 6.16: A thin wire with 75 degree inclination angle

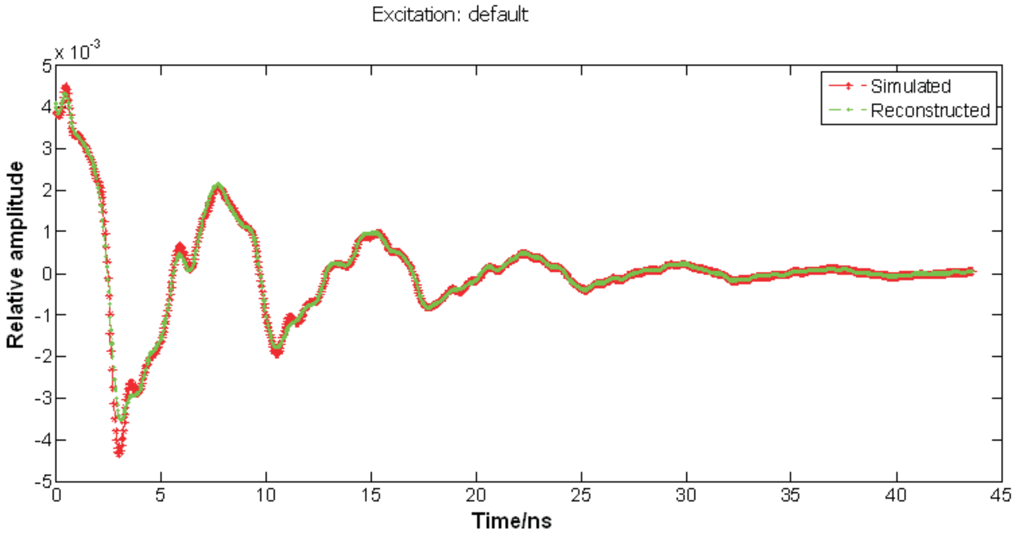

Figure 6.17: Comparison between original simulated and reconstructed waveform

Table 6-D: Comparison of extracted CNR frequencies for 75 degree incidence angle.

MoM(Rothwell) [14]	Extracted in this Chapter	Matrix Pencil Method by Lui [3]
0.87	0.79; 0.87	0.861
1.80	1.77; 1.7325; 1.62; 1.47	1.779
2.72	2.60	2.715
3.66	3.52; 3.37;3.25	3.63
4.59	not excited	Not excited
5.52	5.14	5.28
6.45	Not excited	6.48
7.38	7.34	Not excited
8.31	not excited	8.56
9.24	9.26	Not excited

to verify the CNRs of the target of interest by experiments. In its report, the transient responses from a human body with and without a concealed handgun are evidently different, and the later time response from the tested handgun is obvious. The extracted complex resonance frequencies of the handgun in both cases are close to each other only with change of the damping factor of one of the complex resonance frequency. Considering above, it is advised to form the signature database using the method developed in this chapter and verified it with the experiment.

Ideally, the wider frequency range of the interrogation pulse, the more modes of CNR frequencies can be excited, however, in practice only a limited frequency range can be used. The frequency range of the pulses used in the simulations in this chapter are: 0-2.0 GHz for the conducting sphere, 0-0.5 GHz for the dielectric sphere, 0-9.0 GHz for the thin wire with a 15 degrees inclination angle, and 0-1.5 GHz for the thin wire with a 75 degrees inclination angle. Harmer [15] used a frequency range of 0.5-18 GHz in his experiment and the CNR frequencies below

0.5 GHz are not excited. The CNR frequencies excited for the sub-machine gun and the small handgun, on and off body in either case, range from 0.5 GHz to 2.5 GHz. The frequency range of a novel antenna based on a bow-tie slot antenna they designed is from 0.3 GHz to 1.0 GHz. Based on these results, the author suggest that using a frequency range from 0.3 GHz to 9.0 GHz would be able to excite enough modes for the identification of a handgun-sized object.

CWD systems based on different technologies can be combined and complement each other, in the case considered in this thesis, the electromagnetic resonances based detection system will be combined with the MMW imaging based system. Combining MMW imaging with EM resonance based detection offers the potential for improved system performance. Its drawbacks of high false alarm rates can be circumvented by the combination with the MMW imaging based technology. Since the MMW imaging system offers the target image, this would greatly narrow down the lists of weapon signatures that automation algorithm needs to compare to, hence the improved detection rate is resulted. The deployment of the resonance based CWD system combined with MMW holographic imager will be discussed in chapter 7.

6.5 Conclusions

In this chapter, the CNR extraction technique is developed. The procedure of the extraction of CNR frequencies contains two steps. The first step is to obtain the late time response from the transient solver of CST Microwave Studio. The second step is using GA to extract the CNR frequencies. Three targets, i.e. a metallic sphere, a dielectric sphere and a thin wire with 15 degrees and 75 degrees inclination angle are simulated. For the metallic sphere and the dielectric sphere, the CNR frequencies extracted using the method developed in the chapter are comparable with other simulated or theoretical results. For the extracted natural resonance frequencies for the thin wire, not all the modes can be extracted at certain orientation angles. Though some modes are extracted correctly, there exists a certain level of false alarm. The more complex cases such as overlapped targets and concealed targets have not been considered yet, in which case more false alarm would appear. Also, a large database containing the resonance frequencies information of targets of interest has to be constructed before hand. Experimental report from other group suggests that it is possible to form the signature database using the method developed in this chapter and verified it with experiment. The author suggest that using a frequency range from 0.3 GHz to 9.0 GHz would be able to excite enough modes for the identification of a handgun-sized object.

Resonance based target recognition on its own it is not viable because of the high alarm rate but it might be combined the with the imaging based approach to enhance the detection and circumvent the high alarm issue. In this thesis, it will be combined with the MMW holographic imager. The MMW image of the target narrows down the list of the search database that the automation program need to compare to. The deployment of such a system will be discussed in chapter 7.

References

[1] Baum, C. E.; *On the singularity expansion method for the solution of electromagnetic interaction problem* Air Force Weapons Lab. Interaction Notes, Note 88, (Dec. 1971).

[2] *http://www.cst.com/Content/Products/MWS/Overview.aspx*

[3] Lui, Hoi-Shun; Shuley, N. V.; *On the analysis of electromagnetic transients from radar targets using smooth pseudo wigner-ville distribution (SPWVD)* Antennas and Propagation International Symposium, 2007 IEEE, 9-15 June 2007. Page(s): 5701 - 5704. Digital Object Identifier 10.1109/APS.2007.4396845.

[4] Choi, In-Sik; Lee, Joon-Ho; Kim, Hyo-Tae; Rothwell, E.J.; *Natural frequency extraction using late-time evolutionary programming-based CLEAN* Antennas and Propagation, IEEE Transactions on, Volume 51, Issue 12, Dec. 2003. Page(s): 3285 - 3292. Digital Object Identifier 10.1109/TAP.2003.820955.

[5] Ilavarasan, P.; Rothwell, E. J.; Kun-Mu Chen; Nyquist, D. P.; *Natural resonance extraction from multiple data sets using a genetic algorithm* Antennas and Propagation, IEEE Transactions on, Volume 43, Issue 8, Aug. 1995. Page(s): 900 - 904. Digital Object Identifier 10.1109/8.402216.

[6] Baum, C. E.; Rothwell, E. J.; Chen, K. M.; Nyquist, D. P.; *The singularity expansion method and its application to target identification* Proceedings of the IEEE. Volume 79, Issue 10, Oct. 1991. Page(s): 1481 - 1492. Digital Object Identifier 10.1109/5.104223.

[7] Chuang, C. W.; Moffatt, D. L.; *Natural Resonances of Radar Targets Via Prony's Method and Target Discrimination* Aerospace and Electronic Systems, IEEE Transactions on. Volume: AES-12, Issue: 5. Digital Object Identifier: 10.1109/TAES.1976.308260. Publication Year: 1976, Page(s): 583 - 589.

[8] Mackay, A.; McCowen, A.; *An improved pencil-of-functions method and comparisons with traditional methods of pole extraction* Antennas and Propagation, IEEE Transactions on, Volume: 35, Issue: 4. Publication Year: 1987. Page(s): 435 - 441.

[9] Rothwell, E.; Kun-Mu Chen; Nyquist, D.; *Extraction of the natural frequencies of a radar target from a measured response using E-pulse techniques* Antennas

and Propagation, IEEE Transactions on. Volume: 35, Issue: 6. Publication Year: 1987, Page(s): 715 - 720.

[10] *http://www.softechdesign.com/GA/EvolvingABetterSolution-GA.html*

[11] Chen, Kun-Mu; *Impulse Response of a Conducting Sphere Based on Singularity Expansion Method* Proceedings of the IEEE Volume 69, Issue 6, June 1981. Page(s):747 - 750.

[12] AKELA; *US Department of Justice Final Report-Demonstration of a Concealed Weapons Detection System Using Electromagnetic Resonances* January 2001 [Online]. http://www.ncjrs.org/pdffiles1/nij/grants/190134.pdf.

[13] Turhan-Sayan, G.; Kuzuoglu, M.; *Pole estimation for arbitrarily-shaped dielectric targets using genetic algorithm-based resonance annihilation technique* Electronics Letters. Volume 37, Issue 6, 15 Mar 2001. Page(s): 380 - 381. Digital Object Identifier 10.1049/el:20010274.

[14] Rothwell, E. J.; Baker, J.; Nyquist, D. P.; Chen, K. M.; *Approximate natural response of an arbitrarily shaped thin wire scatterer* IEEE Trans. Antennas and Propagation. VOL 39, No 10, pp1457-1462, October 1991.

[15] Harmer, Stuart; Andrews, David; Bowring, Nicholas; Rezgui, Nacer; Southgate, Matthew; *Ultra wide band detection of on body concealed weapons using the out of plane polarized late time response* Millimetre Wave and Terahertz Sensors and Technology II, Vol.7485, No.1.(2009), 748505.

Chapter 7

Imager System Implementation

7.1 Introduction

In chapter 2 to 5, the parameters, performance evaluation and new devices and image enhancement techniques for the 94 GHz MMW holographic imager has been investigated, and in chapter 6 the possibility of combining the resonance based target recognition with imaging based CWD technique to improve the levels of threat detection were discussed. This chapter will concentrate on the implementation of such a system based on the results and conclusions achieved in the chapter 2 to 6. Two possible imager configurations are proposed in this chapter. The first one uses a conventional waveguide based array feeding a focused reflector antenna system to illuminate the body at a 2-3 meter stand-off distance. The second uses the same configuration replacing the complex and expensive waveguide array with an array-on-a-chip solution. Both imaging systems are incorporated with a resonance based system to provide extra information about the target and a CCTV camera for image fusion to assist the location of the concealed target in the body. System parameters for both systems are tabulated and compared. There advantages and disadvantages are discussed. Most of the parameters are directly or inferred from experimental results with theoretical results to back them up.

There are a few innovations in this design, including: 1. Using woodpile EBG antenna. The shared aperture feature makes the compact design of the imaging array possible. 2. Using an optical waveguide to deliver light to optically switched silicon. 3. The combination of resonance based target recognition technique with the imaging based CWD system to narrow down the lists that the automation algorithm need to compare to, hence to reduce the high false alarm rate. 4. Quasi-optical feeding to the imaging array eradicating use of any cables or transmission lines, a neat design is achieved.

7.2 System design

7.2.1 System design requirement

Here are the basic requirement of the imager:

1. Real time, video rate (1/20th second frame rate) imaging
2. Application: airport passenger screening. It should be able to penetrate common clothing and detect metallic and dielectric objects concealed on a human body.
3. Controlled environment. Minimal cooperation of individuals is required.
4. Operating frequency: 94 GHz. In chapter 5 some textiles properties have

been investigated to justify the choice of using millimetre wave imaging which offers the desired penetration and resolution.

5. An indoor environment is assumed, in which case natural illumination is very weak, hence an auxiliary illumination source (frequency 94 GHz) is introduced.

7.2.2 System design procedure

In chapter 3, we have proved that for a target area of 400mm by 400mm at a distance of 1000mm, the imaging array should have the same dimension of 400mm by 400mm at the sampling rate of 3 wavelengths with resolution of 4mm (theoretical), with 41 by 41 elements used. The 3-D reference coordinate system used in chapter 3 is reproduced here as Fig 7.1 for convenience. Based on this mini-experimental system, we can work out the 'life-size' system parameters by two operations, i.e. system parameters scaling up and pupil plane to focal plane transform using a reflector.

The process of system parameters scaling up and pupil plane to focal plane transform is illustrated in Fig 7.2. Fig 7.2(a) is the mini-experimental system used in chapter 3, (b)is the scaled system with imaging array dimension 1000mm by 1000mm, area of scan 1000mm by 1000mm, detection range 2500mm, and 100 by 100 elements used, but the same element spacing remains unchanged. The reason that backs up the scaling-up process is that the spatial frequency in target plane still can be sufficiently sampled in the recording aperture as the maximum spatial frequency Kx and sampling rate (element spacing) remain unchanged in the scaled system.

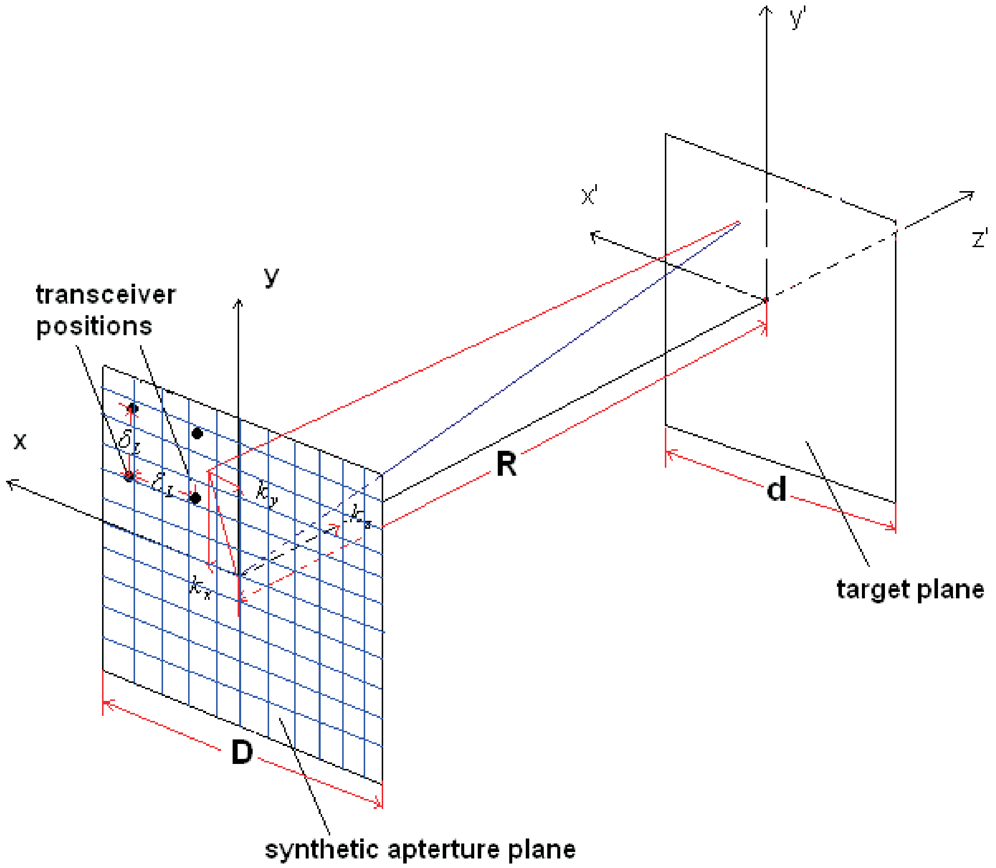

Figure 7.1: The 3-D reference system

The second step is to use a quasi-optical system to transform the pupil plane array into an focal plane array, see Fig 7.2 (b) and (c). Scanning in the focal plane is equivalent to scan in the pupil plane with a scaling down factor for the imaging array dimension and element spacing, but the number of elements remains the same which is 100 by 100 elements (element spacing is 3 wavelengths). If element spacing 5 wavelengths is chosen, 63 by 63 elements will be used.

7.2.3 Focal plane array element spacing

The smallest imaging array dimension is limited by the element spacing. For the waveguide and woodpile EBG antennas, it is 5mm in E plane and 7mm in H

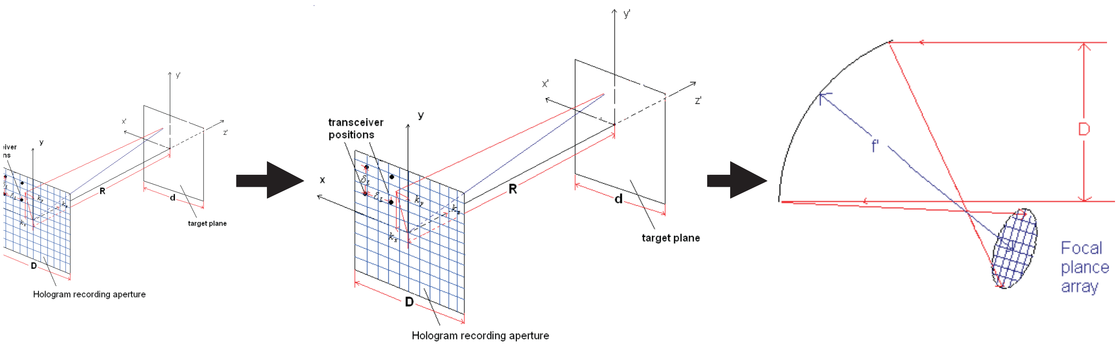

Figure 7.2: The process of system parameters scaling up and pupil plane to focal plane transform (a) The mini-experimental system used in chapter 3 (b) The scaled system (c) Using a reflector to transform the pupil plane array in a focal plane one

plane. For the array-on-the-chip array it could be as small as 2mm.

7.2.4 Focal plane array dimension (if 5 wavelengths spacing is used)

If element spacing 5 wavelengths is chosen, then 63 by 63 elements will be used, so for the waveguide based array, the imaging array dimension is 63×7mm=441mm by 63×5=315mm. For the array-on-a-chip based array, the dimension is 63×2=126mm by 63×2=126mm.

7.2.5 Resolution at the maximum detection range

As discussed in chapter 4, for the transmitter and receiver simultaneous scan, the resolution can be calculated according to the following equation, $\delta_x=\frac{\lambda}{2D}$R, where δ_x is the lateral resolution, λ is the wavelength of the operation frequency and it is 3.19mm at 94 GHz, D is the lateral dimension of the recording aperture and it is 1000mm. R is the distance and it is 2500mm, so δ_x=4 mm. For receiver only scan the resolution equation is $\delta_x=\frac{\lambda}{D}$R, so δ_x=8 mm.

7.2.6 Field of view

To calculate the field of view of the imager, coherence length l=c/B must be calculated first, where c is the light speed in free space, B is the Bandwidth. The woodpile EBG antenna has a bandwidth B of 1 GHz, so l=300mm. Field of view (FOV) is calculated by the equation $\theta = arcsin\frac{l}{D}$=±17.45°.

7.2.7 Determining how many frequencies can be used in a multiple frequencies imaging system.

As discussed in chapter 5, when using multiple frequencies for image enhancement, the frequency interval should satisfy the criterion Δf<$\frac{c}{4R_{max}}$, At 2500mm range it is 0.03GHz. The woodpile EBG lens has a bandwidth of 1 GHz, so 33 frequencies can be used, corresponding to a process gain of 20log$\sqrt{33}$=15dB, but the process gain brought by the number of frequencies used should be limited by the system dynamic range.

7.2.8 System dynamic range, transmission power.

The investigation results in chapter 4 show that the prototype imager has a dynamic range of 60 dB, maximum transmission power is 20 mW, and normal operation transmission power is 5 mW to 10 mW. For the test target a knife edge, SNR_I is 23.3, NEΔR is 0.0419. The designed system are expected to have comparable performances.

7.3 Two implementations of the above design

7.3.1 Waveguide based array

The overall configuration based on a waveguide array is shown in Fig 7.3. In this system the illumination of the target comes from a fixed source, and the 3dB beam width needs to be sufficient to illuminate the 1.8m high target from a stand-off distance of 2.5 metres, leading to a beam width of 40 degrees. This is easily achieved with a direct radiating horn or EBG superstrate antenna. The safe radiation density on an individual should satisfy the EU standard which is below 5mW/cm^2. A single off-set reflector quasi-optical system is used for the receiving path for the imaging based system. The CCTV camera is used to record the video for image fusion. The details of the waveguide array are shown in Fig 7.2.

Resonance based target recognition on its own has the high alarm rate issue, but here it is combined the with the imaging based approach to enhance the detection and circumvent the high alarm issue, its frequency needs to be 0.3 GHz - 9.0 GHz (see chapter 6). The MMW image of the target narrows down the list of the search database that the automation program need to compare to. The video captured by the CCTV camera is used for image fusion, precise location on the body can be achieved, also small movement of the target between subsequent images can result in image details complementing each other.

1. A woodpile EBG lens is used to sharpen the radiation patterns of the waveguide based rx array.
2. Two separate sources are used. One provides the LO signals for the harmonic mixers of both reference and receiving channels, the other provides

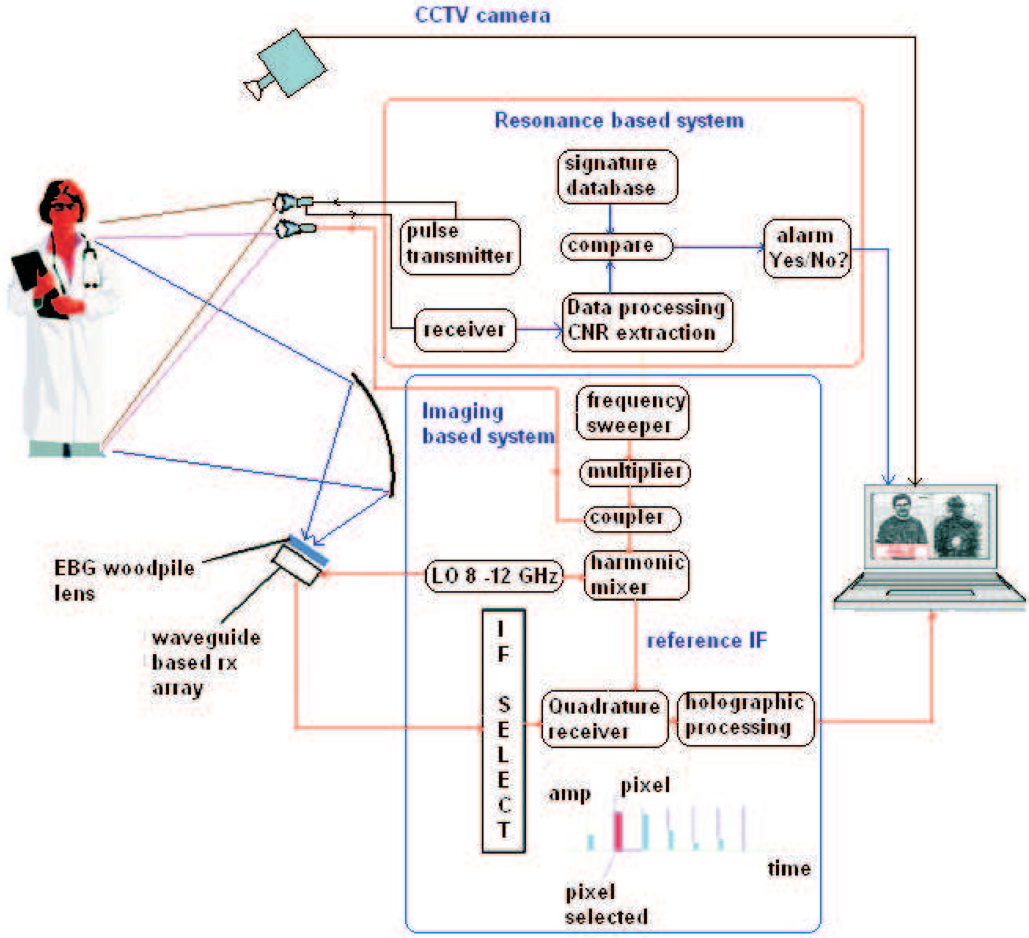

Figure 7.3: Imager based on waveguide based imaging array

the multiplier source with the relevant harmonic for 94 GHz. The transmit source signal goes through a multiplier then a coupler, one output of which is transmitted by the tx antenna, the other provides the input of the harmonic mixer for the reference channel.

3. The IF outputs from all the rx harmonic mixers are connected to an IF select array. The output of the IF select and reference IF are the inputs of the quadrature receiver, which gives the amplitude and phase of the test signal received by the front end IF select array.

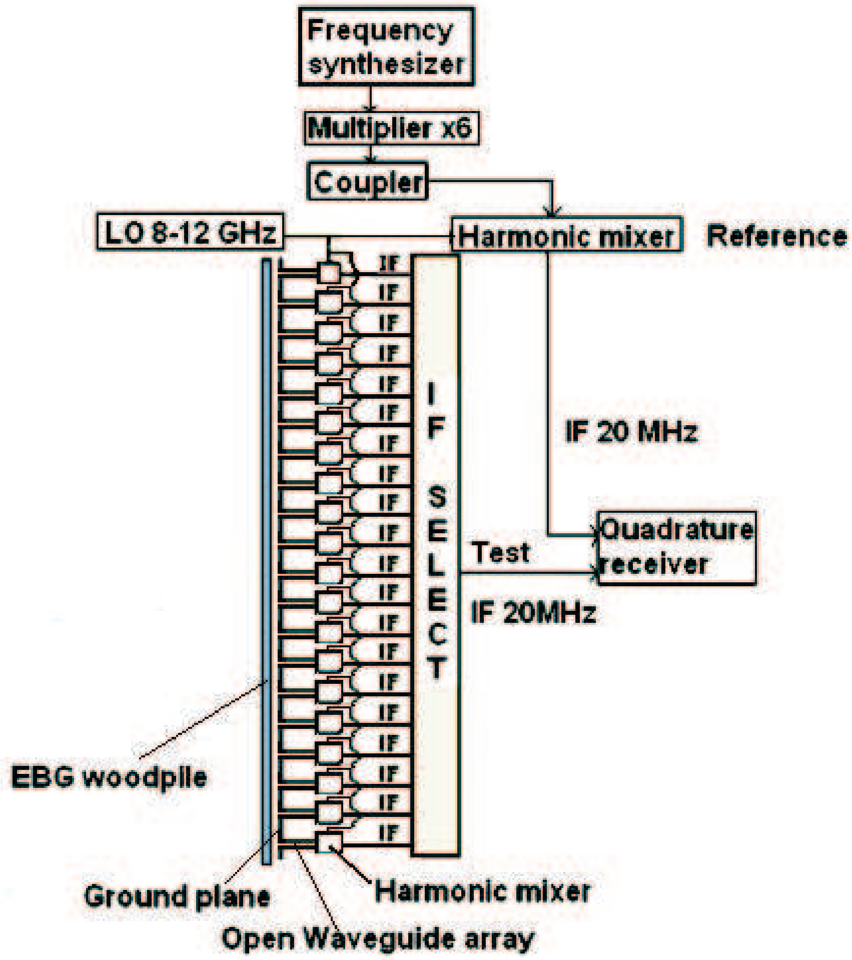

Figure 7.4: Diagram of the waveguide based imaging array

4. No phase shifter is required, because calibration (Amplitudes and Phases) is instigated prior to use for all the sub-array elements.

Issues that might arise:

1. The constraint of the available woodpile EBG lens with the required dimension as large as 441mm by 315mm. It is not possible to fabricate a woodpile EBG lens of this size currently using free forming technique. One possible solution is to combine a few small woodpile EBG lens to form a large one. But the shape of each small woodpile EBG lens should be carefully chosen so

that the antenna element near their edges would not be affected. This could be combined with the concept of a sparse array.

2. The constraint of the circuitry physical dimension. The smallest waveguide array element spacing in the design is about 5mm, the harmonic mixer circuitry behind the waveguide should be physically small enough to be accommodated.
3. IF switch speed is critical. The IF select switch is an x-y matrix, from which the selection of a column or row is controlled by the electrical control lines. For video rate imaging, the raster refresh rate plus data processing time for a frame is about 50 ms. Suppose the 63×63 front ends in the imaging array are selected sequentially, 63 elements in a row and 63 elements in a column, then the switch time from one row or column to another should not be more than $50 \div 63 \doteq 0.7937$ ms.
4. The processing speed is critical. The delay of the video display from the real scene will depend on the computing power. Efforts such as increasing the computing capacity and optimizing the data processing algorithm should be made to ensure the delay is unperceived.
5. Very high cost of manufacturing due to high component count, especially the waveguide mixer at every array port. The array is heavy and bulky.
6. Use of harmonic mixing means high conversion loss.

Advantages of such a design:

1. The woodpile EBG and waveguide receiving array are low profile.
2. No phase shifter is required in the design, which reduces system complexity.

3. No RF switch is used, which avoids the difficulty of design and manufacturing RF switch at 94 GHz.
4. IF switch at 20 MHz is low profile, and it can be found in mobile phone handsets.
5. By using an IF select, all the front ends can share one or a few expensive quadrature receiver(s).
6. The use of harmonic mixers over fundamental mixing eases the distribution of the LO signal as at low frequencies signal can be easily split and transmitted via flexible cables.
7. Eradication of mechanical scan.

7.3.2 Array-on-a-chip based imaging array

In an attempt to overcome the very high cost and complexity of the waveguide based array described in section 7.2, an imager based around a silicon integrated slot-ring antenna with integrated Schottky diode fundamental mixer is proposed. A 90 GHz-receiving slot-ring antenna with integrated Schottky diode in Fig 7.5 can be the candidate element of the MMIA. The device is compact in that the co-planar line IF stub filter is placed in the centre of the 90 GHz resonant radiating slot ring. The element has been built on a 0.5mm silicon substrate and exhaustively measured at QMUL to verify the FDTD based modelling with considerable success [3]. The LO and incident RF are fed to the device quasi-optically leaving only extraction of the IF by conventional co-planar transmission line. In this antenna both the signal to be received and the fundamental local oscillator are fed to the chip quasi-optically, removing the need to distribute the LO via any form of transmission line.

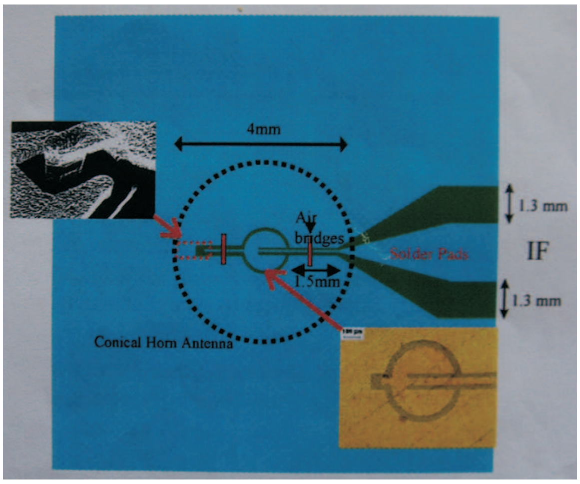

Figure 7.5: Active slot ring antenna at 90 GHz

Receivers are usually the main cost, however, since this process uses standard silicon based lithography the manufacture of an array would be potentially low cost. The complete imaging system is shown in Fig 7.6.

A good down conversion (typical conversion loss is 10 dB) is achieved by making use of a heterodyne receiving architecture with fundamental mixing, compared to a harmonic mixing which has a typical down conversion loss of 30 dB. The target image can be formed directly by the amplitudes of the pixels. If a quadrature receiver is used, both amplitudes and phases information can be recorded, and subsequently microwave holographic processing can be applied.

The array-on-the-chip could have two possible configurations. The first uses conventional row and column switching of the 1.5 GHz IF using standard low-cost components that can be found in a mobile phone. However the columns would need to be fabricated on the backside of the chip, requiring vias at each array element point to connect through to the column, see Fig 7.7.

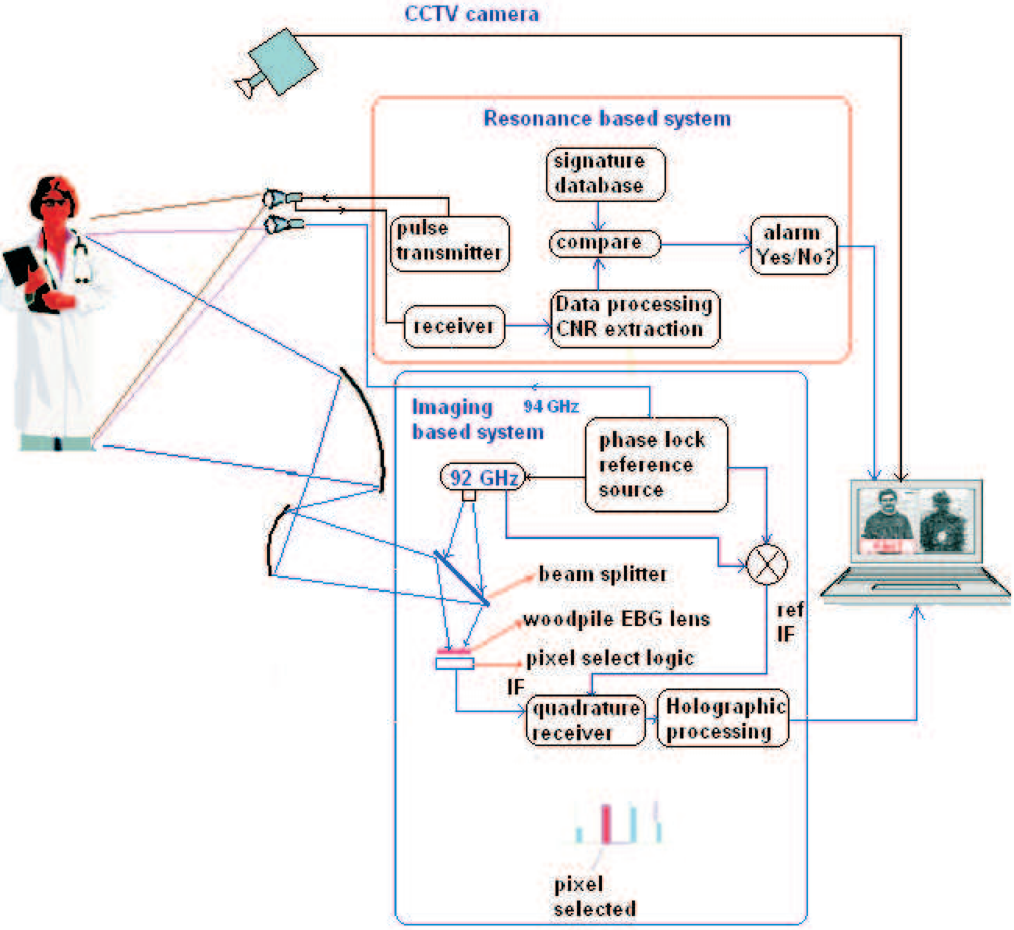

Figure 7.6: On-chip imaging array based MMW imaging system

Table 7-A: Comparison between waveguide based array and array-on-the-chip

	Waveguide based array	Array-on-the-chip
number of FPA elements	63 by 63	63 by 63
element spacing	7 mm in H plane 5mm in E plane	2mm in both E and H planes
dimension of FPA	441mm by 315 mm	126mm by 126mm
mixing mode	harmonic high conversion loss	fundamental low conversion loss
RF feeding	using transmission lines	quasi-optically
features	conventional array forming	MMIA compact design SU-8 optical waveguides used

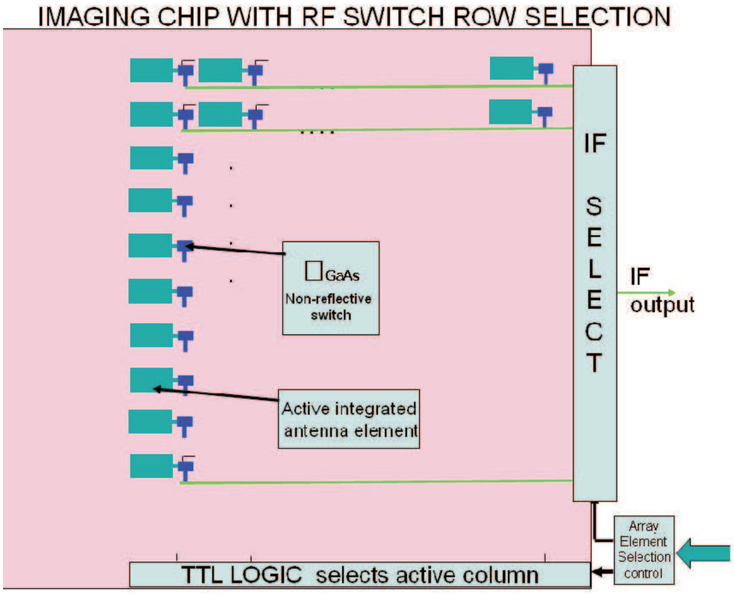

Figure 7.7: Conventional row and column switching of the 1.5 GHz IF using standard components

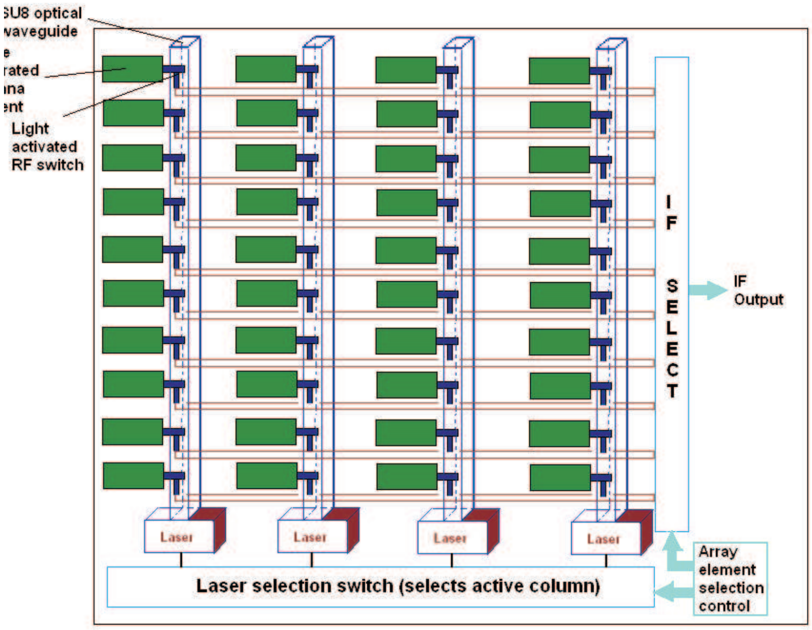

Figure 7.8: Proposed imaging array architecture using SU-8 optical waveguide

An alternative (but speculative) approach is shown in Fig 7.8 where the troublesome backside mounted column is replaced by SU8 optical waveguides integrated on the front face of the array. The Light controlled silicon RF switch [1], see Fig

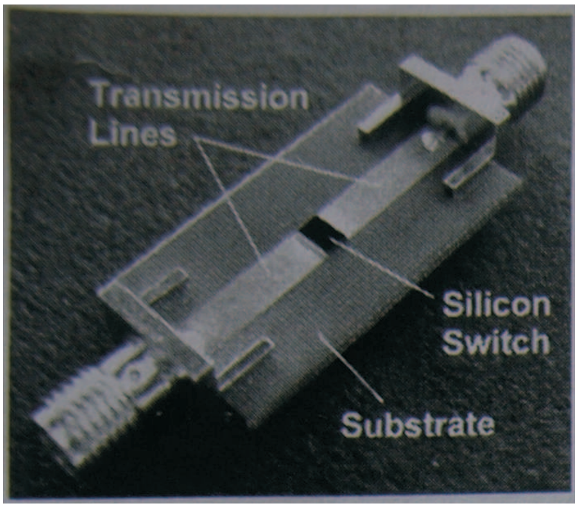

Figure 7.9: Single switch topology, curtesy the Department of Electronic and Electrical Engineering at Loughborough University

7.9, is key component in this design, and has an isolation of 30dB. Under optical illumination charge carriers are generated within the silicon switch, consequently the silicon forms a conducting path between the copper strips, and this area can be regarded as the active region. Extinguishing the light source has the effect of opening the switch. The optically controlled switches will be embedded in the substrate with SU8 waveguides passing over them. Comparison between the waveguide based array and array-on-the-chip is performed in TABLE 7-A. From the comparison, it is concluded that array-on-the-chip approach can achieve a neat (quasi-optically feeding), compact design, with potential low cost in production quantities.

7.4 Illumination of source

Illumination of the active imager with a single source as proposed above has the problem of the coherent illumination creating flash lobes due to constructive and destructive interference. A solution to this problem for indoor imaging systems employs a system proposed by QinetiQ [2] and an imager concept based on this

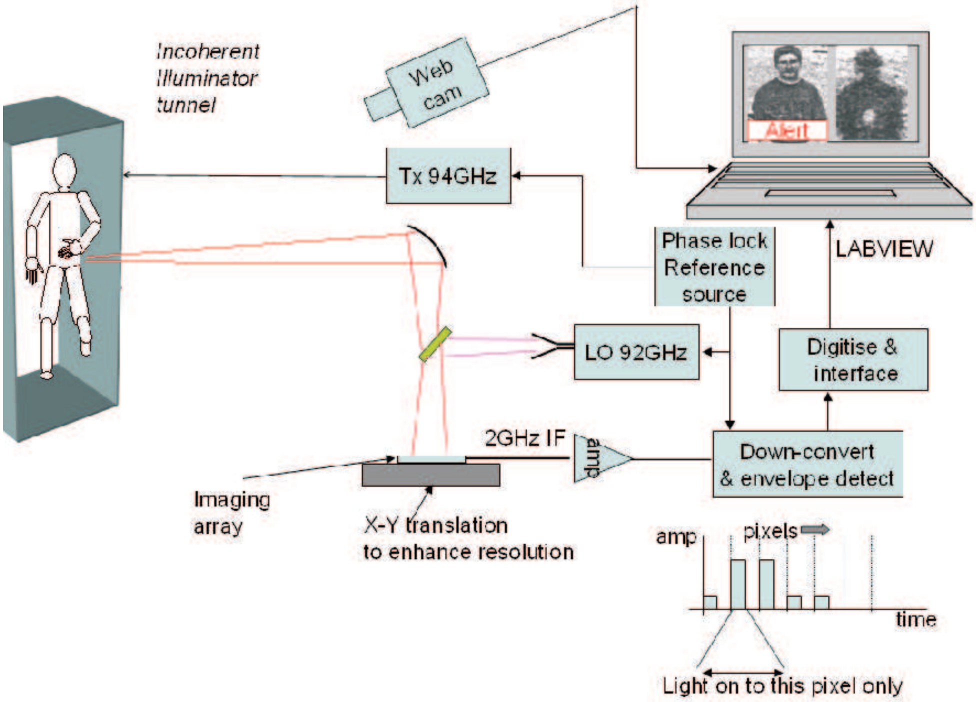

Figure 7.10: Imager diagram based on an incoherent illuminator tunnel

incoherent illumination tunnel is shown in Fig 7.10. Here a walk through tunnel is fabricated with slotted waveguide leaky wave illumination along each side of the tunnel. This insures the target is illuminated incoherently so avoiding the flash lobe effect.

7.5 Summary

This chapter focuses on the system implementation. There are two steps of the design procedure. In the first step, the mini-system is scaled up to 'life-size'. The reason that backs up the scaling up process is because the highest spatial frequency and element spacing remain unchanged in the process. In the second step, a reflector is used to transform the pupil plane array to a focal plane one. In this process, the number of elements does not change but the element spacing changed. 33 frequencies are used for the image enhancement and it brings a dynamic range increase of 15.2 dB. For the resolution, a single transmitter is used and the theoretical resolution is 8mm. The system has the choice of using multiple transmitters to increase the resolution. Based on the parameters obtained from the mini-system, the parameters of the focal plane array are worked out. Two possible imaging array configurations are proposed. The first one is a conventional waveguide based array and the second one is the array-on-a-chip based. In the second case, both LO and RF are fed quasi-optically. There are two types of switching that can be used. For the first type, the column and row switching of the 1.5 GHz IF uses standard components, and the columns are on the backside of the chip and requires vias to connect through to them. In the second type, SU-8 optical waveguides are used for the column switching, and in this case they will be on the front side. The system transmission power, the normal operation transmission power, system dynamic range, test target (a knife egde) SNR_I and NEΔR are estimated based on the 94 GHz MMW prototype holographic imager designed in this thesis. The waveguide based and array-on-the-chip imagers parameters are compared. The latter has a more compact design with the focal plane array dimension of 126mm by 126mm. Other parameters are the same in the two designs. The designed system parameters are listed in TABLE 7-B. From the comparison, it is concluded that array-on-the-chip approach can achieve a neat (quasi-optically feeding), compact design, with potential low cost in production quantities. Resonance based target recognition on its own has the high alarm rate issue, but here it is combined the with the imaging based approach to enhance the detection and circumvent the high alarm issue, its frequency needs to be 0.3 GHz - 9.0 GHz.

Table 7-B: Imager system parametres summary

	Waveguide based array	Array-on-the-chip
operation frequency	94 GHz	94 GHz
bandwidth	1 GHz	1 GHz
Number of frequency used	33	33
dynamic range increase	15.2 dB	15.2 dB
Field of view	17.5 degrees	17.5 degrees
resolution	8.0mm	8.0mm
number of FPA elements	63 by 63	63 by 63
element spacing	7 mm in H plane 5mm in E plane	2mm in both E and H planes
dimension of FPA	441mm by 315 mm	126mm by 126mm
area of scan	1000mm by 1000mm	1000mm by 1000mm
detection range	2500mm	2500mm
main reflector dimension D	1000mm	1000mm
system transmission power (maximum)	20 mW	20 mW
normal operation power	5 mW	5 mW
system dynamic range	60 dB	60 dB
Test target (knife edge) SNR_I	23.3	23.3
Test target (knife edge) NEΔR	0.0419	0.0419

References

[1] Panagamuwa, C. J.; Chauraya, A.; Vardaxoglou, J. C.; *Frequency and beam reconfigurable antenna using photoconducting switches* Antennas and Propagation, IEEE Transactions on. Volume: 54, Issue: 2, Part: 1. Digital Object Identifier: 10.1109/TAP.2005.863393. Publication Year: 2006. Page(s): 449 - 454.

[2] Coward, Peter R.; Appleby, Roger; *Development of an illumination chamber for indoor millimeter-wave imaging* Proc. SPIE, Vol. 5077, 54 (2003); doi:10.1117/12.487031.

[3] Yeap, S. B.; Parini, C. G.; Dupuy, J. A.; Rayner, M. R.; *FDTD simulation and measurement of a 90 GHz quasi-optical annular slot receiver* Microwaves, Antennas and Propagation, IEE Proceedings. Volume: 152, Issue: 2. Digital Object Identifier: 10.1049/ip-map:20045014. Publication Year: 2005, Page(s): 117 - 123.

Chapter 8

Conclusions, discussions and outlook

8.1 Conclusions

Concealed target imaging involves several areas of research, for example, the optimum operation spectrum, the system architecture, the component development and data processing. The comparison of different imaging techniques is necessary, the advantages and disadvantages of different techniques need to be understood. Manufacturing of imagers is expensive and they are currently physically large, the endeavour of cost reduction and miniaturization is worthwhile. This includes the investigation of low profile component, and the optimum system parameters. Based on literature surveys and first hand experimental results, this thesis aims to provide system level parameter determination to aid the development of a target detection imager. The goal set forth here is approached step by step in 7 chapters, with topics and issues addressed ranging from reviewing the past work, finding out the best candidate technology,i.e. MMW holographic imaging combined with the resonance based target recognition technique, the construction of the 94 GHz MMW holographic prototype imager, experimental trade-off investigation of system parameters, imager performance evaluation, low profile components and image enhancement techniques, feasibility investigation of resonance based technique, to system implementation based on the parameters and results achieved.

In chapter 1, the technologies used for CWD, including earth magnetic field distortion, inductive magnetic field, acoustic and ultrasonic, electromagnetic resonance, MMW, THz, Infrared, x-ray are reviewed. From this brief review it is evident that MMW based techniques offer an attractive solution because, of all the above reviewed technologies, MMW offers both good penetration ability and high resolution advantages, both metallic and non-metallic objects can be detected, both stand-off and near proximity operation are possible, with no ionising radiation hazard. Indeed there is very little (even in the active MMW systems) non-ionising radiation posed to the scanned individual. The radiation power of the active imaging system used for imaging could be 1000 times lower than the EU standard for the maximum allowed radiation power density on an individual, which is $50W/m^2$. In addition, it has other advantages such as size reduction, wide available bandwidth, mitigation of industrial interference frequencies compared to microwave band. All of these make it an ideal spectrum for concealed weapon detection.

Also in chapter 1, the possibility of combining MMW imaging with EM resonance based detection is proposed. Such a combination offers the potential for improved system performance. EM resonances based CWD technology is active can be used for stand-off detection. It has a high penetration ability and both metallic and non-metallic objects can be detected. Its drawbacks of high false alarm rates can be circumvented by the combination with the MMW imaging based technology. Since the MMW imaging system offers the target image, this would greatly narrow down the lists of weapon signatures that automation algorithm needs to compare to, hence the improved detection rate is resulted.

In chapter 2, a brief overview within the category of MMW imaging is conducted. The place of the MMW imager based on microwave holography within the whole family tree of holography is located. The characteristics of passive and active imagers have been summarized and compared. In terms of illumination, while passive imaging has the advantage of free natural illumination, it is not suitable for the indoor environment operation. On the other hand, active imaging uses artificial illumination and has a variety of waveforms to choose. Passive images are formed pixel by pixel with small dynamic ranges, whereas images formed by microwave holographic method have high dynamic ranges. As the target RCS could vary greatly, the latter is more effective for CWD operations. Direct detector receivers need cryogenic operation to achieve high sensitivities which is a drawback, while heterodyne receiving can operate at room temperatures with high sensitivities, the latter is more viable for real system implementation. Lastly, for the same aperture dimension used, microwave holography can achieve higher resolution than passive imaging. From the comparisons and discussions, it is concluded that the microwave holography based active imaging system, with a CW single/multiple frequency(ies) illumination, using the heterodyne receiving architecture provides a viable solution for CWD operation with respect to the scenarios defined.

In the second part of chapter 2, based on the microwave holography theory, a prototype imager operating at 94 GHz is designed and implemented using the NSI 2000 scanner and Agilent 8510 C Vector Network Analyzer as the transmitter and receiver. Detailed system description is given. Basically the system has a dynamic range of 60 dB, an output power of 12.7 dBm. The two-step imaging procedure is also introduced, i.e, hologram recording and raw data processing. Use of the NSI 2000 Measurement system is stated. The prototype is ready to perform the investigations in the following chapters.

In chapter 3, a range of system parameters are investigated. In the array element spacing investigation, the theoretical array element spacing 5λ and experimental results agrees very well. Compared to the 0.5λ array element spacing, the number of array elements are significantly reduced. In the array dimension investigation, when the dimension reduced to 200mm by 200mm, the image quality is still very good, this is due to the scan mode chosen in the measurement, which is the transmitter and receiver simultaneous scan. It offers finer resolution than the receiver scan only mode. In such a scan mode, theoretically, an aperture size of 200mm can offer a resolution of 8mm, whereas for the receiver scan only mode, it needs 400mm aperture dimension to achieve a resolution of 8 mm. For the MMW images of large and flat objects, the image quality is very sensitive to the normalities of the target to incident wave direction. 10 degrees transmitters spacing is suggested for illumination. Since the system SNR is a variable value when the transceiver scans across the recording aperture, only the maximum system SNR is used for evaluation. When the transmission is 5 mW, the maximum system SNR is 11 dB for a MDF gun replica target, and at this power level, SNR_I of the copper slab saturates at 20 or so, and the SNR_I of the perspex slab is 5, which is at usable level, so 5 to 10 mW transmission power is recommended for normal operation.

In chapter 4, the performance of the 94GHz MMW holographic prototype imager are evaluated qualitatively and quantitatively. For the qualitative evaluation, a range of scenarios are simulated and it is concluded that penetration to common clothes are generally fine. Transmissions of common clothes are generally high. Material discrimination is possible. Target reflectivity contrast against body background maybe low. Image quality is related to the orientation of the target. Resonance within the target could occur and under certain conditions.

For the quantitative evaluation, SNR_I, NEΔR with respect to the test target i.e. a knife edge are used. For the imager resolution, two methods are used. The first one is based on PSF estimation, and it is estimated that resolutions are 3.9mm and 3.1mm in vertical and horizontal direction respectively. The second method is based on the direct measurement. The result obtained by the direct measurement method is finer than 10mm. Even though the VNA receiver used in the imager has a dynamic range of 60 dB, due to the noisy background ($\sigma(B_{notarget})$), the 4mm by 4mm foil cannot be seen. The author would suggest use the smallest metallic square visible to represent the background scene noise level. Two parameters can be used describe the background performance, i.e. $\sigma(B_{notarget})$ and the smallest detectable metallic foil square.

In chapter 5, three investigations are performed. In the first investigation, the feasibility study of applying a woodpile EBG antenna in millimeter wave imaging is presented. The experimental results verified that the proposed antenna has the capability of producing good quality target images to conventional high gain horns due to the shared aperture possibility. When forming an imaging array using woodpile EBG antenna, due to the size of the waveguide, the minimum spacing is suggested to be 5mm in E plane and 7mm in H plane. Such spacing is impossible using conventional horn antennas.

In the second investigation of the chapter 5, the conclusion is that it is feasible to use a sparse array (though the morphology is not optimized) for the millimeter wave imaging for the reduction of array elements. A morphology with just a half of the full array element counts still offers an acceptable image quality, though the optimization is pending further study. Such an array is compatible with the need to split the array into series of sub arrays for the manufacture of the EBG superstrate.

In the third part of the chapter 5, for the investigation of the image enhancement using multiple frequencies, it can be seen that wide band imaging is rather effective with significant increase of the SNR_I experimentally verified. For the woodpile EBG antenna, since the bandwidth is 1 GHz, if the interval of 0.03 GHz is used, then overall 33 frequencies would be used. This brings a dynamic increase of $20\log\sqrt{33}$=15.2 dB.

In chapter 6, the CNR extraction technique is developed. The procedure of the extraction of CNR frequencies contains two steps. The first step is to obtain the late time response from the transient solver of CST Microwave Studio. The second step is using GA to extract the CNR frequencies. Three targets, i.e. a metallic sphere, a dielectric sphere and a thin wire with 15 degrees and 75 degrees inclination angle are simulated. For the metallic sphere and the dielectric sphere, the CNR frequencies extracted using the method developed in the chapter are comparable with other simulated or theoretical results. For the extracted natural resonance frequencies for the thin wire, not all the modes can be extracted at certain orientation angles. Though some modes are extracted correctly, there exists a certain level of false alarm. The more complex cases such as overlapped targets and concealed targets have not been considered yet, in which case more false alarm would appear. Also, a large database containing the resonance frequencies information of targets of interest has to be constructed before hand. An experimental report from other workers suggests that it is possible to form the signature database using the method developed in this chapter and verified it with experiment.

Resonance based target recognition on its own is not viable because of the high alarm rate but it might be combined the with the imaging based approach to enhance the detection and circumvent the high alarm issue. In this thesis, it is combined with the MMW holographic imager. The MMW image of the target narrows down the list of the search database that the automation program need to compare to. The author suggest that using a frequency range from 0.3 GHz to 9.0 GHz would be able to excite enough modes for the identification of a handgun-sized object.

Chapter 7 focuses on the system implementation. There are two steps of the design procedure. In the first step, the mini-system is scaled up to 'life-size'. The reason that backs up the scaling up process is because the highest spatial frequency and element spacing remain unchanged in the process. In the second step, a reflector is used to transform the pupil plane array to a focal plane one.

In this process, the number of elements does not change but the element spacing is changed. 33 frequencies are used for the image enhancement and it brings a dynamic range increase of 15.2 dB. For the resolution, a single transmitter is used and the theoretical resolution is 8mm. The system has the choice of using multiple transmitters to increase the resolution. Based on the parameters obtained from the mini-system, the parameters of the focal plane array are worked out. Two possible imaging array configurations are proposed. The first one is a conventional waveguide based array and the second one is the array-on-a-chip based. In the second case, both LO and RF are fed quasi-optically. There are two types of pixel selection that can be used. For the first type, the column and row switching of the 1.5 GHz IF uses standard components, and the columns are on the backside of the chip and requires vias to connect through to them. In the second type, SU-8 optical waveguides are used for the column switching, and in this case they are on the front side. The system transmission power, the normal operation transmission power, system dynamic range, test target (a knife edge) SNR_I and NEΔR are estimated based on the 94 GHz MMW prototype holographic imager designed in chapter 2. The waveguide based and array-on-the-chip imagers parameters are compared. The latter has a more compact design with the focal plane array dimension of 126mm by 126mm.

Based on the above results and conclusions from each chapter, it is concluded that the goal set forth in the beginning. i.e. achieving system level parameters to assist system design, is achieved.

8.2 Summary of contributions

In chapter 3, the main contribution of the investigations is using the experimental approach to verified the system parameters. The trade off investigation of element spacing and imaging array dimension through the experimental approach using the 94 GHz MMW holographic prototype imager is an innovation.

In chapter 4, what makes the investigation unique here lies in the fact that the imager was active and the holography approach was adopted, though similar investigation has been performed in the passive imaging system. Also, this investigation differs from Tamminen's [1] in the way that the former operation frequency is 94 GHz and using transmitter and receiver simultaneous scan mode, whereas the latter is 310 GHz and receiver only scan mode. Using test target SNR_I, NEΔR, and $\sigma(B_{notarget})$for imager performance evaluation and determining imager resolution by PSF estimation and direct experimental measurement at 94 GHz have not be reported in the open public literature.

In chapter 5, the main contribution of this chapter is the use of the medium gain woodpile Electromagnetic Bandgap (EBG) antenna for millimeter wave imaging at 95 GHz. The main advantage of using such an antenna lies in the fact that a shared antenna aperture by the antenna array elements makes it attractive for array forming, as the aperture size limitation is usually a major issue. Also, the woodpile EBG antenna has other advantages over conventional millimeter wave antennas such as low profile, low cost. Its feasibility study and antenna system evaluation has been undertaken via simulation and measurements in the author's group. This is the first application found for such an antenna.

In chapter 6, the contribution in this area of study is to use the transient solver in CST Microwave Studio to obtain the impulse response, which differs from conventional frequency domain techniques such as method of moment (MoM), in that case inverse Fourier transform is used to obtain its time domain data sets.

In chapter 7, there are a few innovations in this design, including: 1. Using woodpile EBG antenna. The shared aperture feature makes the compact design of the imaging array possible with medium gain array elements. 2. Using an optical waveguide to deliver light to silicon switches. 3. The combination of resonance based target recognition technique with the imaging based CWD system to narrow down the lists that the automation algorithm need to compare to, hence to reduce the high false alarm rate. 4. Quasi-optical feeding to the imaging array eradicating use of any cables or transmission lines, a neat design is achieved.

8.3 Discussions and outlook

The MMIA forms the heart of the imager and would have wide application. The system in its first generation form would be active, in that a low power millimetre wave source, either coherently or incoherently illuminates the scene to be imaged. In the short term future, it is possible to envisage this image data being fused with that from other sensors such as infrared and biohazard to provide a comprehensive security system. Array element spacing requires the dimension of the array element be confined within a small space (aperture), which results in low gain, wide beam width of the element antenna which in turn breaches the system S/N requirement, so the EBG based woodpile superstrate lens offers valuable gain. Research on the highly integrated imaging array with the woodpile EBG lens is the primary task in the next step. It would offer the possibility of a portable hand-held system.

An investigation concerning the optical design of the reflector system for imaging the array onto the human body, possibly with some "auto focus" technique, is worthwhile.

References

[1] Tamminen, A.; Ala-Laurinaho, J.; Risnen, A. V.; *Indirect holographic imaging: evaluation of image quality at 310 GHz (Proceedings Paper)* Proceedings Vol. 7670. Passive Millimeter-Wave Imaging Technology XIII, David A. Wikner; Arttu R. Luukanen, Editors, 76700A Date: 27 April 2010.

[2] Hoogeboom, Peter; *Advanced Radar Techniques, Delft University of Technology/TNO Defense, Security and Safety, The Netherlands.* European Microwave Week 2009, Workshop Notes, 28 Sep. - 2 Oct. 2009. Rome, Italy.

Appendix A

Author's Publications

Journal Papers

1. L. Zhang; Y. Hao; C. G. Parini; "Millimetre Wave Imaging System Parameters at 95 GHz", IET Microwaves, Antennas and Propagation. doi: 10.1049 /iet-map.2009.0330

Conference Papers

1. L. Zhang; Y. Hao; C. G. Parini; "Natural Resonant Frequency Extraction For Concealed Weapon Detection At Millimetre Wave Frequencies", The Second European Conference on Antennas and Propagation, November, 2007, Edinburgh, UK.
2. L. Zhang; Y. Hao; C. G. Parini; J. Dupuy; "An Experimental Millimetre Wave Imaging System", Loughborough Antenna and Propagation Conference (LAPC '08), Loughborough (United Kingdom), 17-18 March 2008.

3. L. Zhang; Y. Hao; C. G. Parini; J. Dupuy; "An Investigation of Antenna Element Spacing on the Quality of Millimetre Wave Imaging," , the IEEE AP-S International Symposium on Antennas and Propagation and 2008 USNC/UR SI National Radio Science Meeting in San Diego, California, USA, on July 05-12, 2008.

4. L. Zhang; Y. Lee; Y. Hao; C. G. Parini; "Woodpile EBG Structure for Millimeter Wave Imaging Enhancement", invited paper for 2009 IEEE International Workshop on Antenna Technology, iWAT2009: "Small Antennas and Novel Metamaterials" March 2-4, 2009, Santa Monica, California.

5. L. Zhang; Y. Hao; C. G. Parini; " Sparse Array In The Millimeter Wave Imaging System At 94 GHz", 5th ESA Workshop on Millimetre Wave Technology and Applications and 31st ESA Antenna Workshop,18-20 May 2009,ESA/EST EC, Noordwijk, The Netherlands.

6. L. Zhang; Y. Hao; C. G. Parini; "The Development of a Millimetre Wave Imaging System", 2nd UK/Europe China Workshop on Millimetre Waves and Terahertz Technologies. 19th -21st Oct 2009. Rutherford Appleton Laboratory, UK.

Appendix B

Image SNR_I and NEΔR calculation

Calculation steps

For the target with complex geometry, the determination of the boundary between target and non-target areas could be a very time consuming job if the accurate method by finding the maxima and minima near the edge is used. Here an convenient method is used to estimate the image SNR_I and NEΔR. It is a four-step procedure which is described below. The codes are written in Matlab language.

1. Loading the brightness data set of the MMW image of the MDF gun replica and store the values in matrix G(j, i), see Fig 2.1. Since the image has little background noise, it is used to determine the boundary of the target area.

2. Determination of the target area coordinates. The MMW image brightness values are normalized to its maxima ranging from 0.0 to 1.0. Values below 0.1

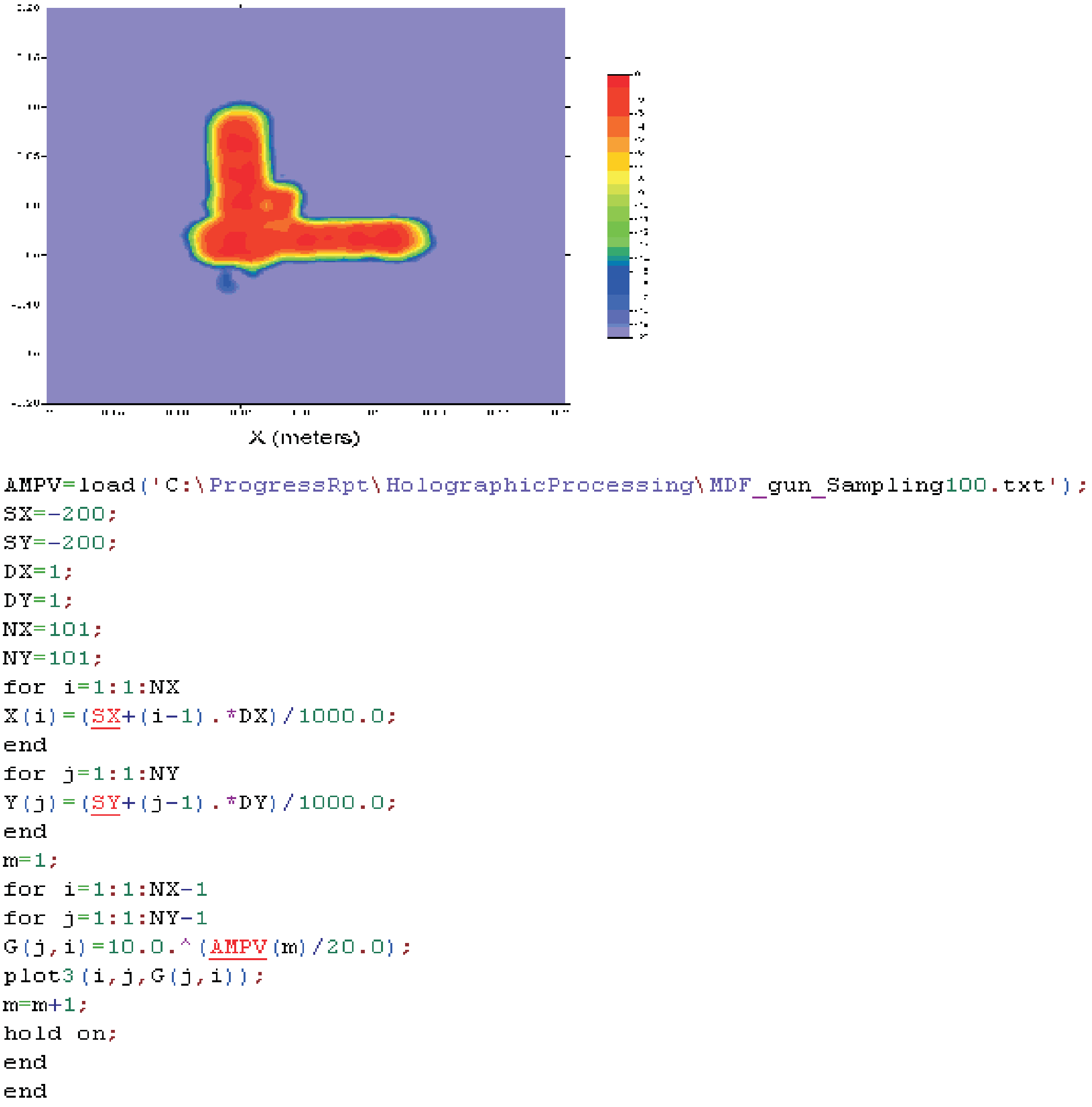

```
AMPV=load('C:\ProgressRpt\HolographicProcessing\MDF_gun_Sampling100.txt');
SX=-200;
SY=-200;
DX=1;
DY=1;
NX=101;
NY=101;
for i=1:1:NX
X(i)=(SX+(i-1).*DX)/1000.0;
end
for j=1:1:NY
Y(j)=(SY+(j-1).*DY)/1000.0;
end
m=1;
for i=1:1:NX-1
for j=1:1:NY-1
G(j,i)=10.0.^(AMPV(m)/20.0);
plot3(i,j,G(j,i));
m=m+1;
hold on;
end
end
```

Figure 2.1: Step 1. Loading the brightness data set of the MMW image of the MDF gun replica.

are considered as noise background. Values above 0.1 are considered to be in the target area and their coordinates are stored in matrix C (x axis) and matrix D (y axis), see Fig 2.2.

3. Loading the brightness data set of the MMW image whose image SNR_I and NEΔR will be calculated, see Fig 2.3.

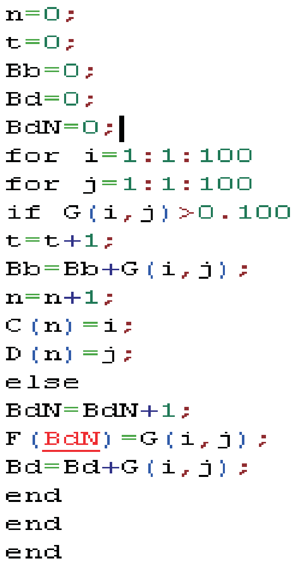

```
n=0;
t=0;
Bb=0;
Bd=0;
BdN=0;
for i=1:1:100
for j=1:1:100
if G(i,j)>0.100
t=t+1;
Bb=Bb+G(i,j);
n=n+1;
C(n)=i;
D(n)=j;
else
BdN=BdN+1;
F(BdN)=G(i,j);
Bd=Bd+G(i,j);
end
end
end
```

Figure 2.2: Step 2. Determination of the target area coordinates.

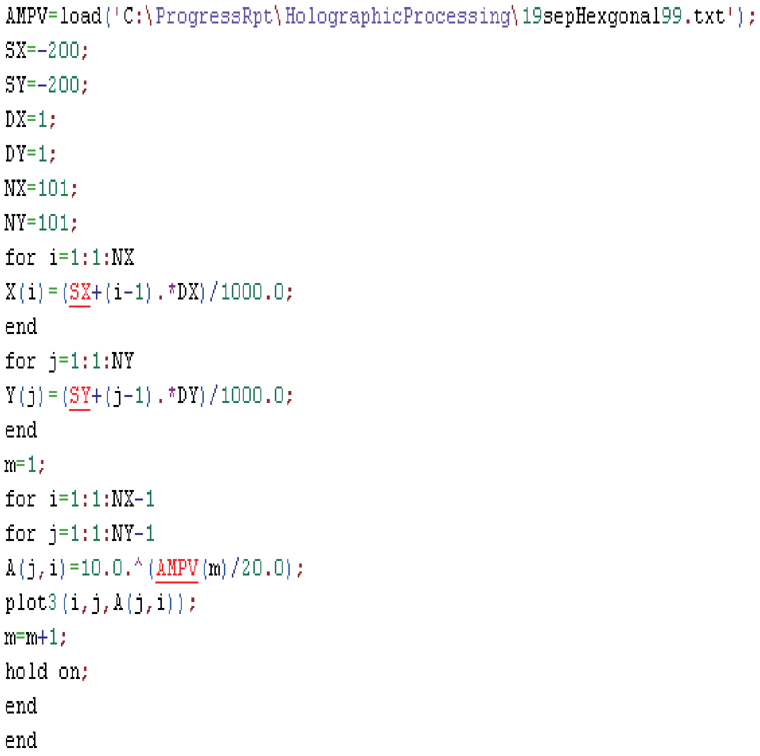

```
AMPV=load('C:\ProgressRpt\HolographicProcessing\19sepHexgonal99.txt');
SX=-200;
SY=-200;
DX=1;
DY=1;
NX=101;
NY=101;
for i=1:1:NX
X(i)=(SX+(i-1).*DX)/1000.0;
end
for j=1:1:NY
Y(j)=(SY+(j-1).*DY)/1000.0;
end
m=1;
for i=1:1:NX-1
for j=1:1:NY-1
A(j,i)=10.0.^(AMPV(m)/20.0);
plot3(i,j,A(j,i));
m=m+1;
hold on;
end
end
```

Figure 2.3: Step 3. Loading the brightness data set of the MMW image whose image SNR_I and NEΔR will be calculated.

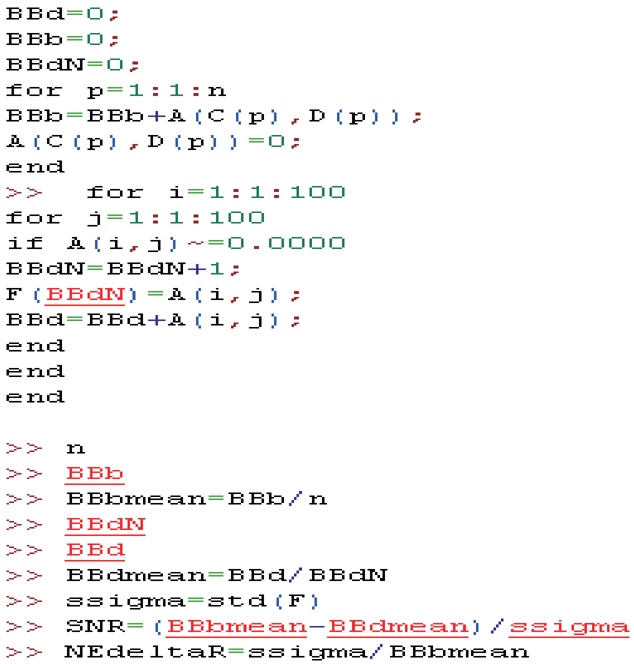

```
BBd=0;
BBb=0;
BBdN=0;
for p=1:1:n
BBb=BBb+A(C(p),D(p));
A(C(p),D(p))=0;
end
>>  for i=1:1:100
for j=1:1:100
if A(i,j)~=0.0000
BBdN=BBdN+1;
F(BBdN)=A(i,j);
BBd=BBd+A(i,j);
end
end
end

>> n
>> BBb
>> BBbmean=BBb/n
>> BBdN
>> BBd
>> BBdmean=BBd/BBdN
>> ssigma=std(F)
>> SNR=(BBbmean-BBdmean)/ssigma
>> NEdeltaR=ssigma/BBbmean
```

Figure 2.4: Step 4. Using the coordinates recorded in step 2 to calculate the image SNR_I and NEΔR.

4. Using the coordinates recorded in step 2 to calculate the sum of the brightness in the target and non-target areas, then calculate the image SNR_I and NEΔR according to their definition equations, see Fig 2.4.

Appendix C

Curve fitting for the measurement data set using sine integral function

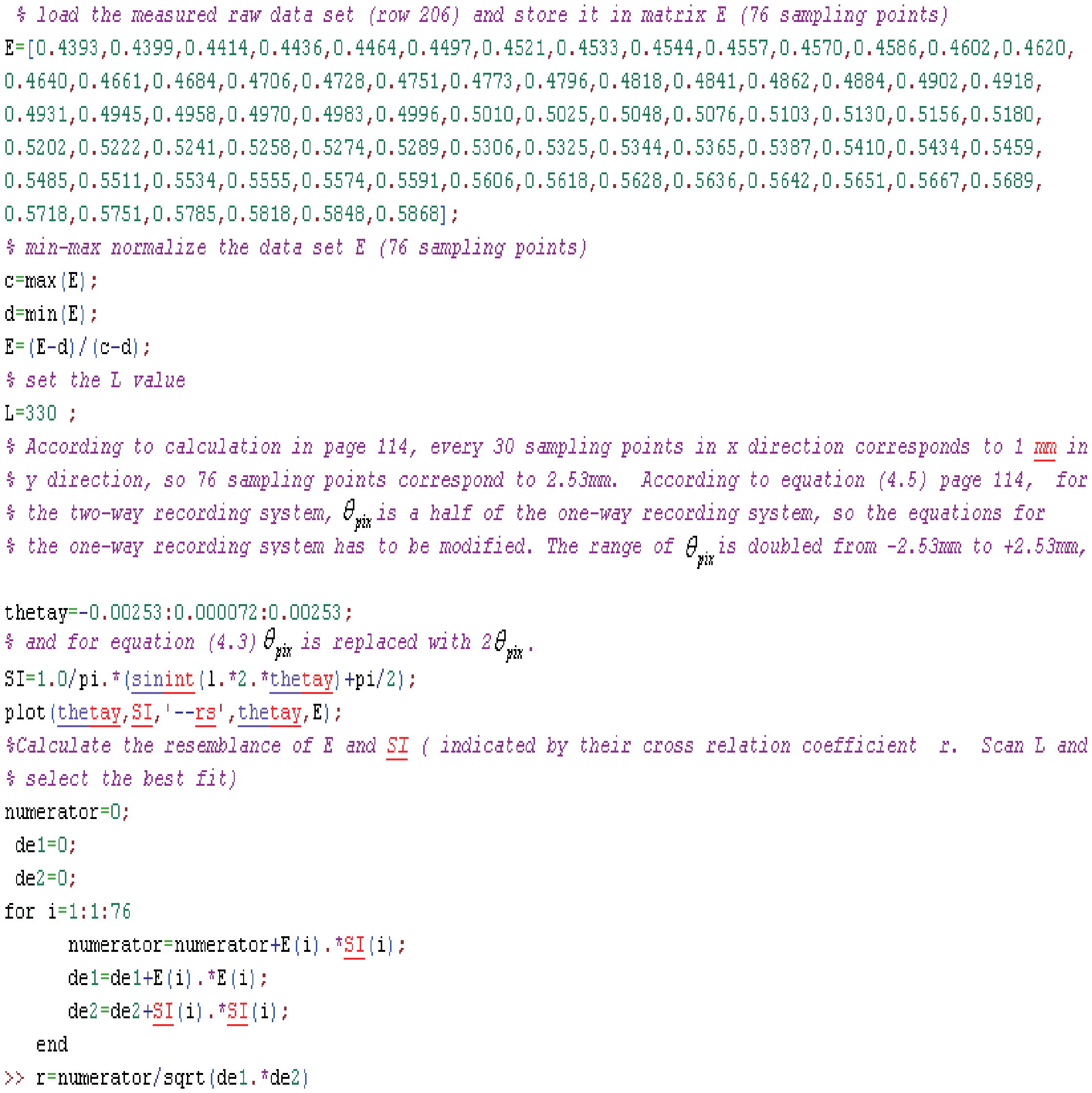

```
 % load the measured raw data set (row 206) and store it in matrix E (76 sampling points)
E=[0.4393,0.4399,0.4414,0.4436,0.4464,0.4497,0.4521,0.4533,0.4544,0.4557,0.4570,0.4586,0.4602,0.4620,
0.4640,0.4661,0.4684,0.4706,0.4728,0.4751,0.4773,0.4796,0.4818,0.4841,0.4862,0.4884,0.4902,0.4918,
0.4931,0.4945,0.4958,0.4970,0.4983,0.4996,0.5010,0.5025,0.5048,0.5076,0.5103,0.5130,0.5156,0.5180,
0.5202,0.5222,0.5241,0.5258,0.5274,0.5289,0.5306,0.5325,0.5344,0.5365,0.5387,0.5410,0.5434,0.5459,
0.5485,0.5511,0.5534,0.5555,0.5574,0.5591,0.5606,0.5618,0.5628,0.5636,0.5642,0.5651,0.5667,0.5689,
0.5718,0.5751,0.5785,0.5818,0.5848,0.5868];
% min-max normalize the data set E (76 sampling points)
c=max(E);
d=min(E);
E=(E-d)/(c-d);
% set the L value
L=330 ;
% According to calculation in page 114, every 30 sampling points in x direction corresponds to 1 mm in
% y direction, so 76 sampling points correspond to 2.53mm.  According to equation (4.5) page 114,  for
% the two-way recording system, θpix is a half of the one-way recording system, so the equations for
% the one-way recording system has to be modified. The range of θpix is doubled from -2.53mm to +2.53mm,

thetay=-0.00253:0.000072:0.00253;
% and for equation (4.3) θpix is replaced with 2θpix.
SI=1.0/pi.*(sinint(l.*2.*thetay)+pi/2);
plot(thetay,SI,'--rs',thetay,E);
%Calculate the resemblance of E and SI ( indicated by their cross relation coefficient  r.  Scan L and
% select the best fit)
numerator=0;
 de1=0;
 de2=0;
for i=1:1:76
      numerator=numerator+E(i).*SI(i);
      de1=de1+E(i).*E(i);
      de2=de2+SI(i).*SI(i);
   end
>> r=numerator/sqrt(de1.*de2)
```

Figure 3.1: Finding out the lateral dimension L by curve fitting for the measurement data set using sine integral function